

**Czech Technical University in Prague**

Faculty of Mechanical Engineering

Department of Automotive, Combustion Engine and Railway Engineering



**Diploma Thesis**

Development of a virtual toolchain for Toyota Hybrid System powertrain  
NV assessment

Supervisors:

Ing. Rastislav Toman

Satrio Wicaksono ST, M.Eng., Ph.D.

Eng. Jeroen De Smet

2020

Bc. Ivo Vodička



# MASTER'S THESIS ASSIGNMENT

## I. Personal and study details

Student's name: **Vodička Ivo** Personal ID number: **437096**  
Faculty / Institute: **Faculty of Mechanical Engineering**  
Department / Institute: **Department of Automotive, Combustion Engine and Railway Engineering**  
Study program: **Master of Automotive Engineering**  
Branch of study: **Advanced Powertrains**

## II. Master's thesis details

Master's thesis title in English:

**Development of a virtual toolchain for Toyota Hybrid System powertrain NV assessment**

Master's thesis title in Czech:

**Vývoj virtuálního toolchainu pro vyhodnocení charakteristik hluku a vibrací pohonných řetězců Toyota Hybrid System**

Guidelines:

1. Couple given 1D detailed powertrain plant model (AMESIM) and HEV control model (SIMULINK) of Toyota Hybrid System powertrain into a toolchain
2. Define and perform validation process for top level performance of the toolchain
3. Define and perform validation process for low frequency powertrain dynamics predicted by the model
4. Define and perform validation process for high frequency powertrain dynamics predicted by the model
5. Identify potential model accuracy improvements

Bibliography / sources:

Name and workplace of master's thesis supervisor:

**Ing. Rastislav Toman, Department of Automotive, Combustion Engine and Railway Engineering, FME**

Name and workplace of second master's thesis supervisor or consultant:

Date of master's thesis assignment: **24.10.2019** Deadline for master's thesis submission: **08.01.2020**

Assignment valid until: \_\_\_\_\_

  
Ing. Rastislav Toman  
Supervisor's signature

  
doc. Ing. Oldřich Vitek, Ph.D.  
Head of department's signature

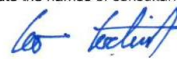
  
prof. Ing. Michael Valášek, DrSc.  
Dean's signature

## III. Assignment receipt

The student acknowledges that the master's thesis is an individual work. The student must produce his thesis without the assistance of others, with the exception of provided consultations. Within the master's thesis, the author must state the names of consultants and include a list of references.

28.11.2019

Date of assignment receipt



Student's signature

## Annotation

<b>Author:</b>	Bc. Ivo Vodička
<b>Title in English:</b>	Development of a virtual toolchain for Toyota Hybrid System powertrain NV assessment
<b>Title in Czech:</b>	Vývoj virtuálního toolchainu pro vyhodnocení charakteristik hluku a vibrací pohonných řetězců Toyota Hybrid System
<b>Academic year:</b>	2019/2020
<b>Study program:</b>	Master of Automotive Engineering
<b>Branch of study:</b>	Advanced Powertrains
<b>Department, faculty:</b>	Department of Automotive, Combustion Engine and Railway Engineering, Faculty of Mechanical Engineering (CTU in Prague) Faculty of Mechanical and Aerospace Engineering (ITB)
<b>Supervisors:</b>	Ing. Rastislav Toman (CTU in Prague) Satrio Wicaksono ST, M.Eng., Ph.D. (ITB) Eng. Jeroen De Smet (TME)
<b>Abstract:</b>	This thesis consists of a review of hybrid vehicles and NV problematics of Toyota Hybrid System powertrain, development and validation of a MBD methodology for the low speed booming noise prediction.
<b>Keywords:</b>	Toyota Hybrid System, noise and vibration, MBD methodology, toolchain model, validation
<b>Number of pages:</b>	113
<b>Number of pictures:</b>	95
<b>Number of tables:</b>	15

## **Declaration**

I hereby declare that I have completed this thesis independently and that I have listed all the literature and publication used in accordance with the methodological guidelines about adhering to ethical principles in the preparation of the final thesis.

*In Prague, 20<sup>th</sup> of January, 2020*

Bc. Ivo Vodicka

## **Acknowledgements**

I would like to thank my mentor Ing. Martin Halánek and supervisor Eng. Jeroen De Smet for the support, guidance and help with the diploma thesis. I would also like to thank my supervisors Ing. Rastislav Toman and Satrio Wicaksono ST, M.Eng., Ph.D. for a patient help with this work.

A big thank you belongs to my family and friends who have supported me throughout my studies.



All the results shown in this thesis have been approved and accepted by my supervisor  
Jeroen De Smet, as a representative of Toyota Motor Europe.

For reasons of confidentiality, most of the data and results shown in this document have been masked  
or replaced by dummy values, in accordance to Toyota Motor Europe's confidentiality guidelines.

# Contents

1. Introduction.....	9
1.1. Motivation.....	10
2. Toyota Hybrid System .....	12
2.1. Introduction to hybrid vehicles architecture .....	12
2.1.1. Level of hybridization.....	12
2.1.2. Hybrid vehicles architecture .....	13
2.2. Toyota Hybrid System Gen4.....	16
2.2.1. Working principles.....	21
3. Noise, vibration and harshness.....	25
3.1. Sources of NVH.....	25
3.2. Transfer paths.....	26
3.3. Powertrain NVH .....	27
3.3.1. Shuffle.....	28
3.3.2. Driveline clonk.....	29
3.3.3. Gear rattle.....	29
3.3.4. Booming noise .....	30
4. Toolchain development.....	35
4.1. Software in Loop.....	36
4.1.1. Driver model .....	36
4.1.2. Control model .....	36
4.1.3. Plant and vehicle models.....	37
4.2. Initial powertrain model.....	37
4.2.1. Amesim model components.....	38
4.3. Coupling into the toolchain.....	42
4.3.1. SiL modifications.....	44
4.3.2. Powertrain model modifications .....	46
4.4. Evaluation of developed toolchain.....	46
5. Toolchain validation .....	47
5.1. Vehicle instrumentation .....	47

5.2.	Road load measurement .....	50
5.3.	Top-level validation .....	53
5.3.1.	Driving scenarios definition .....	53
5.3.2.	Measurement .....	54
5.3.3.	Evaluation .....	55
5.3.4.	Summary .....	65
5.4.	Low frequency validation .....	66
5.4.1.	Driving scenarios definition .....	66
5.4.2.	Measurement .....	67
5.4.3.	Evaluation .....	67
5.4.4.	Model improvements .....	70
5.4.5.	Summary .....	76
5.5.	Powertrain block movement validation .....	77
5.6.	High frequency validation .....	83
5.6.1.	Driving scenario definition .....	83
5.6.2.	Measurement .....	84
5.6.3.	Evaluation .....	84
5.6.4.	Model improvements .....	88
5.6.5.	Summary .....	100
6.	Model accuracy improvements .....	101
6.1.	SiL model improvements .....	101
6.2.	Powertrain model improvements .....	101
6.3.	Co-simulation level improvements .....	102
7.	Conclusion .....	104
	References .....	105
	List of abbreviations .....	108
	List of figures .....	110
	List of tables .....	113
	Attachments .....	113





# 1. Introduction

The automotive industry faces many challenges in the last decade. The governmental regulations are becoming more and more stringent so the car manufactures must adapt to the reality and develop new solutions for the cars. At the same time, they must meet the requirements and expectations of customers.

Passenger cars play very important role in people mobility while the conventional propulsion with an internal combustion engine is no longer able to comply all the upcoming CO<sub>2</sub> and emissions regulations. This brings a tough challenge for the industry and engineers.

There are several solutions of the propulsion system which can enable car manufactures to comply with upcoming regulations. Nowadays, some of the manufactures launch the battery electric vehicles (BEVs) mainly for their local zero emissions, the cost of BEV powertrain is still not competitive with the conventional. Hence the BEVs price remains still high even though they are widely supported by governments in many countries. Another limitation factor is the availability of the charging infrastructure and the charging time for restraining their usage. The recent development of the hydrogen fuel cell vehicles shows a convenient way to minimize some BEV disadvantages. Yet the price remains incomparably higher to the BEVs and conventional vehicles.

Hybrid electric vehicle (HEV), combining an internal combustion engine with one or more electric motors, seems to be a good compromise between the conventional vehicles and BEV. Compared to BEVs, they bring advantages in terms of their usable range, refuelling time and affordable price comparable with the conventional vehicles. HEV's efficiency is higher than the efficiency of the conventional vehicles in most of the driving cycles and hence acquiring the benefit of lower CO<sub>2</sub> and emissions production. The following figure 1 shows the increasing tendency of the sales of the passenger HEV's in the selected countries in the European Union (EU). The HEV's market share is expected to continuously in the following years.

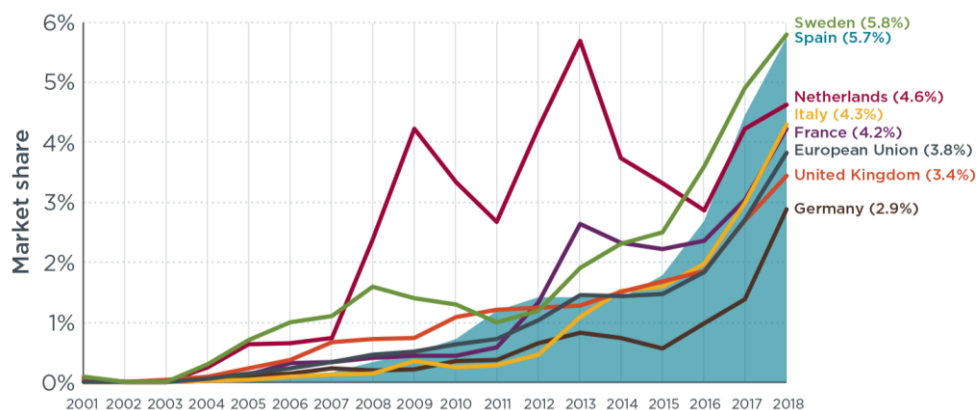


Figure 1 Market share of new HEV's in selected EU countries [1]

The electrification of the powertrain brings more costs to the vehicle, so the costs need to be optimized. The research and development of the vehicle is one the most expensive phase of a product life cycle. For this reason, the tendency is to cut down on the expenses during the development phase. One of the approaches is to minimize the number of tests on prototype vehicles and human resources using Computer Aided Engineering (CAE) tools in various stages of the vehicle development process. The other benefit is usually in a time save.

Besides the environmental and financial aspects, the passengers' comfort is another targeted point during the vehicle development process. The low level of noise and vibration (NV) contributes to a good perception of the car by the customer. The hybrid vehicles are susceptible to a distorted judgement as they switch frequently between the HEV and EV modes with a significant difference in NV level, caused by combustion engine operational mode. Therefore, the HEV's are subjected to an NV reduction with a high priority. The means of the NV reduction can be either car body or powertrain related. They can be either structural, or control based in case of the powertrain.

### 1.1.Motivation

Toyota introduced the first commercially successful hybrid car more than twenty years ago. Since that time, it spread the hybrid technology from one into many models in its range. By January 2017, 10.05 million Toyota hybrid cars had been produced as it can be seen in figure 2. Between 2015 and 2018, the sales of Toyota cars with the hybrid powertrain increased from 201 500 to 480 800 per year in Europe. The share of Toyota hybrid cars reached 46 % of total Toyota sales in Europe in 2018. [2, 3]

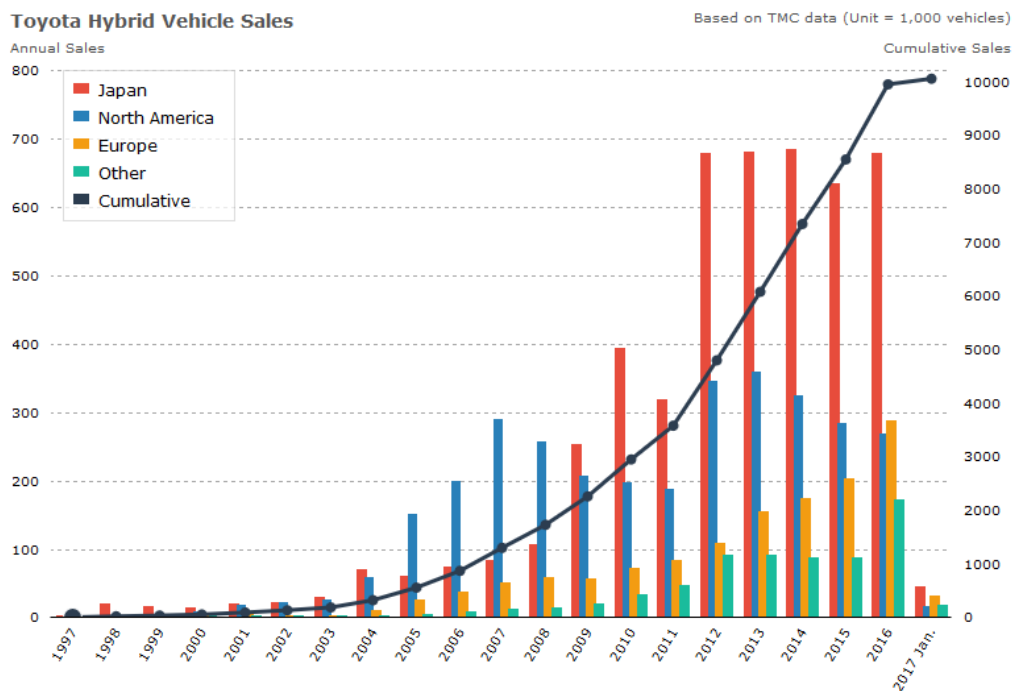


Figure 2 Toyota hybrid vehicle global sales [2]

As the HEV's have become a highly important part of Toyota model range, Toyota puts emphasis on the comfort improvement and hence the NV reduction. Toyota Hybrid System (THS) powertrain allows the control-based NV reduction. The calibration process takes place in the final stage of the vehicle's development process. This time-demanding calibration process is performed by a calibration engineer on a prototype vehicle. If the dedicated time period is exceeded, it can cause a delay of other processes of development and in the worst case a delay in launching the model to the market.

Using the Model-based Calibration (MBC) approach is favourable from two reasons. It can decrease the time needed for the calibration process by giving an idea of the HEV model behaviour or directly performing the calibration process on the HEV model. So far, the validation by a prototype vehicle is needed. The other advantage lies in the reduction of the testing time of the prototype, hence lower number of test vehicles needed, hence a reduction of costs.

One of the most critical NV in the powertrain is the low speed booming noise which has the origin in the combustion engine operated in the low engine speed under high load. Its occurrence can be avoided by a modification in the vehicle controls by the calibration process of THS. For the purpose of applying the MBC approach, no validated model of THS for low speed booming noise exists yet. Development of the model is a task for Model-based Design (MBD) department, and the process will be described in this work. It is also favourable to predict the booming noise phenomenon based on a driving cycle with an appropriate control of all the parts of hybrid system.

From these reasons, two already existing models built in two different software environments (LMS Amesim and MATLAB Simulink) were selected as the candidates for the low speed booming noise model. Each of the models has advantages but also limitations in terms of functionality and suitability as it will be described later. Therefore, it was decided to couple them into a toolchain.

When the toolchain model is completed, it is necessary to validate the toolchain accuracy in the validation process using the real test vehicle data. Three stages of the validation process were proposed to examine the performance of the model for the top-level performance, the low frequency and high frequency powertrain dynamics.

For each stage, the measurement conditions should be proposed, the measurement performed, the toolchain model run based on the same input and the results evaluated. Potential model accuracy improvements should be identified or implemented into the model if needed.

As the first step of this work, it is necessary to get familiar with the hybrid vehicles and NV problems.

## **2. Toyota Hybrid System**

Nowadays, the market with hybrid vehicles grows rapidly as it can be seen in figures 1 and 2. Toyota offers many hybrid models worldwide in its range with a target to offer every model with an electrified version. A development of a solution for a Toyota Hybrid System (THS) powertrain is the main objective of this work. Therefore, the hybrid vehicles architecture and THS will be described in the following chapter.

### **2.1.Introduction to hybrid vehicles architecture**

Hybrid vehicles (HV) are passenger or commercial vehicles which combine the conventional combustion engine with another source of energy used for the vehicle drive. They are usually categorized by several categories. The first is according to the physical principle of the auxiliary energy accumulator which stores and provides the energy for propulsion. It can be either mechanical (flywheel), compressive (pneumatic, hydro-pneumatics) or the most widespread electrical (battery, super-capacitor). Due to the fact, that the occurrence of the mechanical and compressive storage principles is practically zero in passenger vehicles, only the hybrid electric vehicles (HEV) will be subjected in this chapter.

#### **2.1.1. Level of hybridization**

The second category is the level of hybridization of the powertrain and its function. We can distinguish between micro hybrids, mild hybrids, full hybrids and plug-in hybrids.

##### **Micro hybrid**

Micro hybrid is a vehicle with the reinforced electrical accessories (battery, starter, alternator) and the engine start-stop system. They help to save the fuel when the conventional engine would be idling. Micro hybrid can also recover the kinetic energy from the braking or coasting manoeuvres to batteries through the alternator to a limited extent. It is often equipped with the Belt Alternator Starter (BAS) which is the alternator with an integrated function of the starter. The voltage is usually between 12 and 48 V, the motor does not provide more than 5 kW.

##### **Mild hybrid**

Mild hybrid drive supports the engine with an electric motor during acceleration or high load. The fully electric drive is not possible in any mild hybrid vehicle. In some mild hybrid architectures, purely electric creeping or reverse is possible. The electric energy is obtained either from recuperation or charging by engine. The power voltage is in a range between 42 and 144 V, the electric motor usually provides up to 15 kW and the battery capacity is usually less than 2 kWh.

## Full hybrid

Full hybrid allows fully electric drive of the vehicle with a maximum range in units of km. The motor is usually used for the start-up, up to a reasonably high-mid speed, e.g. 80 km/h, driving and boosting the engine during the acceleration and high load. The battery voltage is usually between 200 and 300 V, the power of motor is more than 30 kW, the battery capacity usually does not exceed 2 kWh.

## Plug-in hybrid

Plug-in hybrid is a full hybrid with a possibility of charging the battery from an external source or the electricity network. The battery capacity and power of the engine is higher than for the full hybrid.

### 2.1.2. Hybrid vehicles architecture

The third category is the structural arrangement of the powertrain. It can be divided into series hybrids, parallel hybrids and power-split hybrids. Another possibility is the axle split hybrid drive when the combustion engine drives one axle and the electric motor the second axle.

## Series hybrid

The series hybrids employ the scheme where the combustion engines and two electric motors are connected in series. There is no mechanical connection between the engine and wheels. The engine is directly connected to one motor which serves as a generator and produces electrical power. The power flows into the inverter. The inverter logic can decide whether the power flows to batteries or directly to the second motor which serves as the drive unit. When the battery is sufficiently charged, the logic can turn off the combustion engine and the motor is supplied from the battery. During braking, the motor recuperates the energy. The scheme of series hybrid system can be observed in the following figure 3.

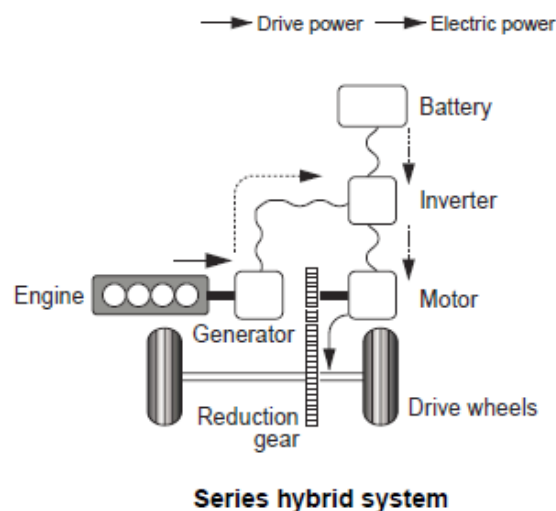


Figure 3 Series hybrid layout [4]

The combustion engine is always operated in the best efficiency conditions. In spite of the Battery Electric Vehicles (BEV) with a range extender, the combustion engine must be dimensioned to produce enough power for the vehicle drive when the state of charge of the battery is low. The generator also serves as the engine starter.

### Parallel hybrid

The parallel hybrid uses a combination of the combustion engine and usually one electric motor. The electric motor always works in one mode only. In the motoric regime, the electric motor draws power from the batteries and supports the combustion engine during the acceleration and higher load or drives alone in case of full hybrid. In generator regime, it either recuperates energy or charges the battery by the engine. The drivetrain commonly comprises of a conventional transmission (manual, automatic, CVT) and a clutch in some cases to fully disengage the engine. The scheme of the parallel hybrid system can be seen in figure 4.

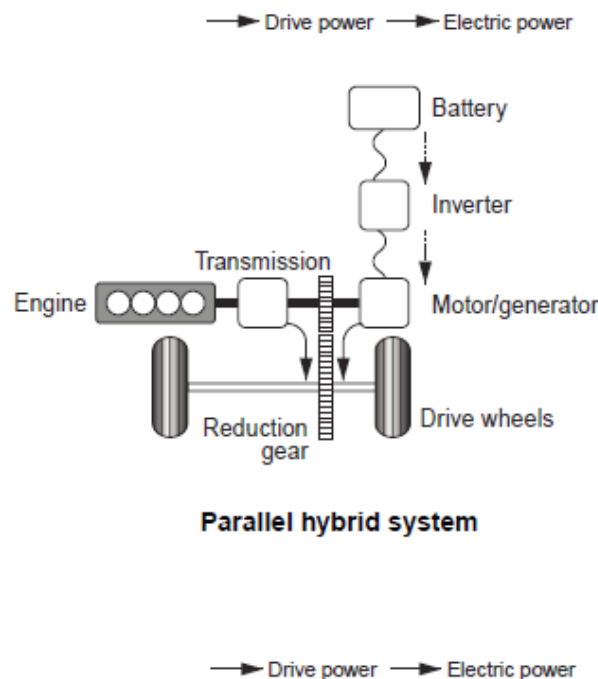


Figure 4 Parallel hybrid layout [4]

In general, it is structurally simpler than the series hybrid, but it is not possible to power the wheels by motor and charge the battery at the same time. On the other hand, this configuration of parallel hybrid is closer to the conventional powertrain and allows its relatively simple hybridization. The electric motor can be attached to the powertrain in many different locations as shown in the figure 5.

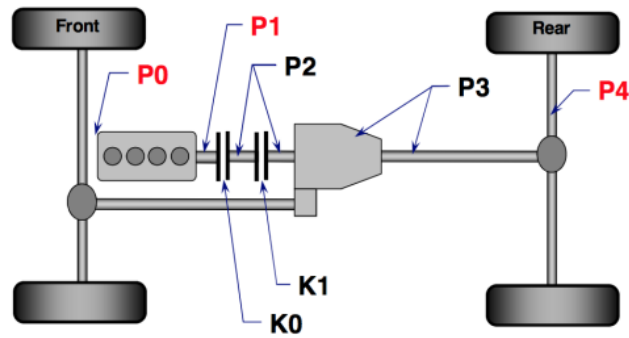


Figure 5 Location of electric motor in mild hybrid powertrain [5]

The P0 architecture, when the motor is attached via belt on the accessory side of the engine, is common for micro hybrids. It does not allow high power boosting for driving, mostly operates the engine (BAS). Also, P1 architecture with the motor mounted on the crankshaft is typical for micro hybrids, alternatively for mild hybrids. The motor mostly works as Integrated Starter Generator (ISG). In the case of mild hybrid, it can provide only limited support to the engine.

For P2, P3 and P4 architectures, the electric motor is located after the clutch. It can be mounted either on transmission input (P2) or output (P3, P4). Electric motor can be attached directly on the shaft or via permanent gear (two-shaft parallel hybrid). These configurations take advantage of direct connection to the wheel and the ability to use most of the energy for recuperation during braking. Despite to P0 and P1 architectures, the vehicle allows fully electric drive without employing the engine.

Another architecture of parallel hybrid uses two electric motors. One attached to the crankshaft before clutch and the other after. Thanks to this, the engine can supply power for driving and battery can be charged at the same time.

### Power-split hybrid

The power-split hybrid, also called a series/parallel hybrid, comprises of the combustion engine and two electric motors as shown in figure 6. One is coupled with combustion engine through the power-split device (planetary gear set) and mostly serves as a generator or controls the engine. The second motor is directly coupled with the final drive or transmission and drives wheels but also generates power during the steady speed driving or coasting manoeuvres. There are several ways of connections of power-split unit and the final drive. In this architecture, there is typically no clutch or conventional transmission. Indeed, the main purpose of the first motor is to vary the ratio between the combustion engine and the wheels known as e-CVT.



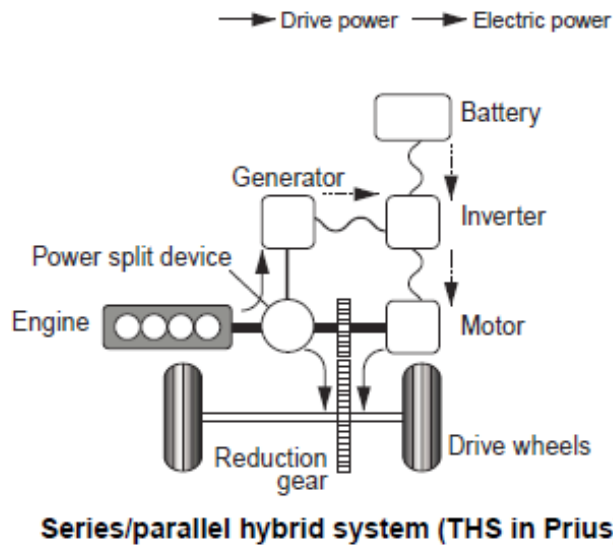


Figure 6 Power-split hybrid layout [4]

Toyota launched the first production hybrid vehicle known as Prius with this technology called Toyota Hybrid System (THS) in 1997. Since that time, the system underwent several structural changes and nowadays it is offered in the fourth generation. This system is the main subject of this work and will be explained in detail in the next chapter.

## 2.2. Toyota Hybrid System Gen4

The fourth generation (Gen4) of THS underwent some modifications towards the previous third generation. The scheme of Gen4 can be seen in figure 7. The powertrain consists of a combustion engine, two electric motors/generators MG1 (12) and MG2 (9), the power-split gear unit (14) and countershaft with counter driven gear (7) and final drive gear (5). Power-split unit consists of a planetary gear set with an external geared ring– counter drive gear (10), also called a propeller shaft. MG2 is linked to the countershaft via the MG2 reduction gear (8).

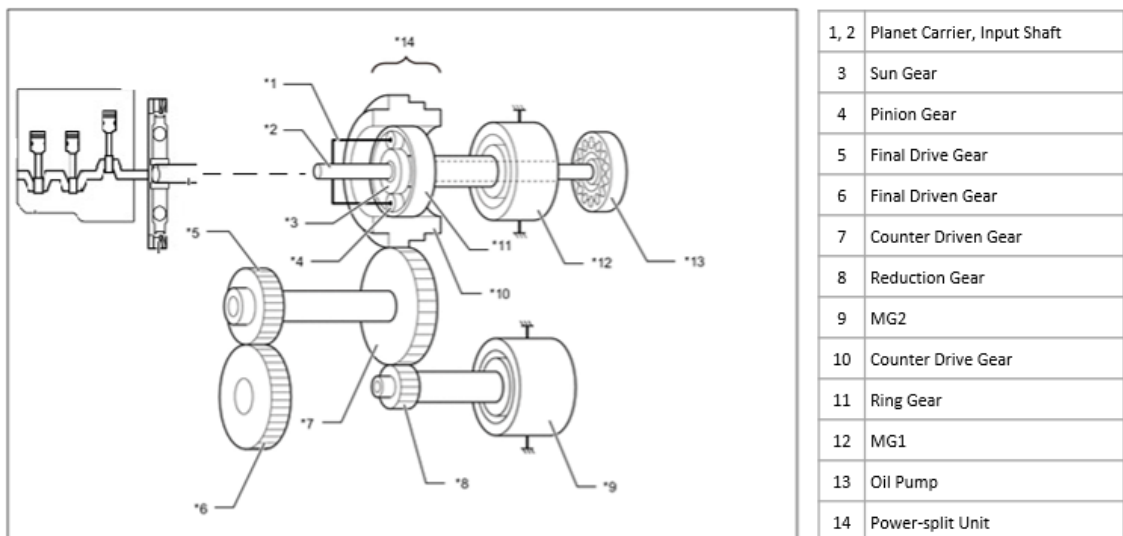


Figure 7 Scheme of THS Gen4 [6]

## Engine

The engine is a naturally aspirated gasoline inline four-cylinder engine. It works in an Atkinson cycle which allows operation with higher efficiency than the conventional Otto cycle. The Atkinson cycle is a type of an over-expanded cycle developed by a British engineer James Atkinson.

The gas pressure inside the cylinder of a conventional engine at a point of exhaust valve opening is greater than the exhaust port pressure. The energy, which is still available at this point in the gas, is usually dissipated during the blow down process. The prolongation of the expansion period within the cylinder would furthermore increase the indicated work per cycle and hence the efficiency. This is called the Atkinson cycle. The comparison of p-V and T-s diagrams with Otto cycle can be seen in the following figure 8. [7]

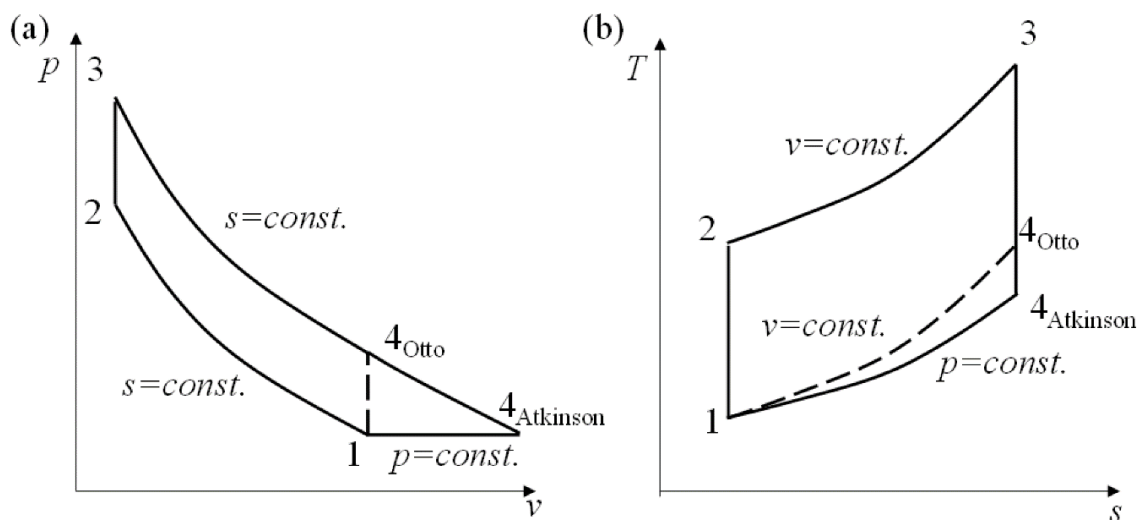


Figure 8 Otto and Atkinson cycles p-V (a) and T-s (b) diagrams [8]

Originally, the Atkinson cycle was achieved by a complex crankshaft mechanism. Nowadays, the solution of the Atkinson cycle is usually different. It is commonly applied as a modification of the Otto cycle with a different valve timing. The main idea consists of different lengths of the intake and exhaust phases. The intake valve is held open longer and closes in the compression stroke after bottom dead centre (BDC). It allows the reverse flow of the air or charge back to the intake manifold – backflow. It decreases the time of the compression phase when being compared to the conventional Otto cycle. [7]

This reverse flow decreases the amount of charge in the cylinder and the in-cylinder pressure after the compression stroke. With the same geometrical compression ratio as in the Otto cycle, the effective compression ratio is lower. At the same time, the expansion ratio is not changed. So, the expansion ratio is greater than the compression ratio in Atkinson cycle as can be seen in figure 9. Therefore, the thermal efficiency is higher and the specific fuel consumption lower in the engines using this technology.

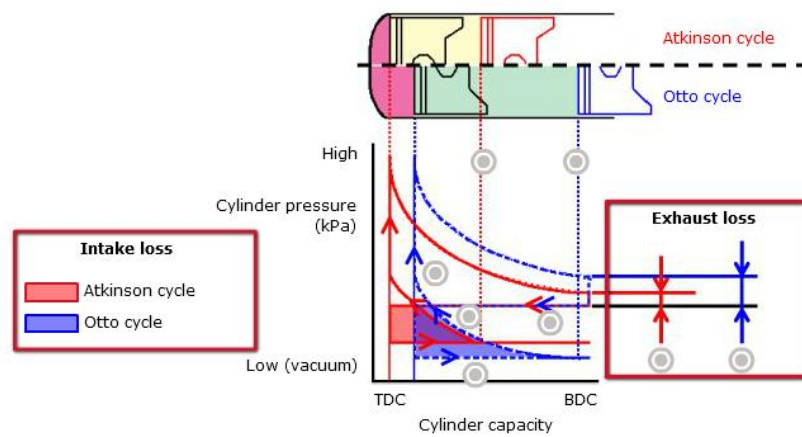


Figure 9 p-V diagram of Atkinson cycle in the conventional reciprocating engine [9]

On the other hand, as the effective compression ratio is lower, the amount of charge for combustion is smaller and hence the torque output is lower than for the Otto cycle engine of the same size. For this reason, the engines with Atkinson cycle are usually equipped with Variable Valve Timing (VVT) in order to vary the effective compression ratio and allow the engine to work in either the high fuel efficiency or the high-performance modes. The specification of the engine is shown in table 1.

Table 1 Toyota CH-R Hybrid 1.8L engine characteristics [6]

	Unit	Value
Displacement	cm <sup>3</sup>	1,798
Compression ratio – geometrical	1	13.04:1
Bore	mm	80.5
Stroke	mm	88.3
Maximum torque (at engine speed)	Nm	142 (3600 rpm)
Maximum power (at engine speed)	kW	72 (5200 rpm)

## Electric motors

THS consists of two electric motors/generators, called MG1 and MG2. Both of them are frequency controlled, synchronous brushless Alternating Current (AC) motors with a permanent magnets rotor [9]

MG1 has several functions. Primarily it serves as a generator. It can either charge the battery or supply electrical power for the MG2. It also starts up and stops the engine. It has the controlling function in the power-split unit. By varying the power generated, it controls the gear ratio between the combustion engine and the propeller shaft, whose speed is directly connected to the wheels. This technology is known as a Continuously Variable Transmission (e-CVT). The regimes of operation will be discussed in the following chapter.

MG2 mostly provides power to the system for the vehicle propulsion and recuperates the kinetic energy of the vehicle during the regenerative braking or the coasting manoeuvres and stores it into the battery.

In some cases, in the steady speed driving, it can also draw the power from the engine and additionally charge the battery when the MG1 charging power limit is reached. In the case of electric vehicle (EV) mode, MG2 is the only source of power. The specification of the motor/generators is shown in table 2.

Table 2 MG1 and MG2 characteristics [6]

	Unit	MG1	MG2
Maximum torque	Nm	50	163
Maximum power	kW	40	53

MG1 and MG2 are connected to the Power Control Unit (PCU). The overall scheme of the high voltage electric part of THS can be seen in the following figure 10.

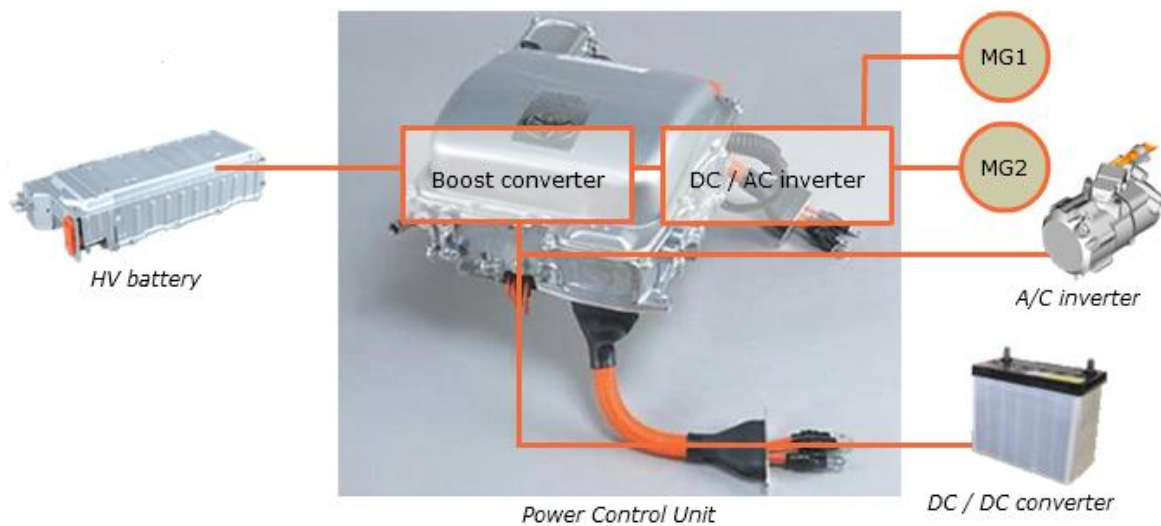


Figure 10 High voltage layout [9]

The PCU consists of a DC/AC inverter and a boost converter. It controls the power flow between MGs and the HV battery. The DC battery voltage is approximately 200 V while the voltage of motors is around 500 V. Therefore, the boost converter, which transforms the battery voltage to the voltage needed in the DC/AC inverter, is upstream to it. Thanks to the lower current, the inverter can be smaller with a lower weight. Two more devices are linked to the boost converter. It is the A/C inverter which supplies power to the compressor of the air-conditioning unit since it must work also in EV mode when it cannot be run by the accessory belt as in the conventional vehicle. The second device is the DC converter which can support the 12 V accessory battery in the vehicle. [6]

### Hybrid vehicle damper

In most of conventional vehicles, the engine crankshaft is connected to the flywheel and further to a clutch or a torque converter in the case of a manual or an automatic transmission, respectively. The coil-spring clutch or the hydrodynamic torque converter usually smoothens the torque fluctuations

originated in the engine. In a vehicle with THS, no clutch or torque converter is needed since the gear ratio is varied by the transaxle. As a side effect, the damping effect is not present, therefore the flywheel is connected to the carrier of transaxle through a torsional damper, called hybrid vehicle damper (HV damper). It is a coil-spring single plate damper which is attached to the flywheel. It also contains stoppers with much higher stiffness for a case of overloading when the compression of coil springs is depleted. The scheme can be observed in the following figure 11.

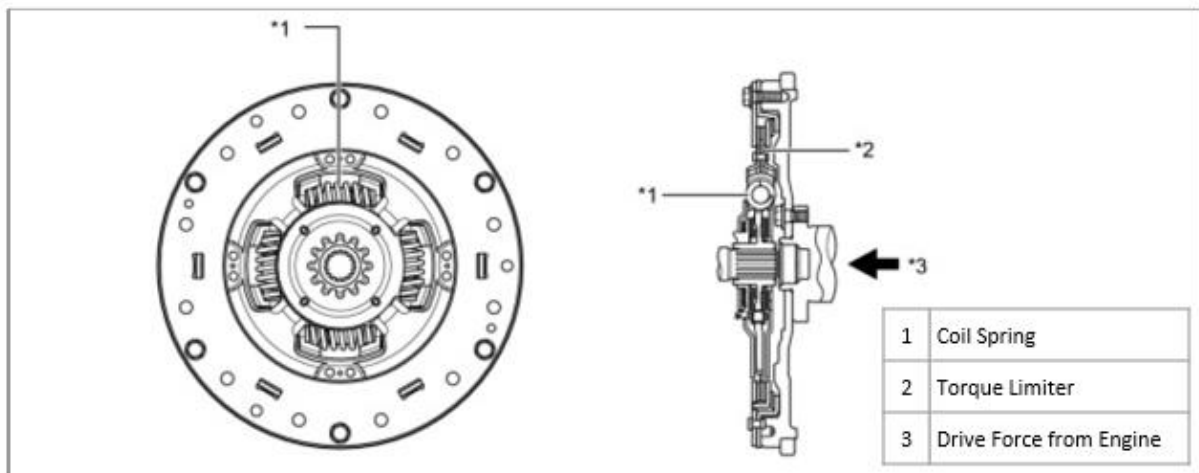


Figure 11 HV damper [9]

### Electronic Continuously Variable Transmission (e-CVT)

As it has been mentioned above, the THS does not include any conventional type of transmission (manual, automatic, automatized or Continuously Variable Transmission – CVT) but the gear ratio between the combustion engine and wheels is varied by a planetary gear set and operating strategy. Despite geared transmission, the e-CVT provides an infinite number of gear ratios. Thanks to that, the engine can be operated in the area of lowest fuel consumption. Classical automotive CVT with a belt drive allows some slip of the belt, therefore the loss is significantly higher than for the geared transmissions. Efficiency of a classical CVT is usually from 89 % to 94 % at full load. In e-CVT transmission, only a combination of a planetary gear set and MG1 is used, therefore the efficiency is comparable with geared transmissions. [10]

The planetary gear set, also called power-split unit, consists of several parts. The input of engine torque comes from the planet carrier shaft, which is linked to hybrid damper. The sun gear is a part of the input shaft of MG1 and incorporates MG1 rotor. Next to the internal gearing of the ring gear (propeller shaft), it also includes external gearing, which serves as the output from transaxle. The torque flows then through the countershaft and the differential to the driveshafts and wheels through the fixed gear ratios. The speed of the propeller shaft is therefore directly linked to the vehicle speed.

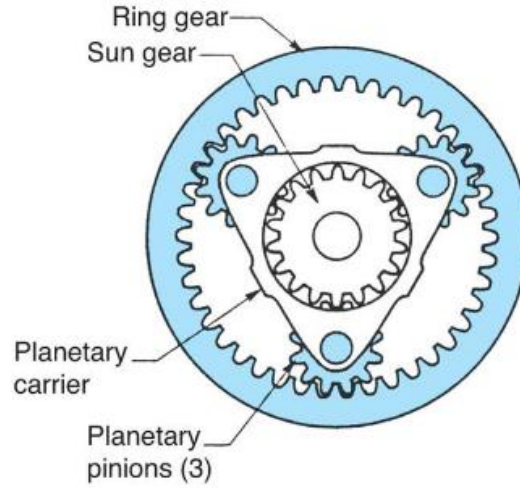


Figure 12 Planetary gear set [11]

The planetary gear set, as depicted in figure 12, has two degrees of freedom that means that the speeds of two parts are always independent on the third one. In the case of THS, the speed of the propeller shaft corresponds to the vehicle speed and speed of the engine and MG1 are variable. Speeds follow the basic kinematic equation:

$$(1 - i) \cdot \omega_c = (-i) \cdot \omega_s + \omega_r \quad (1)$$

where  $\omega_c$  is rotational speed of carrier,  $\omega_s$  is speed of sun gear,  $\omega_r$  is speed of ring gear  $i$  is base gear ratio, which can be determined as:

$$i = \frac{z_r}{z_s} \cdot (-1)^j \quad (2)$$

where  $z_r$  is number of teeth of ring gear,  $z_s$  is number of teeth of sun gear and  $j$  is number of external gears meshes. The corresponding relations for moments are:

$$\begin{cases} M_s = -M_c \cdot \frac{i}{1+i} \\ M_r = -M_c \cdot \frac{1}{1+i} \end{cases} \quad (3)$$

### 2.2.1. Working principles

Now, when it is clear, which components THS contains and how e-CVT works, the interest can be aimed at the working principals of THS. The basic driving modes will be explained. The advanced powertrain management is fundamental to fulfil the advantage of the hybrid vehicle. The operational conditions always depend on the acceleration, braking or charging of the vehicle. The operational point of the engine is optimized for the lowest fuel consumption. Nevertheless, there are other conditions or limitations, which can modify the operational point.

## Take off

In the beginning, when the vehicle is stopped and the battery is sufficiently charged, MG2 is used only for vehicle take off after a command for a mild acceleration. It means the vehicle is run in EV mode, when the engine is stopped in order not to let the engine freely rotate and not to introduce friction losses. As the vehicle speed increases, the engine is kept stopped by increasing MG1 speed. MG1 is freely rotating and does not generate power. The relation (1) must be satisfied. In this case,  $\omega_r$  equals to propeller shaft speed (proportional to vehicle speed),  $\omega_c$  equals to engine speed and  $\omega_s$  equals to MG1 speed. For easier understanding, the graphical method – nomographic chart – shows the situation in figure 13.

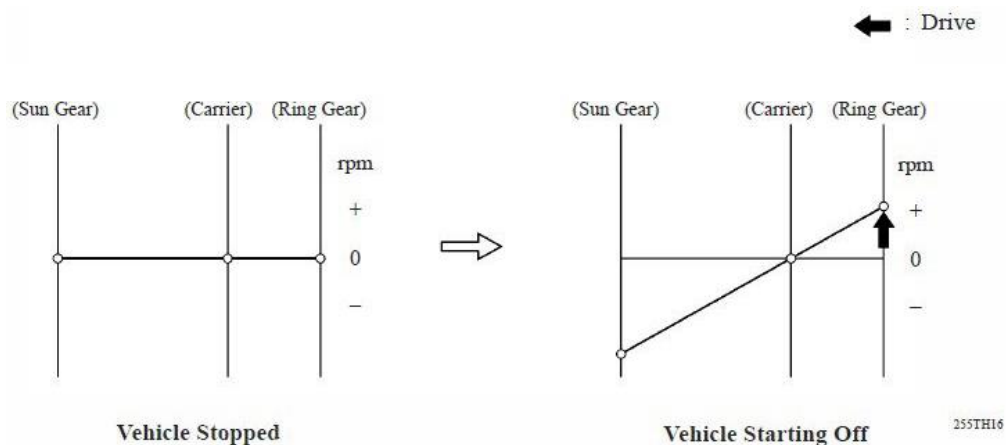


Figure 13 Nomographic chart of vehicle taking off [12]

## Engine start up

The engine must be started up from two reasons during driving. The first case is when the command for acceleration is high so the combustion engine must be started up to satisfy the driving power requirements. The second case is when MG1 approaches its speed limit. Then MG1 provides positive torque for a short time to start up the engine and changes the sense of rotation. The engine is driven by MG1 to idling speed until it provides torque for self-accelerating torque as shown in figure 14.

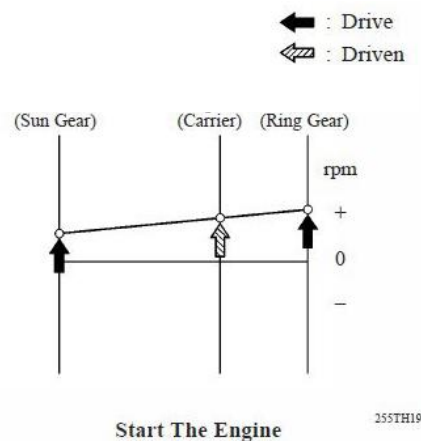


Figure 14 Nomographic chart of engine starting up [12]

## Generating electricity during driving

The THS can generate electric power by MG1 during driving when the engine is on. The power can be distributed either to batteries and stored or to support MG2, when the system evaluates this power distribution as more efficient. The situation is shown in figure 15.

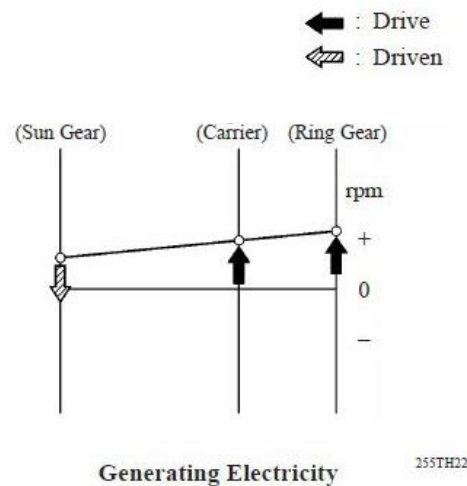


Figure 15 Nomographic chart of electricity generation during driving [12]

## Generating electricity when stopped

When the vehicle is stopped and the battery state of charge (SOC) is low after launching, the battery can be charge. MG1 starts up the engine first and when the engine is on, it provides power to MG1 which generates electricity for HV battery. It can be observed in figure 16.

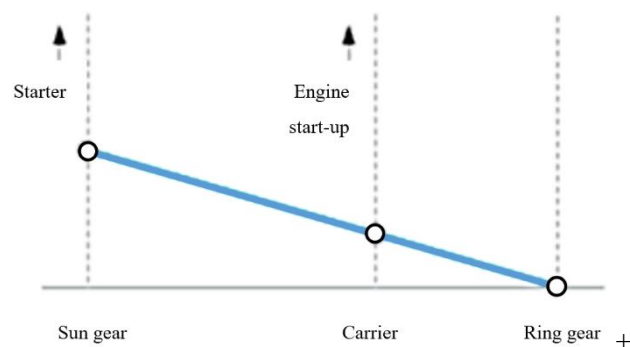


Figure 16 Nomographic chart of electricity generation when vehicle stopped [13]

## Deceleration and braking

During deceleration, MG2 starts recuperating energy and stores it in the battery. The combustion engine is controlled independently on vehicle speed by MG1 and it is immediately switched off after the accelerator pedal tip-out, in case the battery SOC is not too low. Despite a conventional, non-hybrid vehicle, it uses primarily the recuperating MG2 to slow down the vehicle instead of breaks. This contributes to high overall efficiency of a hybrid vehicle and decreases the usage of brakes.



A simple driving scenario can be seen in figure 17. It shows the difference in energy management between a conventional non-hybrid vehicle and a vehicle with the THS.

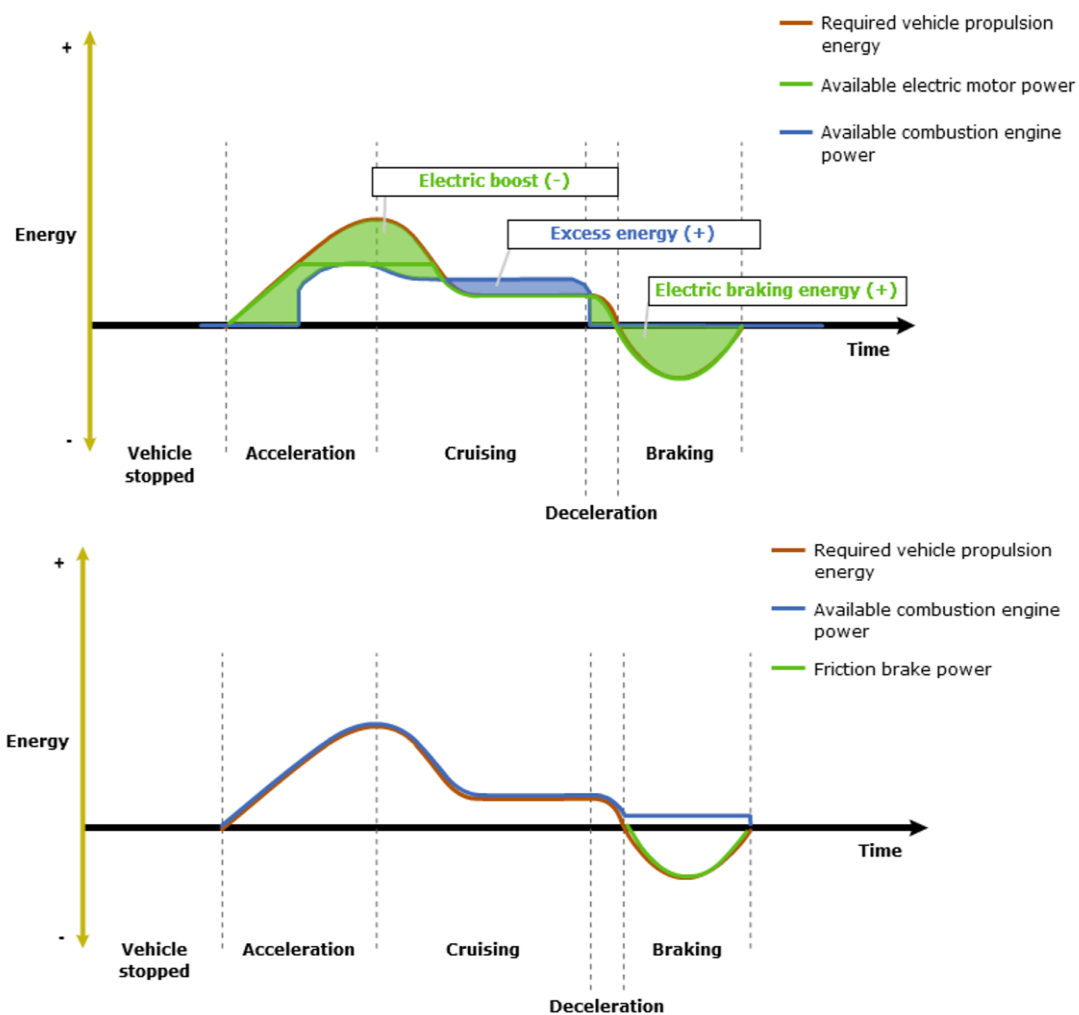


Figure 17 Comparison between THS and non-hybrid powertrain behaviour in a simple driving cycle [9]

During the first acceleration phase, only MG2 is used for vehicle drive. The combustion engine is started up with a delay, when MG2 power is not enough. In the cruising phase, the engine co-drives with MG2 and is run in the area with the lowest fuel consumption so the excess energy is used for electricity generation through MG1. In the deceleration phase, the engine is quickly turned off and does not create additional losses. MG2 starts regenerating the energy. In a conventional vehicle, the engine must be still running for a possible re-acceleration, so that it can immediately provide energy for re-acceleration from safety reasons. This is not necessary in a hybrid vehicle, the first demand would be covered by MG2. During mild braking, all the energy can be reused instead of being dissipated by brakes or engine friction. In comparison, the sum of green areas represents the energy gain of energy against the non-hybrid vehicle.

### 3. Noise, vibration and harshness

The level and quality of the noise, vibration and harshness phenomena (NVH) is one the most important criteria for how the passenger judges his driving experience. The passenger, which is a part of the vibro-acoustical system of the vehicle cabin, perceives the disturbances mostly negatively. Therefore, the NVH problematic plays an important role during the designing phase of the vehicle in order to avoid them or minimize the impact. The noise can be caused by several sources and transferred to the passenger's ear by two mechanisms as shown in figure 18. [14, 15]

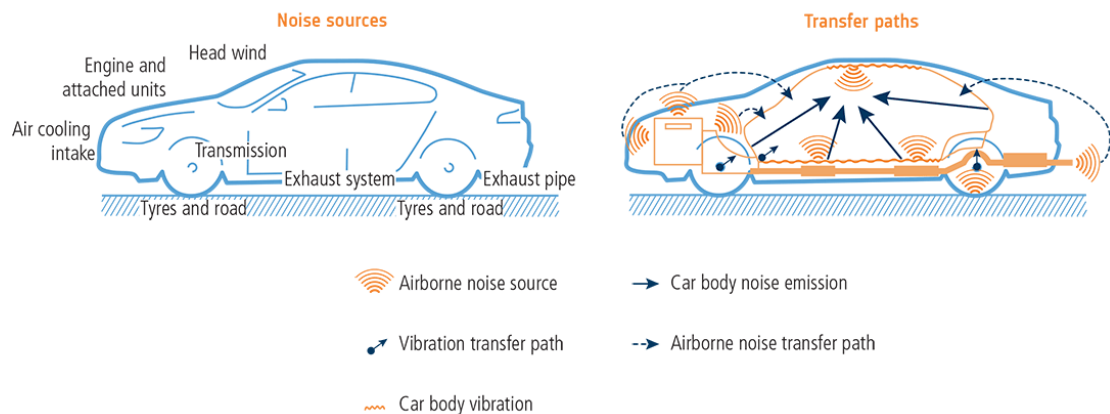


Figure 18 Noise sources and transfer paths [16]

#### 3.1.Sources of NVH

Three physical principles of the NVH origin in the passenger vehicle can be found: aero-acoustic, electro-magnetic and mechanical.

##### Aero-acoustic source

The aero-acoustic noise is always originated on the boundary of a fluid and a structure. It can be divided into three groups. The first one is due to the pulsating volume of a fluid causing the pressure oscillation (monopole), e.g. intake/exhaust pipe, turbocharger, etc. The second one is due to a fluctuating force acting on the panels of the vehicle by a flow separation (dipole), e.g. side-mirrors, roof luggage rack, etc. The third one originates due to a momentum transfer in a turbulent flow – wind noise (quadrupole).

The fluctuations are spread from the body panels to the cabin through the body structure. In the electric or hybrid vehicles this phenomenon becomes very important since the other phenomena might be much weaker or not present. The optimization of the body design is crucial in order to minimize the noise as well as the resistance of the vehicle and hence the fuel consumption. [17]

### Electro-magnetic source

In the passenger vehicles, the electric machines are the main source of electro-magnetic noise. The alternating current is the cause of fluctuating electro-magnetic forces coming from the air gap of the electric motor. Although the electro-magnetic noise may become dominant in the electric and hybrid vehicles, it is not the object of interest of this work and will not be expanded anymore. [17]

### Mechanical source

The noise is often caused by a mechanical source. One type of mechanical sources is introduced by time varying inertia forces caused by unbalances of the rotating parts or unevenly moving parts. The noise usually comes from the powertrain parts, e.g. combustion engine, transmission, driveshafts, etc. The other type is caused by contact forces in gears, bearings and tire-road constant. The roughness and unevenness of the surface cause force fluctuations between two parts. The mechanical powertrain based NVH is the main topic of this work and will be discussed further. [17]

## 3.2. Transfer paths

There are two main mechanisms of the transfer of acoustic and vibrations energy from the source to the passenger. It can be through a fluid or solid medium. They are usually referred to as the air-borne mechanism and the structure-borne mechanism.

The composition of the sound spectrum is partly from the air-borne and structure-borne contributions. The transition region between these two mechanisms is usually around 500 Hz as it can be seen in figure 19. In the region between 200 and 1000 Hz, both mechanisms are mostly present. [17]

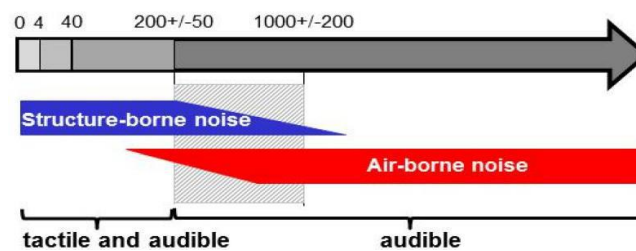


Figure 19 Transition region between structure-borne and air-borne noise [18]

### Air-borne mechanism

Air-borne mechanism can be characterized as an acoustic energy transfer in a form of sound waves through the fluid medium, e.g. air. The mechanism prevails the structure-borne mechanism in interior noise in frequencies over 500 Hz. [17]

### Structure-borne mechanism

Structure-borne noise transmission consists of a vibrational energy transfer from a source to the cabin along structural paths through a solid medium. Of course, all the noise, which is propagated via the

solid structures, must eventually become the air-borne sound and be radiated from a surface as an audible noise. The main contribution to interior noise is usually in a range below 500 Hz. [18, 19]

The vibration energy from the powertrain is transferred through driveshafts, suspension system and car-body structure to the passenger. Along the path, the energy is partly dissipated in the powertrain mounts, dampers and by the structural damping of the vehicle components. The structure-borne transfer path is shown in figure 20.

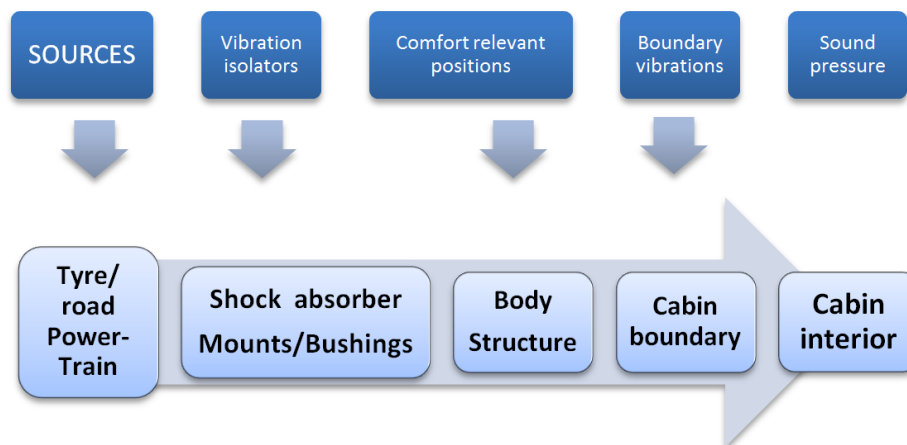


Figure 20 Structure-borne transfer path [18]

### 3.3. Powertrain NVH

As has been mentioned above, the powertrain is one of two main sources of the mechanical NVH. The improvements recently achieved in the lower fuel consumption, higher efficiency and lower exhaust gas emissions led to an emergence of the number of powertrain related NVH concerns. They are mostly the result of a lightweight and fuel-efficient drivetrain. The main contributors of the growing NVH importance are the following:

- Decreasing the number of cylinders of the combustion engines.
- Cylinder-deactivation technology.
- Vehicle performance is more responsive, the rates of engine torque increase are higher.
- Engine and driveline lubricants are generally less viscous and must resist higher temperatures and pressure levels.
- The power-to-weight ratio of vehicles has increased over time.
- The intrinsic damping level of lightweight materials is lower.
- The other vehicle NVHs (aerodynamic noise) have decreased.
- Expectations of customers have increased over time.
- Hybrid vehicles are quieter in EV mode and therefore the NVH level of EV and HEV modes should be kept close, so it is not disturbing to customers because of the frequent switching.

As a result, the powertrain NVH reduction needs more attention than ever before. The noises are mostly excited by two mechanisms: the engine combustion or the contact related, followed by the energy dissipation into a nearby resonating structure. These phenomena appear under different conditions and they have different frequency characteristics as can be seen in the following figure 21.

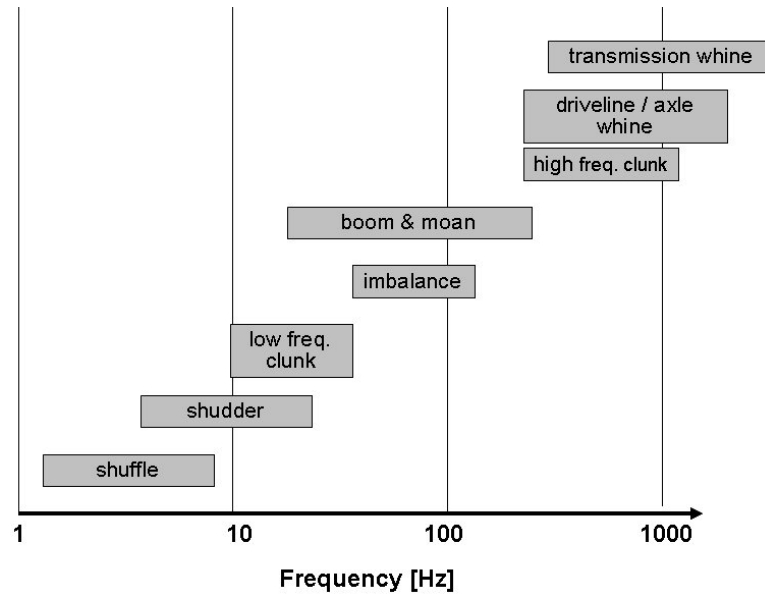


Figure 21 Typical frequency range of different powertrain NVH [20]

However, they all share and respond to a similar generic trait. Both types of sources (combustion and contact) are complex with several orders of vibrations, the transfer paths are complex and non-linear torsional spring and damper systems and they contribute to different forms of energy dissipation (air-borne and structure-borne). In order to obtain a full frequency spectrum of vibrations (Fourier spectrum), the system can be excited by a Dirac impulse. Then all modes of an elastic structure will be excited. [19]

The typical NVH in the vehicle with the THS powertrain will be briefly introduced now.

### 3.3.1. Shuffle

Shuffle is a low frequency phenomenon, which can occur after a harsh tip-in or tip-out. It is characterised by a fore and aft undamped vehicle vibration. It can continue with several cycles. The oscillations can be accompanied by a driveline clunk. In the vehicles with THS this might be a problem as the maximum MG2 torque is available immediately after the tip-in.

Shuffle can be avoided by a very slow rise of the applied driving torque. However, this would not be acceptable from the ‘fun to drive’ reason. In the THS, the calibration of MG2 torque rise and profile is necessary and a compromise must be found. Alternatively, shuffle can be reduced by increasing the driveline damping but this technique is not so effective as by improving the controls. [19]

### 3.3.2. Driveline clonk

Driveline clonk is an audible noise as a response to a sudden change when the lashes in the system are present. It can occur during several driving manoeuvres:

- Tip-out clonk, when the accelerator pedal is suddenly released.
- Engagement clonk, when the clutch is engaged quickly.
- Clutch clonk, when a sudden supply of torque is applied in a low-speed manoeuvre.
- Shift clonk, due to shifting a gear.
- Over-run clonk, when the impulse comes from the road disturbance through the drivetrain.

Clonk is always related to the shuffle, torsional low frequency oscillations. Clonk can be heard usually on the first cycle of shuffle response. It is mostly excited by a single torsional impulse which is followed by a short duration vehicle jerk and a metallic noise. The low frequency shuffle mostly follows. In some cases, multiple clonks may occur with every cycle of the shuffle cycle. The typical frequency range of clonk is from 300 to 4000 Hz, 3 to 7 Hz for shuffle, respectively. The clonk duration varies from 0.25 to 5 ms. [19, 21]

### 3.3.3. Gear rattle

Gear rattle is a metallic noise which is created in a gear mesh. It is originated due to the backlash and unloading and loading the gear. When the gear is unloaded, the teeth exceed the gear inertia and the oil drag so the contact between these two parts is lost (figure 22 (a) and (b)). When the torque is applied again, the teeth collide with each other and create the noise (figure 22 (c)). [19]

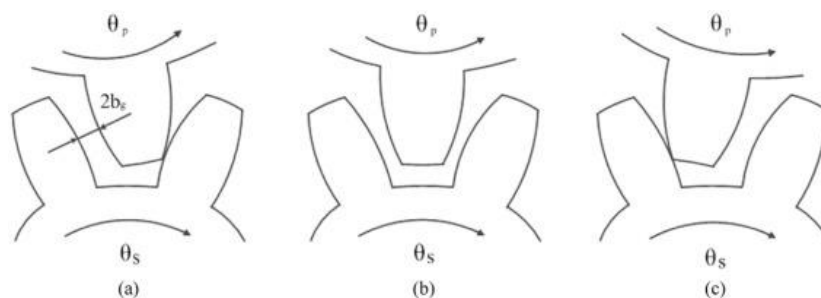


Figure 22 Gear rattle origin [22]

The gear rattle occurrence strongly depends on the relative speed between gears in the mesh, oil temperature and viscosity. It is transferred by the structure-borne and air-borne mechanism. In both cases, the vibrations are transferred into the gear housing and further either radiated or transmitted through the transmission, powertrain block and powertrain mounts to the car body.

Recently, due to lightweight drivetrain structure, low viscosity oil, higher engine performance and lower background noise levels, the rattle is a more serious issue in the powertrain NVH. [19]

There are several drive modes when the gear rattle occurs. [21]

- Idle rattle, which occurs when the vehicle stands still, and the engine speed oscillations are not well damped. Then the gears can approach and create the noise.
- Drive rattle, which occurs in drive mode when the transmission oil is hot (low viscosity) and gears are suddenly engaged.
- Coast rattle, which occurs in coasting after the throttle is closed.

In the THS, rattle usually occurs during the tip-in or tip-out when MG2 changes the mode from driving to recuperation and vice versa. The rise rate of torque is limited to minimize the effect. The MG1 contributes to the gear rattle when it changes the sense of rotation and torque performance during the engine starting up and stopping.

### 3.3.4. Booming noise

Booming noise is an undesirable low frequency noise in the vehicle cabin, which can dominate the overall vehicle noise. It originates in the engine combustion, e.g. combustion (pressure) forces and cranktrain inertia forces. Boom is transmitted by both mechanisms – structure-borne and air-borne. The air-borne is mostly represented by the intake and exhaust pressure waves. We can also observe two main possible structure-borne paths of booming noise. The first one, as a result of the engine block vibrations, which transfers the oscillations by the powertrain mounts to the car body structure. The second one is, when the engine torque fluctuations propagate through the drivetrain. The driveshafts oscillate and via the wheel knuckles and the suspension bushing, the vehicle body is excited. In the end, the vibrations of the structure are radiated as an audible sound. The booming noise source and transfer parts are shown in figure 23. [19, 23]

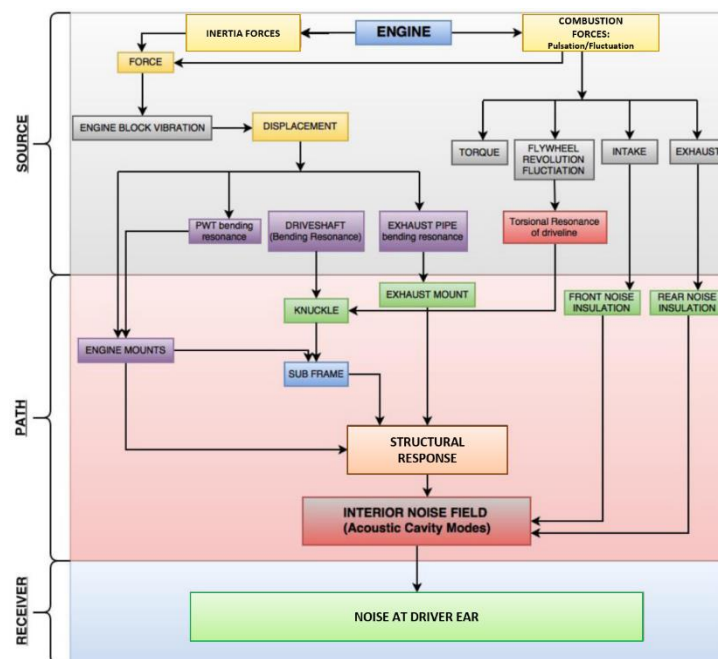


Figure 23 Source-Path-Receiver scheme of booming noise [23]

The booming noise occurs when the body or interior panels are excited into the resonance by the frequency of the booming noise – the combustion frequency. Then the acoustic mode of the body cavity is reached. The combustion frequency can be easily determined from the engine speed  $Ne$  in equation (4). For a conventional four-cylinder engine, there are two cylinders firing per revolution:

$$f_{comb} = \frac{Ne}{30} [Hz, rpm] \quad (4)$$

where  $f_{comb}$  is combustion frequency and  $Ne$  is engine speed.

For the front wheel drive vehicles with a transversal engine, the 1<sup>st</sup> order boom is dominant but higher orders (2, 4, etc.) may appear, too. The low-frequency acoustic cavity modes are barely audible, causing a pressure undulation discomfort in ears. The higher modes are driven by vibrations of panels. [19, 23]

The drivetrain structure-borne booming noise reduction is the main topic of this work. At first, the strategies of booming noise avoidance will be described.

### **Strategies of booming noise avoidance**

There are several countermeasures how to avoid or suppress the booming noise. It can be minimized either by structural changes, by passive noise control, active noise control or by modifications of the operational point of the source (engine).

### **Structural optimization of vehicle design**

The first, most conventional countermeasure of booming is the change of the vehicle structure. Modifications can be applied either to the powertrain or the body panels.

On the powertrain side, the most common point of interest is the cardan shaft in a case of rear wheel drive (RWD) or driveshafts in a case of front wheel drive (FWD). In general, the changes are focused on the shaft diameter, length and shape. Therefore, the shaft mass, stiffness and hence the natural frequency is optimized in order to avoid the collision with booming noise frequency. Also the shaft torsional damping plays an important role but the magnitude is always dependent on the selected material. The other optimization can be done in the transfer path through the powertrain mounts. Also the powertrain subframe optimization may contribute to the booming noise reduction. [23]

The second possible modification is focused on the vehicle cabin. CAE tools are usually used to analyse the modal shapes of vibrations. A 3-D model of the cabin is mostly meshed into a structural and acoustic grid as it can be seen in figure 24. The compartment parts (doors, roof, floor, windshield, etc.) are subjected to an analysis in order to determine the contribution to the interior boom and to give a base for improvement proposals. [24]



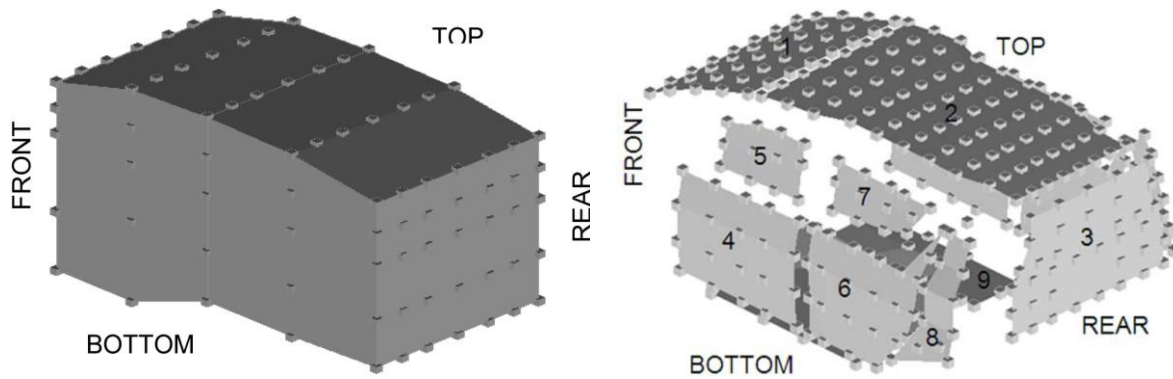


Figure 24 Acoustic and structural meshed models of the cabin [24]

### Passive noise control

This strategy is based on the application of the sound absorbing materials or isolating material for the source of noise. It is a relatively simple countermeasure, but it brings out an increase in the vehicle cost and weight and a poorer fuel efficiency as a result. [24]

### Active noise control

The booming noise can be also avoided by using active components added to the transfer path. One option is the in-cabin noise reduction by sensing the noise by a reference sensor. The noise signal is compared with a signal from an error microphone, processed by an algorithm and filter, and the anti-noise signal with opposite amplitude is emitted by a speaker so it cancels out the original noise as it can be observed in figure 25. There is a wide spectrum of methods and controlling algorithms for the active noise cancelation. This approach requires expensive additional devices (microphones, speakers), therefore it is mostly used in luxurious vehicles. [24, 25]

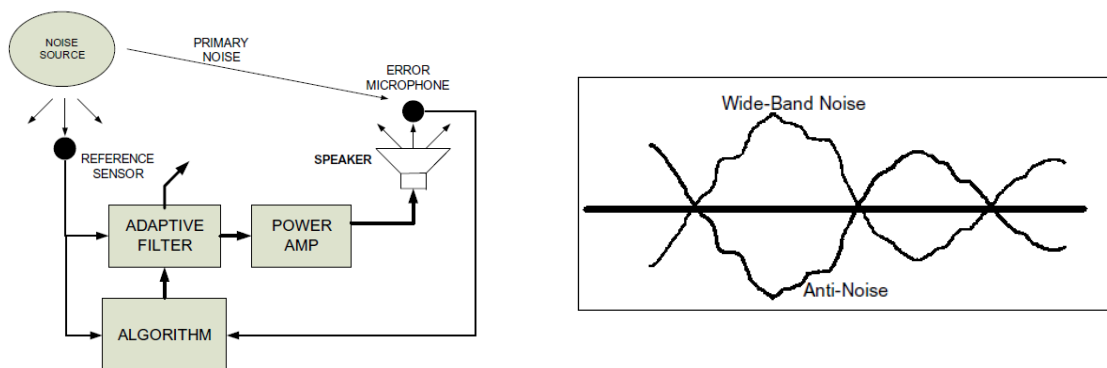


Figure 25 Principle of in-cabin active noise control [24]

The next method of active noise control is powertrain-based. It is applicable for a parallel hybrid vehicle with a configuration called Transmission Mounted Electric Device (TMED) but possibly for a power-split hybrid, too. TMED has two motors, one as Hybrid Starter Generator (HSG) connected to the crankshaft by the accessory belt and the second, propulsion motor, mounted on the output shaft of the

flywheel as shown in figure 26. No torque converter, which can suppress the oscillations, is used in order to minimize the mechanical losses.

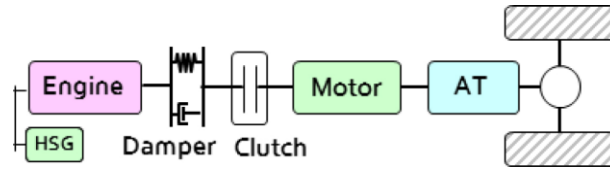


Figure 26 TMED parallel hybrid configuration [25]

The engine torque fluctuations caused by the engine are transmitted through the driveline. Their phase is sensed, and the anti-phase vibration torque is produced by the propulsion motor, so the engine fluctuations are suppressed as you can be seen in figure 27. The phase is estimated based on the frequency response and the feed-forward anti-phase torque control method. [25]

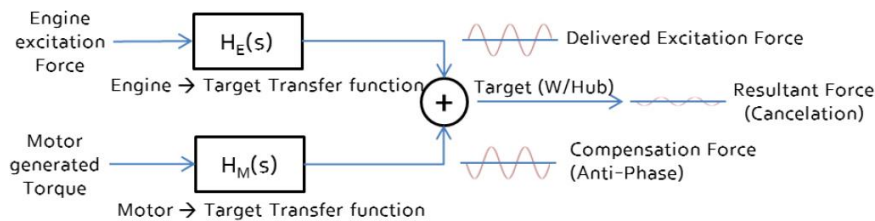


Figure 27 Main principle of anti-phase torque reduction in drivetrain [25]

### Modification of operational point of the source

As mentioned before, the Toyota Hybrid System (THS) is a highly variable system. e-CVT transmission allows to operate the combustion engine in an arbitrary regime of the vehicle speed. The engine is operated primarily in the area (line) with the highest efficiency, e.g. with the lowest fuel consumption. Nevertheless, this area can collide with the area where the booming noise occurs. It usually happens in the low engine speed with a high engine load. The peak combustion pressure is high, and the duration of the combustion is relatively long due to the low engine speed. It gives a nature for the strongest torque oscillations propagating through the drivetrain and later transferred to audible noise.

Thanks to THS variability, the operational point of the engine can be modified by controls – the master Hybrid Vehicle Electronic Control Unit (HV-ECU) – in order to decrease the booming noise. It can be shifted from the base operating point with the highest efficiency (A-1) to a new operating point (A-2). The engine power output is kept the same (moving on the iso-power line). The engine speed  $N_e$  is increased ( $\Delta N_e$ ) by MG1 speed variation. The engine torque  $T_e$  decreases ( $\Delta T_e$ ) as well as its fluctuations. As a result, the noise level decreases, too. The acceptable noise limit can be expressed as a NV line in the engine performance characteristic as can be seen in figure 28. The operational point (A-2) will be always located on this line. The acceptable noise limit, which can be expressed as an NV line in the engine performance characteristic, is set by calibration engineers based on testing and subjective evaluation or objective measurement (i.e. driveshaft torque oscillations).

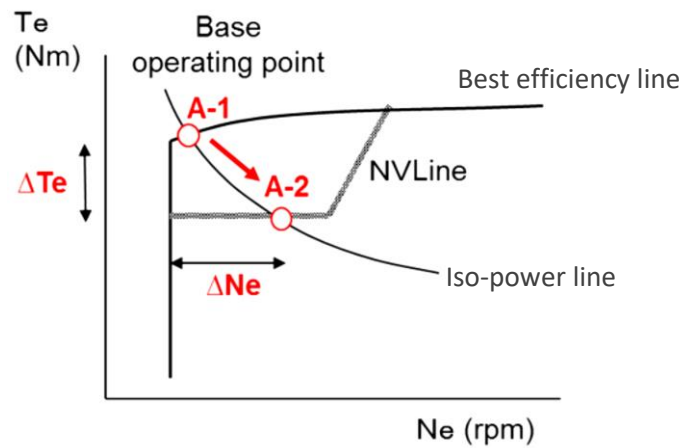


Figure 28 Engine operational point modification

This control method requires a proper calibration process in the final stage of the vehicle development phase but doesn't bring any additional mass and production costs. However, the fuel efficiency is sacrificed. The final NV line is always a trade-off between the low fuel consumption and the acceptable level of the booming noise.

This method of the booming noise reduction is the main principle used in THS and is the precondition of this work. The tendency is to move the calibration process made by a human using the prototype test vehicle to the model-based calibration (MBC) approach. For this purpose, a simulation model for the booming noise prediction must be developed.

## 4. Toolchain development

As it has been already mentioned, computer technology helps us to achieve a higher productivity and decrease the time throughout the designing process. During the last thirty years, virtual modelling has become inseparable part of engineering and its importance steadily grows. Besides the all-purpose engineering programs, there are many software products which try to meet the specific demands of the automotive, off-highway vehicles, railway and aircraft industries. Nowadays, a wide range of them can cover almost every aspect and phenomena which occurs in the transportation applications, including 3-D designing of parts, vehicle dynamics, strength analysis of parts or computational fluid dynamics, etc. Since having this wide range of products, it is always necessary to select an appropriate program for the task.

For many applications it can be easier and, in some cases, even necessary to couple more programs into a toolchain to correctly simulate phenomena. Also, in this case of NV booming assessment, a development of a toolchain is the most suitable approach. In order to well predict the dynamic behaviour of the hybrid powertrain, two models in two different software environments were identified as suitable. In particular, the first, HEV control model, was created in MATLAB Simulink, and the second, powertrain model, in LMS Amesim.

LMS Amesim (Advanced Modelling Environment for Performing Simulations) is a commercial simulation software of multi-domain systems for engineering. It is focused on automotive and aerospace industries. The software provides an effective 0-D/1-D simulation tool to model and analyse multi-body domains and predict their performance. For easy modelling, LMS Amesim provides a wide range of libraries (mechanical, electrical, thermal, electro-mechanical, logical, hydraulic, pneumatic or powertrain), containing pre-defined components. For instance, the mechanical library contains elements like springs and dampers, inertias, gear ratios or friction elements for translational and rotational movement. The powertrain library includes more sophisticated components for driveline as clutches, planetary gear sets, differential and joints. Besides these, it also provides engine case and powertrain mounts blocks for prediction of the powertrain block movement. This is one of few 3D models in LMS Amesim.

MATLAB with Simulink environment is a very versatile program and can be paired with many other programs. The library contains many elements for instance for logical and math operations and signal processing.

From now, the MATLAB Simulink model will be referred to as a SiL model (Software in Loop) and LMS Amesim model as a powertrain model.

## 4.1. Software in Loop

This work starts with an already existing model created in MATLAB Simulink. SiL model can simulate various driving cycles. It can predict general vehicle behaviour, torque, speed and power distribution among plants. The model consists of three part: driver's model, control model and vehicle model as depicted in figure 29. It is specifically prepared for Toyota CH-R in the European hybrid specification with 1.8L VVTi engine and NiMH battery.

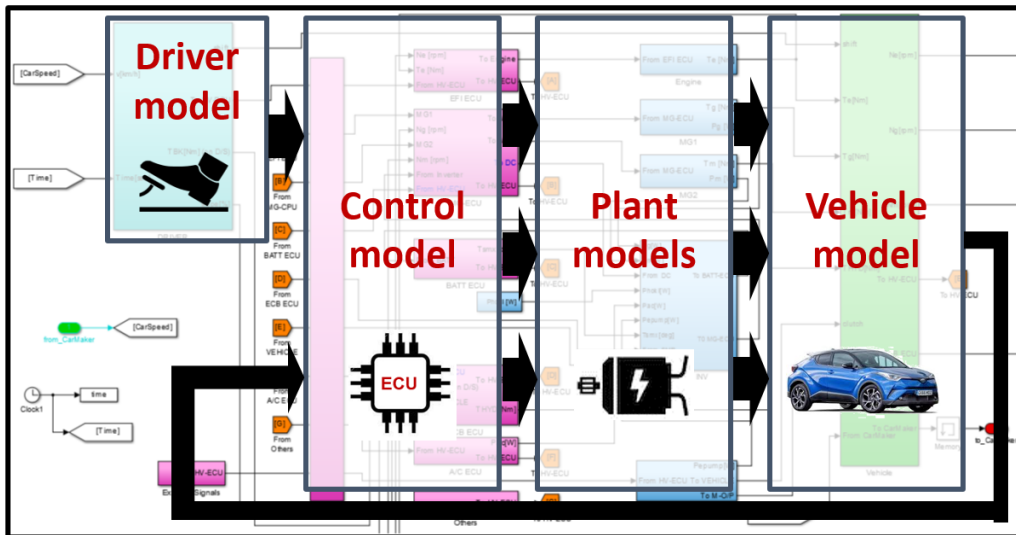


Figure 29 Simplified SiL model scheme

### 4.1.1. Driver model

The driver model translates the driving condition inputs to the commands for the control model in two modes. One, following either accelerator and brake pedals positions, and the second which follows the target speed and regulates the position of the accelerator and brake pedals by a PID controller. It also contains the boundary conditions of an experiment as temperatures of parts, ambient pressure or road conditions.

### 4.1.2. Control model

The control logic is the heart of the model. It consists of electronic control unit models (ECU). Like in the real vehicle, the software includes all the control functions of the vehicle or corresponding vehicle parts. In a conventional vehicle it governs the main control functions referring to the engine, such as E/G start and stop system, exhaust gas recirculation rate (EGR) or variable valve timing (VVT). For hybrid vehicles, the control unit must be capable to process the commands for various sources of power (engine, electric motors).

In the Toyota Hybrid System, we recognize the master ECU called the Hybrid Vehicle Electronic Control Unit (HV-ECU), which is in charge of total system control. It makes decisions which are communicated to the sub-system ECUs. Namely these are the Engine ECU (EFI-ECU), Motors ECU

(MG1 and MG2 ECU) Battery ECU (BAT-ECU). It also masters the ECUs not directly related to vehicle propulsion system but influencing the plants either in the way of vehicle dynamics as brake system (ECB-ECU) or auxiliary power consuming system as air-conditioning (A/C-ECU).

Inside the Simulink model, the ECU models contain the control logic in the form of S-functions, which is a computer language description of the original C-code compatible with MATLAB Simulink environment, in MEX files. The S-function block in Simulink environment only refers to the MEX file but the function itself is inaccessible. Hence every time any structural change in the vehicle model in Simulink is needed, the C-code must be edited and recompiled again. [26]

### **4.1.3. Plant and vehicle models**

Plants and vehicle models provide the response to the outputs from the control logic in order to simulate a real car behaviour in the longitudinal direction. All the impact in the lateral and vertical directions are neglected. The plant models controlled by ECUs such as the combustion engine, MG1, MG2, battery, converter and inverter models and the brake and air-conditioning are simplified or map-based.

These plants provide output to the vehicle model such as engine torque  $T_e$ , MG1 torque  $T_g$ , MG2 torque  $T_m$  and braking torque. The vehicle model contains the road load calculation based on physical parameters (ambient temperature and pressure, road properties, vehicle mass), car model, calculating the vehicle speed and a powertrain model of the hybrid vehicle. The powertrain provides the speed response of the system, more specifically engine speed  $N_e$ , MG1 speed  $N_g$ , MG2  $N_m$ , and torque response of countershaft  $T_o$ .

Prediction of the driveline dynamics of this vehicle model is not possible because it does not contain any properties of the shafts such as stiffness or damping coefficient which are essential for NVH prediction. One way would be a completely new vehicle model in Simulink which includes all this information. But since there was an existing standalone powertrain model of this vehicle, it has been decided to replace the simple powertrain model with it. The sampling frequency of SiL model is 400 Hz, time step 0.025 s, respectively.

### **4.2. Initial powertrain model**

As mentioned above, the powertrain model was already existing. It was extended by powertrain block and powertrain mounts models in the previous work. You can find the scheme in the following figure 30. [27]

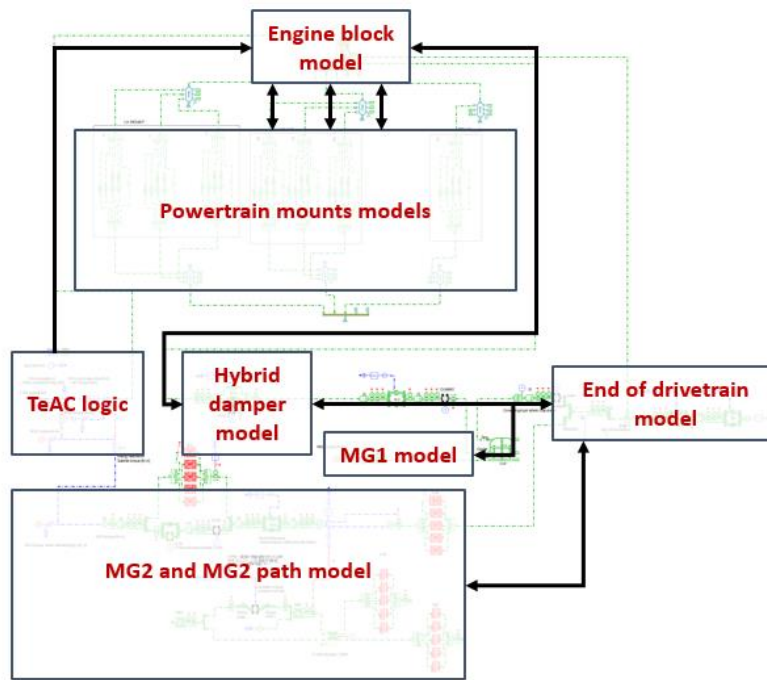


Figure 30 Simplified powertrain model scheme

LMS Amesim powertrain model is fully dynamic and includes the properties of shafts and other components such as stiffness, damping rates needed for the dynamic simulation. On the other hand, it does not include any control logic for a hybrid vehicle plants such as engine, MG1 and MG2. Creating the control logic in LMS Amesim would be very demanding, most likely unfeasible.

The powertrain model is mostly based on mechanical, powertrain and logical libraries. As a standalone model, it has never been validated for booming noise assessment. It contains models of powertrain parts with different level of their complexity. The response of the model is calculated based on inputs into the model in terms of torques signals ( $T_e$ ,  $T_g$ ,  $T_m$ ) and two speed signals (wheel speed  $N_w$  and  $N_e$ ).

#### 4.2.1. Amesim model components

##### TeAC logic

For a prediction of booming noise, it is necessary to ensure an appropriate dynamic input from the engine block. The fluctuating engine torque is an expression of torque from combustion which acts on the crankshaft. It is calculated externally by so called TeAC logic depicted in figure 31. Engine speed  $N_e$  and the value of non-oscillating engine torque  $T_{eDC}$  enter the TeAC map, which determines the magnitude of torque oscillations (TeAC level). Engine speed is also integrated and normalized to a sine wave (AC signal) with corresponding combustion frequency (amplitude equal to one). Then, the gain of TeAC level to the AC signal makes the oscillating engine torque ( $T_{eAC}$ ). In the end,  $T_{eAC}$  is summed up with the mean value of engine torque  $T_{eDC}$  and create the final engine torque signal  $T_e$  as in figure 32.

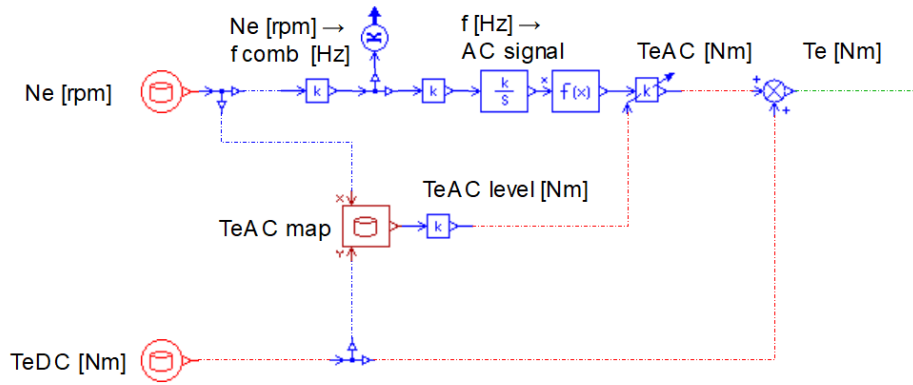


Figure 31 TeAC logic scheme

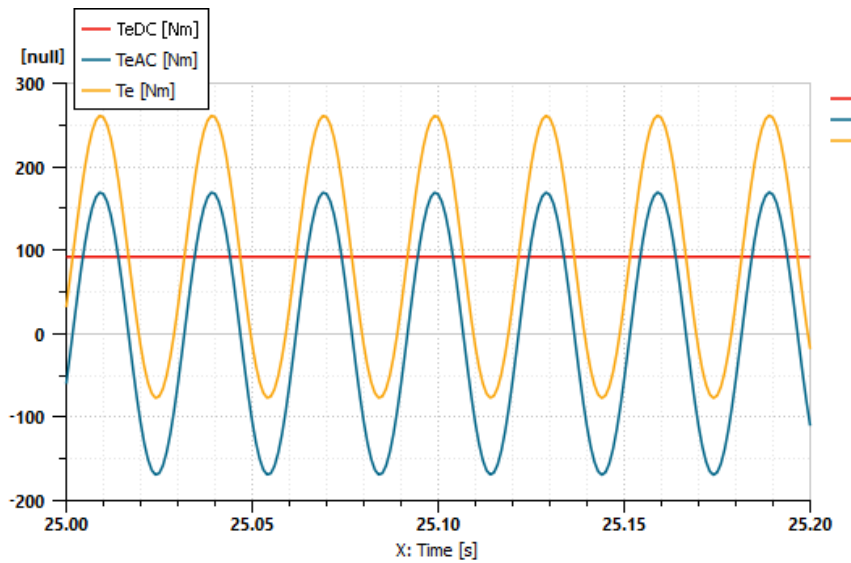


Figure 32 Engine torque signal composition in powertrain model

### Engine block model

This engine torque signal enters the engine block model. The engine block has six degrees of freedom and covers the information of crankshaft, flywheel and engine side of the Hybrid Vehicle damper (HV damper) moments of inertia; further the moments of inertia of the engine block and its initial state (position and speed) in all directions ( $x, y, z, \theta_1, \theta_2, \theta_3$ ). It also receives the torque response from the differential output and force response from powertrain mount models. Based on Newton-Euler equations it calculates the flywheel rotary velocity and engine block movement.

### Powertrain mounts models

As mentioned above, the engine block is connected to the powertrain mount models. Their topology and parameters were identified in the previous work. The left and right mounts are decomposed into  $x, y$  and  $z$  directions. The torque rod mount model includes only  $x$  direction properties. Besides a spring and damper, each model is extended by two Maxwell cells and a Mats-Berg friction unit. A scheme of the right-hand mount is shown in figure 33. [27, 28]



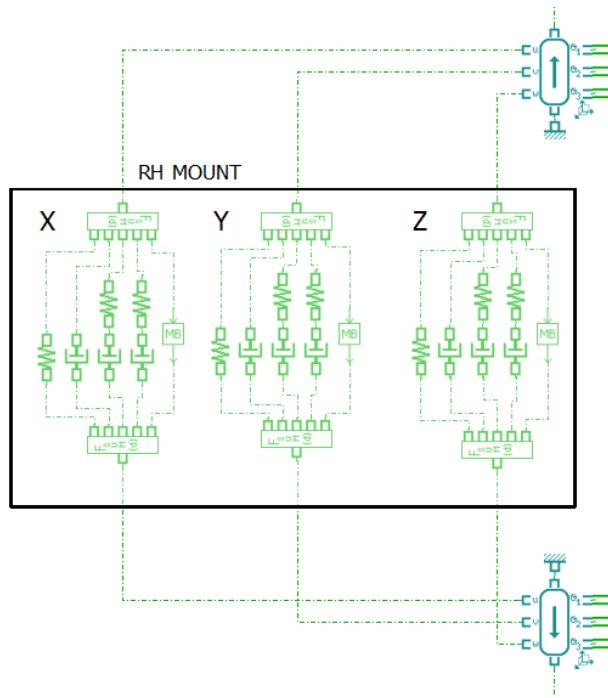


Figure 33 Right-hand powertrain mount model scheme

### Hybrid Vehicle (HV) damper model

Engine block is also connected to the HV damper model. It comprises of rotational spring, damper and a friction element (hysteresis) as shown in figure 34. It makes the torque response to the flywheel rotary velocity coming from the engine block. The value of damping  $c_{HV}$  is calculated like all the shaft damping rates in the powertrain model.

$$c_{HV} = \frac{a_{HV} \cdot k_{HV}}{2\pi \cdot f_{comb}} [Nm \cdot rad^{-1} \cdot s, Nm \cdot rad^{-1}, Hz] \quad (5)$$

where  $a_{HV}$  is a damping constant of hybrid damper,  $k_{HV}$  stiffness of the HV damper and  $f_{comb}$  is the combustion frequency.

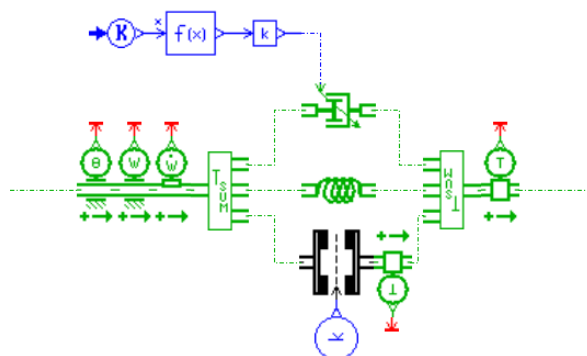


Figure 34 HV damper model scheme

## MG1 model

MG1 model is significantly simplified as an inertia block with MG1 torque input as shown in figure 35. Its torque output comes together with the output from HV damper to the power-split unit which is a simple model of a planetary gear set without friction.

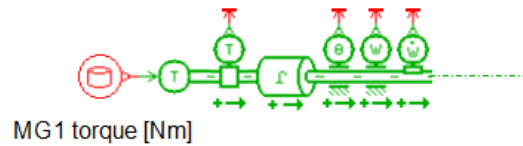


Figure 35 MG1 model scheme

## MG2 and MG2 path model

Despite the MG1 model, MG2 and its path model is very complex and includes models of radial and axial backlashes to simulate rattle and other mechanical contact related noises. They activate in transient around  $T_m = 0$  Nm when MG2 changes its mode from motoric to generator or vice versa. The conditions of booming noise are mostly in steady state, and the value of  $T_m$  should be always kept in range when this phenomenon does not occur. In the following figure 36, the black boxes cover the backlash models according to Toyota Motor Europe's confidentiality guidelines.

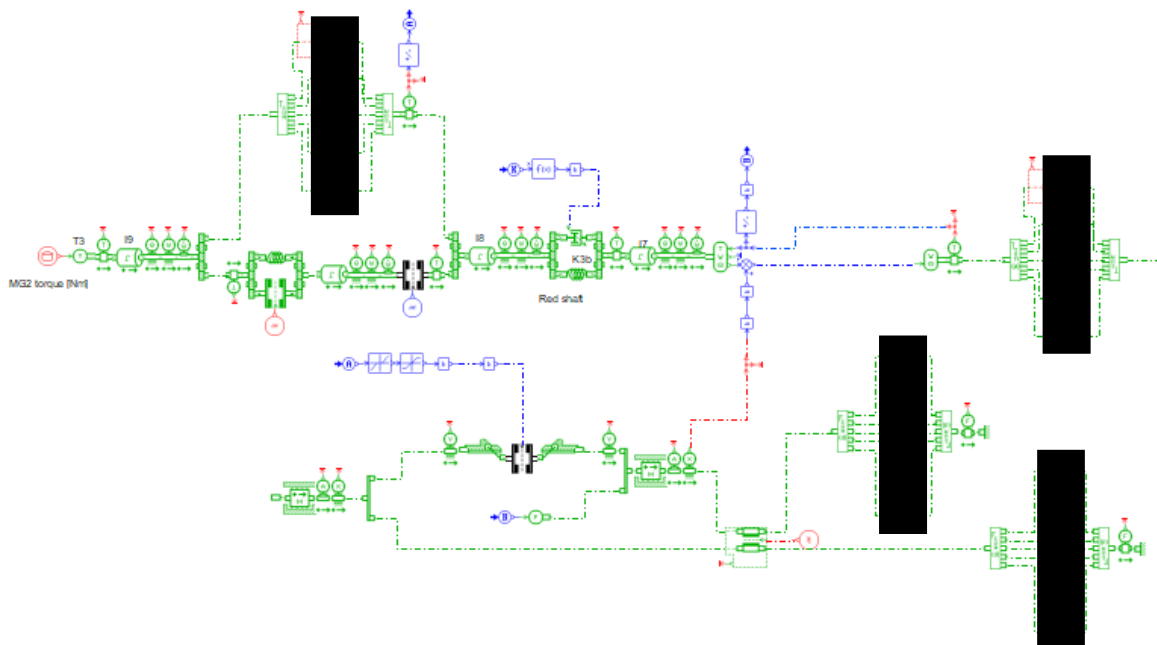


Figure 36 MG2 and MG2 path model scheme

## End of drivetrain

The end of drivetrain is also simplified. The scheme can be seen in figure 37. The countershaft is not modelled as a single shaft; its inertia is lumped together with the differential and a half of equivalent driveshaft inertia. The second half of driveshafts inertia is lumped together with tire. This model neglects the laterality of the left and right side after the differential model. The properties of left and

right driveshafts and wheels are always lumped into a single model. Because of the different properties of left and right driveshafts, their equivalent stiffness  $k_{DS\ eq}$  must be determined. Similarly, as mentioned above for HV damper, the damping coefficient  $c_{DS\ eq}$  of the lumped driveshaft model is calculated from the combustion frequency. The same principle was applied to the tire model.

$$k_{DS\ eq} = \frac{4 \cdot k_{DS\ LH} \cdot k_{DS\ RH}}{k_{DS\ LH} + k_{DS\ RH}} \quad [Nm \cdot rad^{-1}] \quad (6)$$

In case  $k_{DS\ LH} \cong k_{DS\ RH}$ :

$$k_{DS\ eq} = k_{DS\ LH} + k_{DS\ RH} \quad [Nm \cdot rad^{-1}] \quad (7)$$

$$c_{DS\ eq} = \frac{a_{DS} \cdot k_{DS\ eq}}{2\pi \cdot f_{comb}} \quad [Nm \cdot rad^{-1} \cdot s, Nm \cdot rad^{-1}, Hz] \quad (8)$$

where  $k_{DS\ LH}$  and  $k_{DS\ RH}$  is the stiffness of left and right driveshaft,  $a_{DS}$  is the coefficient for driveshaft damping and  $f_{comb}$  is the combustion frequency.

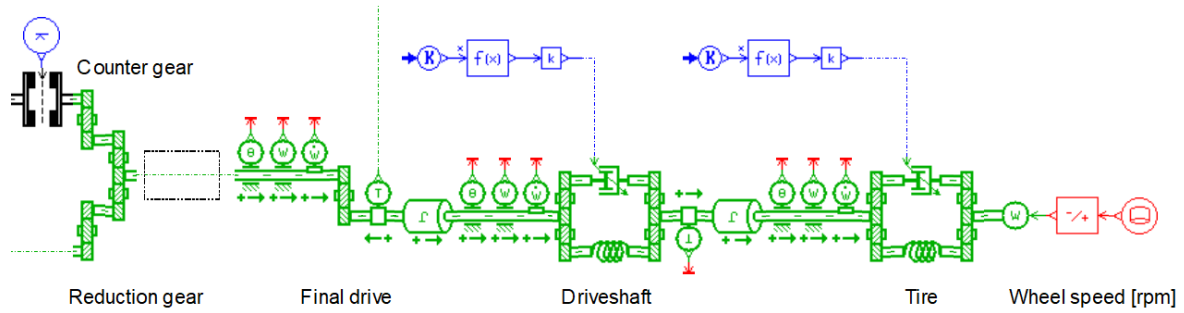
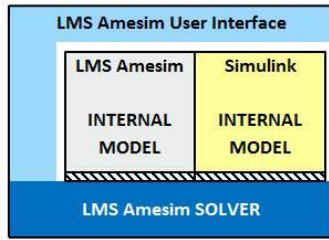


Figure 37 End of drivetrain model scheme

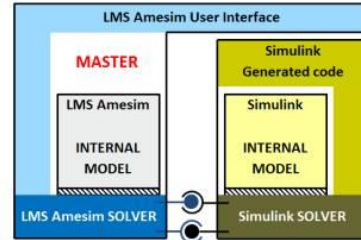
### 4.3. Coupling into the toolchain

As has been described in previous chapters, the current SiL model is not capable of dynamic simulation but it contains the full control logic of a hybrid vehicle (simplified in some sub-levels). On the other hand, LMS Amesim powertrain model should be capable of predictions of the dynamics but does not include any controls. Therefore, a co-simulation of these two models is believed to take the advantages of both and create a stable model toolchain which can be used for booming noise prediction and in an earlier stage of its calibration.

As mentioned before, MATLAB Simulink is a very versatile environment. Therefore, the abilities of LMS Amesim will be the object of interest in order to set the toolchain. It offers several options for a simulation together with MATLAB Simulink. They can be either model exchange based or co-simulation with different solver settings.



a) SL2AME co-simulation mode

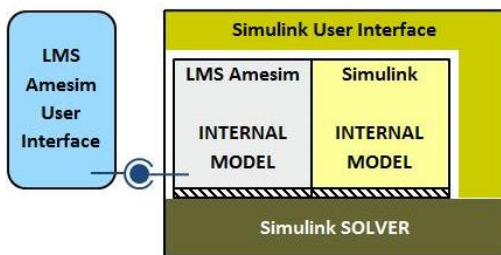


b) SL2AMECosim co-simulation mode

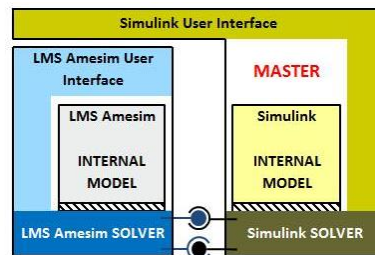
Figure 38 Co-simulation modes SL2AME and SL2AMECosim

The first mode (SL2AME) in figure 38 a) is a model exchange and exports the Simulink model into LMS Amesim. In this mode, only Amesim solver is used and MATLAB licence is not needed.

The second mode (SL2AMECosim) figure 38 b) couples both, Amesim and Simulink, into a co-simulation. Each of them uses its own solver and they only interchange signals. This mode is supported for MATLAB 2014b and greater and the Simulink time step is always fixed. In both previous cases, simulation is controlled from Amesim environment.



a) AME2SL co-simulation mode



b) AME2SLCosim co-simulation mode

Figure 39 Co-simulation modes AME2SL and AME2SLCosim

The third and fourth modes (AME2SL and AME2SLCosim) in figure 39 a) and b) export the Amesim model into Simulink as a S-function. Both modes are controlled from MATLAB/Simulink environment. The third mode uses only MATLAB solver while the co-simulation mode employs solvers in each software separately.

The fourth option (AME2SLCosim) was chosen from several reasons. The SiL model must be always initialized by its Graphical User Interface (GUI) which is untransferable into Amesim co-simulation block. Amesim global parameters are changed more easily from Simulink environment. This mode also takes the advantage of using two different solvers. The settings of Amesim solver will be controlled from the Amesim co-simulation block in SiL.

Due to the LMS Amesim recommendation, the simulation frequency of LMS Amesim model should be at least ten times higher than the expected range of subjected oscillations. For the booming noise with the frequency range between 33 to 50 Hz, the frequency was set to 1000 Hz, time step 0.001 s, respectively.

### 4.3.1. SiL modifications

Initial SiL model of HEV vehicle in this work had vehicle and powertrain model modelled as S-function. This approach was not practical for the aim of this work. Therefore, several modifications had to be made. At first, a replacement of the vehicle black box model for white box model from another SiL was done. It was already mentioned that the vehicle model consists of three sub-models: vehicle resistance model, car model and powertrain model. Now the changes will be shown and described.

The newly implemented vehicle resistance block shown in figure 40 includes the road load calculation in two ways. The first one uses the real parameters of vehicle and road.

$$R = R_a + R_r + R_d + R_g [N] \quad (9)$$

where	$R$	- Total resistance force	$[N]$
	$R_a$	- Air drag	$[N]$
	$R_r$	- Rolling resistance	$[N]$
	$R_d$	- Drawbar load	$[N]$
	$R_g$	- Grade resistance	$[N]$

The constitutive relations can be written as:

$$R_a = \frac{1}{2} \rho \cdot c_D \cdot A_v \cdot \frac{v^2}{2} \quad [N, kg \cdot m^{-3}, 1, m^2, m \cdot s^{-1}] \quad (10)$$

$$R_r = m_{car} \cdot g \cdot f_r \quad [N, kg, m \cdot s^{-2}, 1] \quad (11)$$

$$R_g = m_{car} \cdot g \cdot \sin(\alpha) \quad [N, kg, m \cdot s^{-2}, deg] \quad (12)$$

where  $\rho$  is air density,  $c_D$  is drag coefficient,  $A_v$  is frontal area of the vehicle and  $v$  is vehicle speed.  $m_{car}$  is vehicle mass,  $g$  is gravitational acceleration,  $f_r$  is rolling resistance coefficient and  $\alpha$  is inclination angle.

In our case, the drawbar force and grade resistance will be neglected since the validation process will be performed only on a flat road with no trailer.

For air drag, the pressure, temperature correction of the density is applied in the following form:

$$\rho = \rho_0 \cdot \frac{T}{T_0} \cdot \frac{p}{p_0} \quad [kg \cdot m^{-3}, K, Pa] \quad (13)$$

where  $\rho_0$  is air density,  $T_0$  is at temperature,  $p_0$  is pressure, all at 0 °C.  $T$  and  $p$  are ambient temperature and pressure.

The second way is the road load calculation (vehicle equation of motion) based on quadratic equation with constant linear and quadratic coefficient. In the model, there is a manual switch between these two modes.

$$R = A + B \cdot v + C \cdot v^2 \quad [N, N \cdot (m \cdot s^{-1})^{-1}, N \cdot (m \cdot s^{-1})^{-2}] \quad (14)$$

where  $A$  is absolute coefficient,  $B$  is linear coefficient and  $C$  is quadratic coefficient.

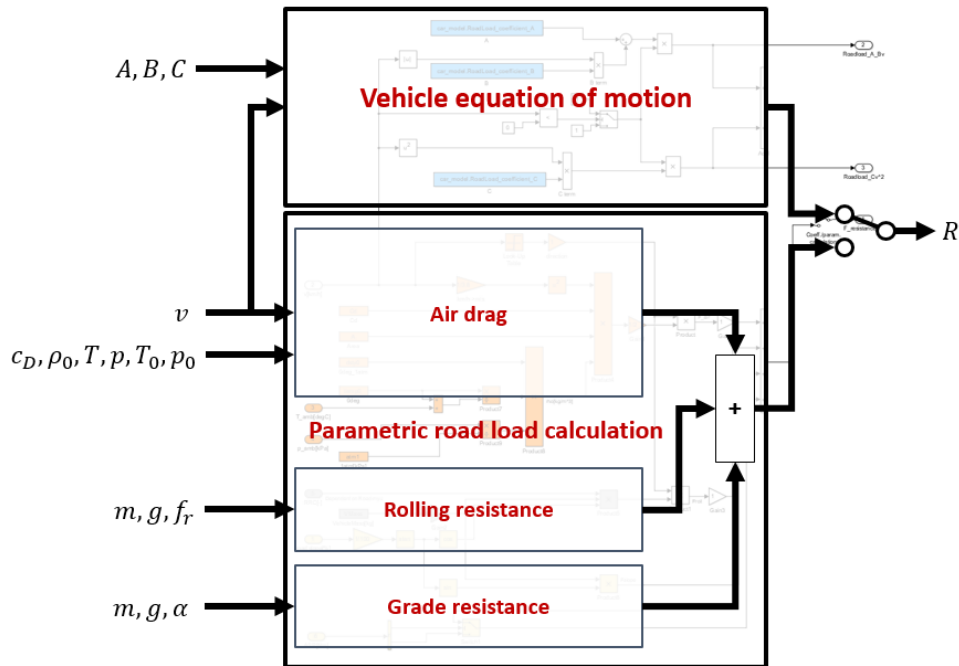


Figure 40 Vehicle resistance calculation block in SiL model

The car model is the next block which was implemented. The driving force as the output is summed up with road load force and vehicle speed is calculated. Equivalent mass  $m_{eq}$  is assumed as a sum of the vehicle weight plus the rotating inertia of rear wheels. Inertia of front wheels is included in the powertrain model.

$$v = \int \frac{F_{drive} + R}{m_{eq}} dt \quad [m \cdot s^{-1}, N, kg] \quad (15)$$

$$m_{eq} = m_{car} + \frac{I_{rw}}{r_t^2} \quad [kg, kg \cdot m^2, m] \quad (16)$$

where  $F_{drive}$  is driving force,  $R$  is total resistance force.  $m_{car}$  is vehicle mass during measurement,  $I_{rw}$  is moment of inertia and  $r_t$  is tire radius.

The powertrain plant model is the last part, which had to be adjusted. As been already said, this model does not include any structural properties of the shafts and gears as stiffness or damping coefficients, so it is not possible to predict the dynamic behaviour. Therefore, this model will be substituted by Amesim model.

### 4.3.2. Powertrain model modifications

In LMS Amesim powertrain model, only few modifications were made in order to setup toolchain. The interface block was added to the model and appropriate inputs and outputs were set and linked with the sensors and connectors. Every shaft had been already equipped with sensors for angular displacement, velocity and acceleration. The choice of torques as inputs which come from the plant models and speeds as outputs comes from the idea of speed response to the force impulse at a certain state of vehicle speed and follows the modelling convention.

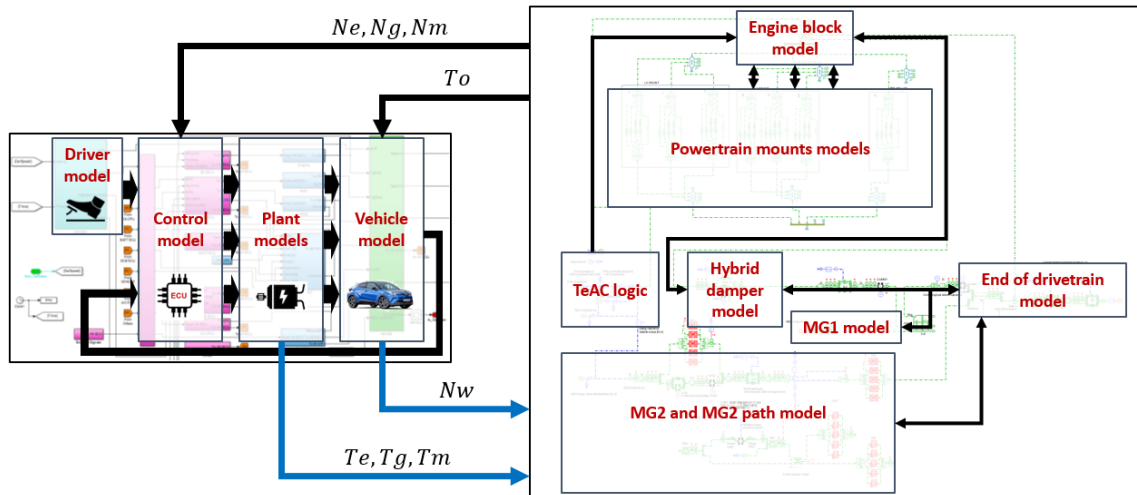


Figure 41 Scheme of co-simulation

### 4.4. Evaluation of developed toolchain

During the setting of co-simulation, the toolchain was tested, and results compared with the original SiL model with S-function vehicle model, which was validated before. Data from measurement were not available yet. Several virtual scenarios were chosen to verify the ability of the toolchain to simulate the desired commands. They were performed in both regimes, following the target speed or accelerator and brake position. The results showed that some limitations for model initialization exist.

For some scenarios some strong dynamics could be seen in high engine speeds. Despite that, in the middle range the dynamics were suppressed. The investigation showed that the TeAC map model was made only for a specific range of engine speed from 1000 to 2000 rpm. When increasing engine speed above 2000 rpm, it is linearly extrapolated and the level of TeAC amplitude crosses zero level and becomes negative, especially under low load. In high engine speeds, the oscillations are becoming huge again, with an opposite amplitude. The range of critical engine speed for booming is under 1500 rpm so this model should be valid for the purpose of this work. Using this TeAC logic for another purpose as driveability is not recommended.

The toolchain of two different environments was successfully set. At this moment, it is necessary to validate the model performance by a test vehicle in order to prove the correct prediction so that it can be used for the booming noise prediction in the future.

## 5. Toolchain validation

Once the toolchain had been created, the validation was needed to prove the abilities of the model. Although the booming noise prediction was mostly subjected, the co-simulation model must also satisfy the requirements of a specific level of the versatility and the correct prediction of different phenomena which are crucial for its overall functionality. A real test vehicle was used for this validation. The procedure was proposed first, data were measured and post-processed to be comparable with the data from simulation. Results were evaluated then. Some necessary improvements in the model had to be done already during the validation process. The validation process was divided into these five steps:

- Road load measurement
- Top-level validation
- Low frequency validation
- Powertrain block movement validation
- High frequency validation

At first, the real road load was measured with the test vehicle so it could be used as an input of the co-simulation model for the other steps. As the next step, the top-level validation was performed. In this part, the road load was verified and the ability of the model to replicate simple driving scenarios and predict values of torque and speeds of parts of the THS was proven. Then, the low frequency validation took part to find out if the dynamics below 33 Hz can be followed by the model. The last stage, the validation in higher frequencies (33 – 50 Hz) was done as the key one for the booming noise prediction. All the measurements were performed on the Toyota test circuit in Zaventem, Belgium.

### 5.1. Vehicle instrumentation

For the experimental data measurement activity, a real test vehicle, Toyota CH-R in the hybrid version with 1.8L VVT engine and NiMH battery, was used. It was necessary to equip the vehicle with sensors and open ECUs.

#### Open ECUs

The open ECUs were installed into the vehicle and replaced the production ECUs. A computer with a dedicated software developed for Toyota was connected. It which enables the communication with the ECU module and save the signals. Thanks to this software, the external commands could be written into the control logic memory. It allowed a change of values of some signal. The calibration maps could be adjusted or completely disabled, the load of the combustion engine could be increased by an additional battery charging request or purely electric mode was activated. The data sampling frequency of the open ECU was 200 Hz.



## Driveshaft torque sensors

Several sensors were instrumented to the vehicle. The most important ones were the driveshaft torque sensors, for both, left- and right-hand side. They were located in the middle of the driveshafts. Before the installation to the vehicle, they were calibrated on a dedicated torsional test bench depicted in figure 42. They allow to sense very small torque fluctuations at high sampling frequency of 10 000 Hz. This signal will be used mainly for the low and high frequency validation steps. The stiffness characteristics of each driveshaft were obtained as an additional information from the torsional bench test.

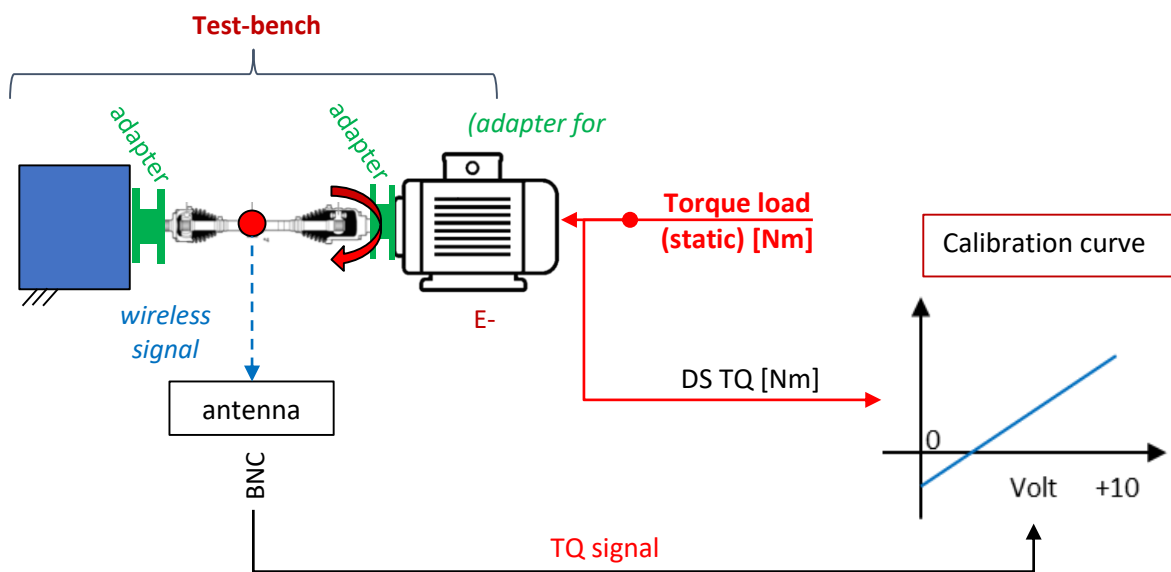


Figure 42 Driveshaft torque sensors calibration process

## Flywheel torque sensor

The test vehicle was also instrumented with a flywheel torque sensor. The location of the sensor and the measurement point can be seen in figure 43. This signal can be considered as the output torque from the crankshaft or input to the flywheel, before the smoothing effect of the high flywheel inertia. With the high sampling frequency of 10 000 Hz it was suitable for sensing the torque oscillations from the combustion. This signal will be used mainly for the high frequency validation in order to verify the force input into the drivetrain.

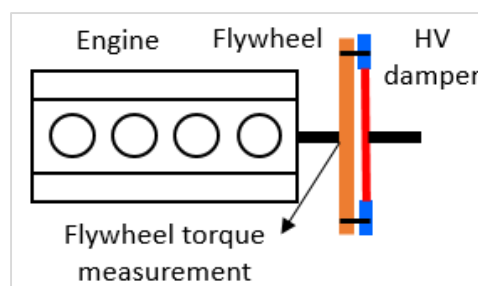


Figure 43 Flywheel torque measurement location

### Powertrain displacement sensors

The vehicle was also instrumented for the powertrain block movement measurement. There were three linear wire stroke sensors. Two of them were placed at the top of the engine, on the left- and right-hand side as you can see in figure 44. The sensor itself was fixed to the vehicle frame and the ends attached to the engine block. The third one was located close to the torque rod in the bottom of powertrain block as shown in figure 45. The sensor was fixed to the vehicle sub-frame and the end of the wire to the oil pan. The position of the wires was nearly horizontal for the standing-still condition. The sampling frequency was 10 000 Hz.

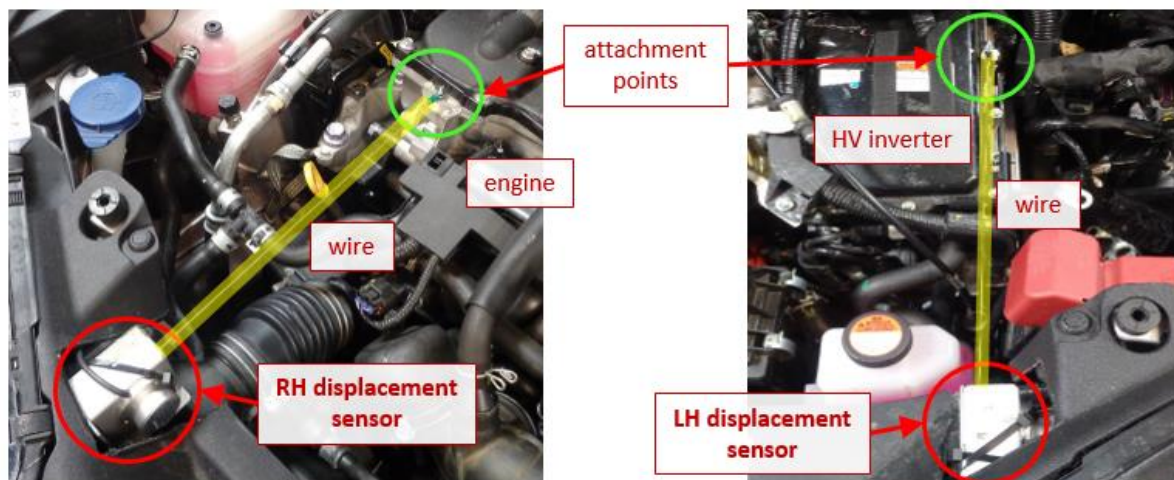


Figure 44 Powertrain top displacement sensors

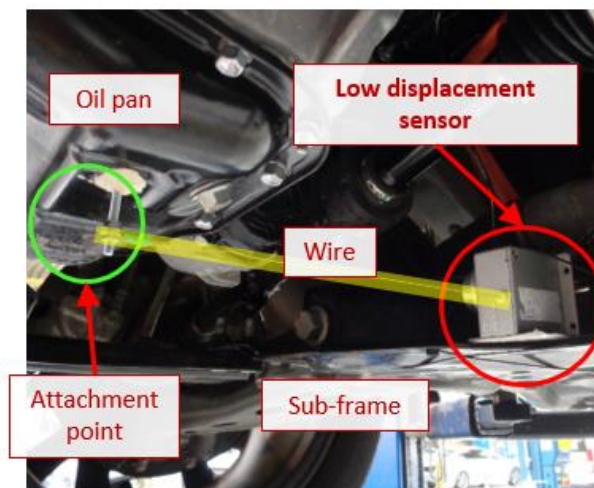


Figure 45 Powertrain low displacement sensor

### Differential ring gear speed sensor

For the vehicle speed measurement, an inductive speed sensor was installed to the differential gear wheel. This measurement was used for the road load determination.

Data from the sensors were processed in IMC data acquisition unit and stored in another PC with the IMC Studio software. This program set up the interface between the data acquisition unit and the user as well as controlled the experiment and the sensors settings.

## 5.2. Road load measurement

At first, the vehicle resistance had to be determined for the vehicle used in the experiment. The correct road load estimation is necessary as a proper input for the simulation. As has been already described in chapter 4.3.1, two ways of calculating road load in the toolchain can be used. One is based on the physical parameters as the vehicle weight  $m_{car}$  and frontal area  $A$ , ambient pressure  $p$  and temperature  $T$  in air density correction and estimated as rolling resistance coefficient  $f_R$  or drag coefficient  $c_D$  (9). The second is called the vehicle equation of motion (14).

The first one uses the physical and estimated parameters in a simplified way which do not necessarily fully correspond with reality. For example, the rolling resistance coefficient is usually speed dependent in reality, however this effect is neglected here. The second approach includes the linear constituent, which can represent the linearly dependent losses. They can be observed mostly in the mechanical parts of the powertrain (friction).

For toolchain purpose, the second approach was chosen. The reasons for this approach are at first the difficulty to estimate the real rolling resistance coefficient between the tire and the road surface. Secondly, the drag coefficient should be known from measurement in wind tunnel, but it can slightly differ for the test vehicle. In general, the vehicle equation of motion can fit the real road load curve dependent on the vehicle speed better thanks to the linear constituent. The coefficients of the equation can be obtained from a coast down test as a typical procedure.

The coast down consists in a launch from a certain speed, continuously recording the speed and the travelled distance until vehicle stops. The main aim of this test is to define the values of the resistant forces acting on the vehicle at certain speed and road conditions, in order to have the possibility to reproduce them in the simulation but also for the measuring of fuel consumption, emissions and noise pollution when using the chassis dyno test. [29]

In order to obtain the equation of motion of the vehicle, some simplifications must be adopted. The dynamic model was imagined based on the assumption that the motor vehicle consists of:

- mass  $m_{car}$  in translation motion;
- equivalent flywheel inertia  $I_{rw}$ , corresponding to the driven wheels (rear wheels);
- equivalent flywheel inertia  $I_{fw}$ , corresponding to the driving wheels and to all rotating parts kinematically connected to them.

The resistance force is calculated then as:

$$R = m_{eq} \frac{dv}{dt} [F, kg, m \cdot s^{-1}] \quad (17)$$

For the coast down test some conditions should be fulfilled. The road should be without inclination, ideally flat and its surface should be dry and smooth enough. The measurement should be performed only in the longitudinal direction, any steering input should be avoided. The constant tire dynamic radius  $R_t$  can be assumed for the vehicle wheels as well as very low tire ground slip. That means no energy loss will be generated by slip. [29]

For conventional vehicles, the engine should be unengaged from the driveline i.e. shifted to the neutral. For a hybrid vehicle with THS, the engine is never fully disengaged from the drivetrain. To keep it stopped, MG1 increases its speed when accelerating. Because the test is being performed from initial speeds over 100 km/h, the speed limit of MG1 would be reached. Therefore, the standardized process of road load measurement of a vehicle with the THS is set always with the engine on to avoid sudden changes (engine stop), which could have an impact on the dynamics and the losses in the powertrain. Some other conditions must be met, too. The coolant temperature should be higher than 80 °C, transmission oil temperature higher than 50 °C. The state of charge of the battery (SOC) should be in a required range. The road load was measured on the Toyota test track, whose length of the straight part is limited, therefore the test had to be divided into sections with different initial speed. Reasonable overlap of speed between trials had to be kept in order to avoid discontinuities in data. Every measurement of the same initial speed was repeated three times.

*Table 3 Conditions of measurement of road load*

	Unit	Value
Vehicle mass	kg	1703
Tire radius	m	0.329
Ambient temperature	°C	22
Ambient pressure	kPa	101.9

Data from the speed sensor of the differential ring gear, recalculated through the gear ratios and the dynamic rolling radius of the tire, were chosen for post-processing as the most precise ones in the measurement. They were evaluated by an internal Toyota process using MATLAB script. The script creates the best fitting curve of all measurement data with the least error. It gives two options: one gives the all three coefficients of the vehicle equation of motion ( $A$ ,  $B$ ,  $C$ ) and the second omits the linear  $B$  coefficient. Both variants were examined, and the probability distribution of each coefficient can be seen in figures 46 and 47.

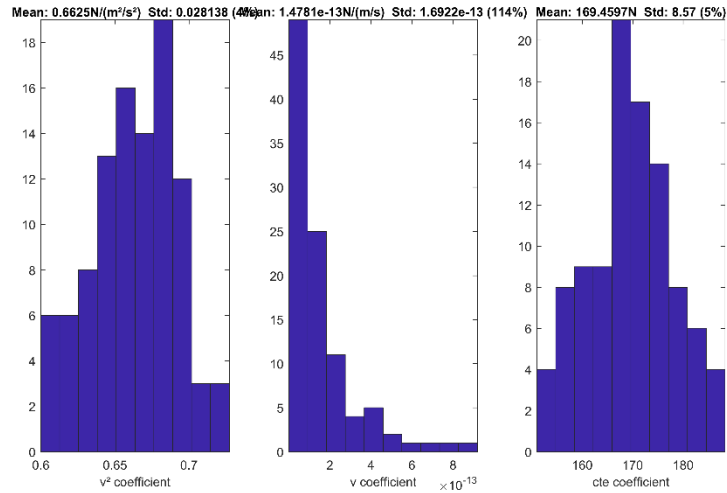


Figure 46 Vehicle equation of motion coefficients probability distribution of variant 1

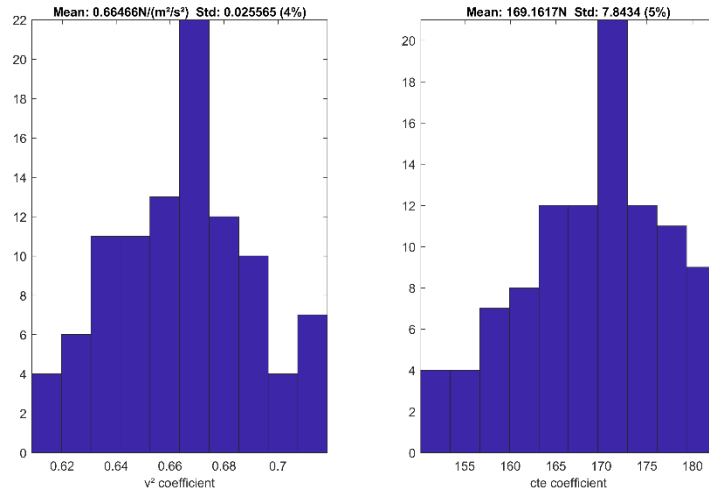


Figure 47 Vehicle equation of motion coefficients probability distribution of variant 2

The mean value of each coefficient, which is identical with the value with the highest probability, was chosen as a reference. The values can be observed in table 4. STD stands for the standard deviation.

Table 4 Vehicle equation of motion coefficients

Coefficient	Unit	Variant 1	STD [%]	Variant 2	STD [%]
<i>A</i>	N	169.5	5	169.2	5
<i>B</i>	N/(m/s)	$1.478 \cdot 10^{-13}$	114	-	-
<i>C</i>	N/(m <sup>2</sup> /s <sup>2</sup> )	0.6625	4	0.6647	4

For the first variant, the *B* coefficient is negligibly small and, on the top, the standard deviation is huge (114 %) so it is not trustworthy anymore. Therefore, not a big mistake is made when only *A* and *C* coefficients will be considered. Because the second variant was determined directly for these two coefficients, its values were applied and verified later in the simulation.

The road load measurement was performed with the weight of the vehicle including a driver, data acquisition system operator with a certain level of fuel in the tank. For other measurements, the weight could change because of a different driver or different amount of fuel in the tank. Therefore, the weight was measured before every experiment and road load must be adjusted for the simulation. The  $A$  coefficient closely corresponds with the rolling resistance calculation (18) where the gravitational acceleration and the rolling resistance coefficient can be considered as constants (the same test track). Then the new coefficient  $A_{new}$  would be due to different mass  $m_{new}$  in (19).

$$A \approx R_r = m \cdot g \cdot f_r [N, kg, m \cdot s^{-2}, 1] \quad (18)$$

$$\frac{A_{new}}{A_{RL}} = \frac{m_{new} \cdot g \cdot f_r}{m_{RL} \cdot g \cdot f_r} = \frac{m_{new}}{m_{RL}} \rightarrow A_{new} = \frac{m_{new}}{m_{RL}} \cdot A_{RL} \quad (19)$$

### 5.3. Top-level validation

When the road load was measured and the coefficients for the vehicle motion equation were determined, the first validation step could proceed. This validation should prove the ability of the toolchain to correctly predict various driving conditions. The model was examined for a correct estimation of power, torque and speed of parts (engine, MG1, MG2, propeller shaft) and other general variables of the system based on the same input of accelerator and brake pedal position.

At first, several basic driving scenarios were proposed considering diverse manoeuvres and modes. The measurement was performed with the vehicle on the test track, data were post-processed, the toolchain model was run with the same input and results were evaluated.

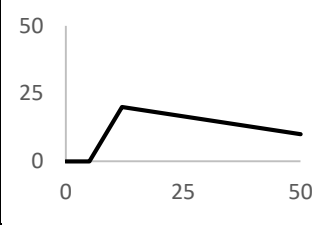
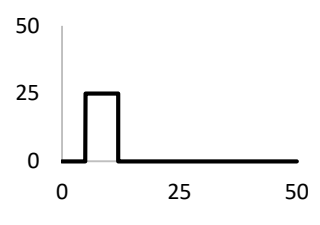
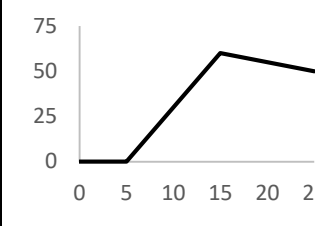
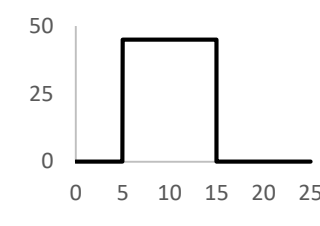
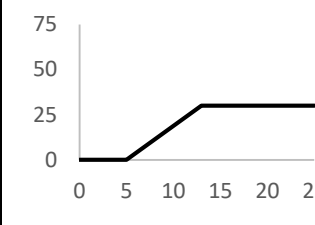
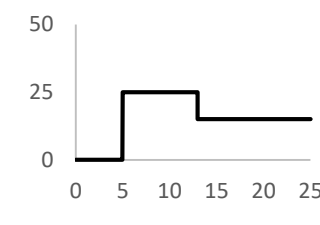
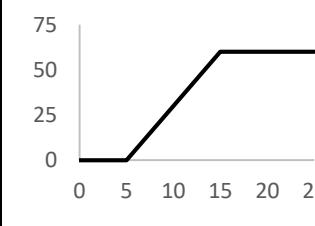
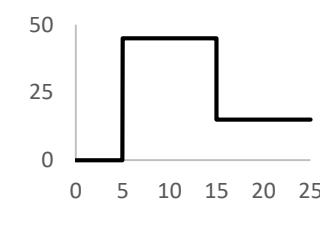
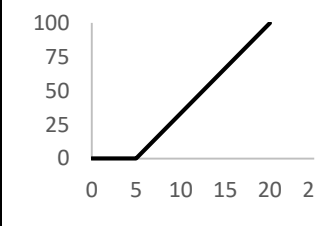
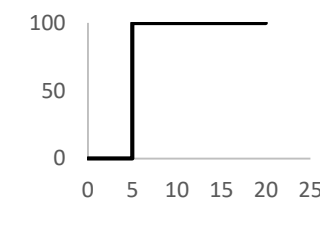
#### 5.3.1. Driving scenarios definition

At first, the driving scenarios must have been proposed to be followed during the measurement. They should cover various conditions including acceleration, steady speed driving or coasting. With a full hybrid vehicle, there is a possibility to perform a test in the hybrid electric vehicle (HEV) mode or electric vehicle (EV) mode.

Five scenarios were proposed, and the accelerator pedal and speed profiles can be seen in table 5. The first one, in purely electric mode, comprises of a mild acceleration to 20 km/h followed by a tip out and gradual coasting in a low speed. Thanks to the event without the running engine, the functionality of the electric part can be proven. The HV-ECU software was not edited to fix the EV mode, therefore the accelerator pedal position mustn't overcome 30 % of its range in order not to switch the engine on. The second scenario, now in the HEV mode, also consists of a mild acceleration to a higher speed than before and a tip out followed by a part of coast down in D-range from approximately 60 km/h. This gives a chance to see the reaction of the system to a sudden change of a command. It will be probably followed by a switching off the engine. The third scenario represents steady speed driving conditions at 30 km/h in EV mode. Potential difference in absolute values could be possibly observed as an

indication of the model inaccuracy. The fourth scenario is also in steady driving conditions with a difference of HEV and higher speed than the previous. The last, fifth scenario is a tip-in acceleration until high speed, which shows the response of the system under full load and might also show the limitations of the model.

Table 5 Driving scenarios proposals for the top-level validation

Case	Scenario	Speed profile [km/h]	Acc. pedal profile [%]	Mode
1	Low speed coast down in D range			EV mode
2	Medium speed coast down in D range			HEV mode
3	Steady low speed driving D range			EV mode
4	Steady medium speed driving in D range			HEV mode
5	Tip-in acceleration from stand still			HEV mode

### 5.3.2. Measurement

When the proposals were raised the measurement could proceed. Measurement of every scenario was repeated at least once to have a choice of case selection for later reproduction in the simulation. Scenarios were measured in three different days, case number 5 was repeated. The

temperature of coolant was always higher than 80 °C, transaxle oil temperature higher than 50 °C. Temperature of batteries was kept under a specified limit and SOC was kept in a given range. Following table 6 shows the conditions of each measurement.

Table 6 Conditions of the measurement of the top-level validation scenarios

	Unit	Case 1, 2	Case 3	Case 4	Case 5
Vehicle mass	kg	1693.7	1686.0	1687.4	1705
Ambient temperature	°C	20	21	20	18
Ambient pressure	kPa	102.1	101.1	101.2	101.8

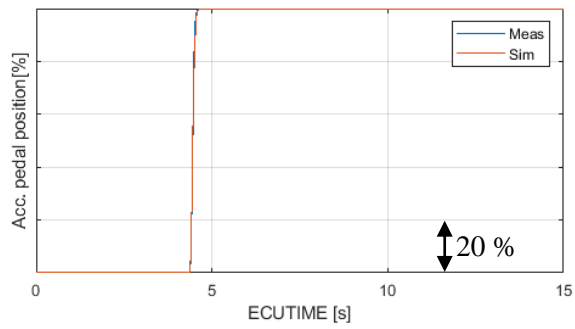
### 5.3.3. Evaluation

It was essential to set the methodology of the validation process first. Seven signals were chosen to be compared. Two of them can be considered as the key signals. The propeller shaft torque  $T_p$ , which is the first signal determined in the HV-ECU based on inputs, and propeller shaft speed  $N_p$ , which for simplicity in plots expressed as a vehicle speed  $v$ , as the output of the toolchain model and in a back-loop into the HV-ECU calculation. Next evaluated signals were engine torque  $T_e$  and speed  $N_e$ , MG1 torque  $T_g$  and speed  $N_g$  and MG2 torque  $T_m$ . MG2 speed is not shown because it is directly proportional to the vehicle speed  $v$  and hence the propeller shaft speed  $N_p$ . In an ideal case, the results of the toolchain should match absolutely with the results of experiment. This is usually not fully possible in the modelling praxis. The criteria of the success rate were not strictly set but reasonably small error should be achieved. For the propeller shaft torque  $T_p$  the error should not be more than 3 % or 5 Nm. For the vehicle speed  $v$  the maximum acceptable absolute error should not exceed 1 km/h. This applies to the steady or mild transient conditions. For the fully transient conditions, the timing of operations was evaluated. The other signals with lower priority should match well, too, but no criteria were set. During the evaluation process, the purpose of this model (the booming noise prediction) should be considered, therefore the impact of some phenomena not related to the booming noise can be neglected when the phenomenon is explainable.

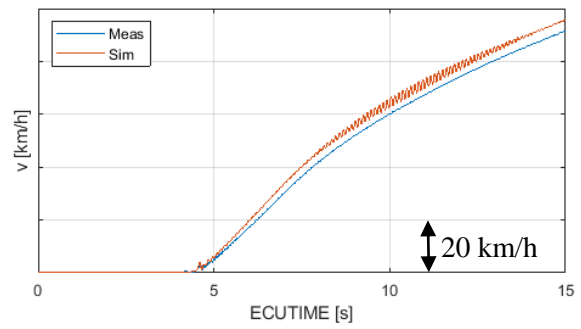
After the data post-processing, the same boundary conditions (accelerator pedal position, brake pedal position and initial SOC) were imposed to the toolchain model. The accelerator pedal position time series was simplified, the input table in SiL is able to process only a limited number of points. Because the accelerator pedal position signal is processed firstly in the HV-ECU, it had to be adjusted to fit precisely the corresponding signal from the measurement. All the scenarios were calculated then with the toolchain. Results of one case, case number 5 will be shown now in figure 48. The values of most of the plots are hidden according to Toyota Motor Europe’s confidentiality guidelines. The solid black line emphasises the zero line in  $T_g$  plot. It will be used in the same manner in other plots where needed.



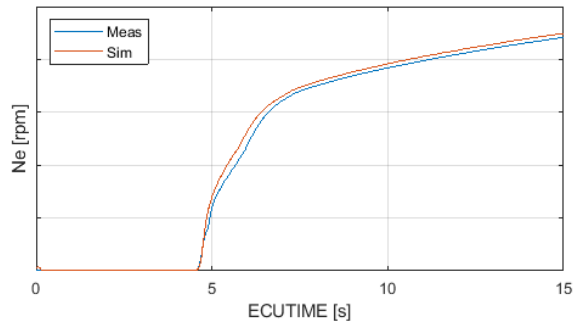
## Case 5



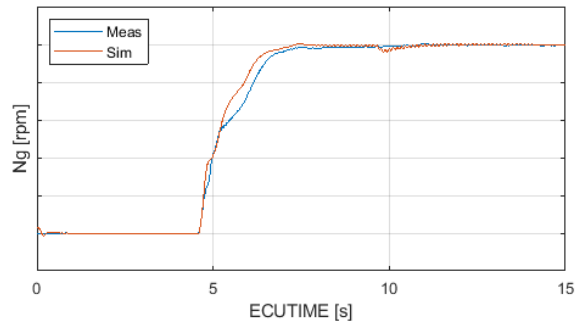
a) Accelerator pedal position [%]



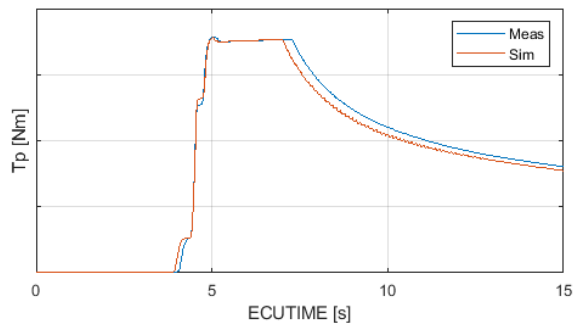
b) Vehicle speed  $v$  [km/h]



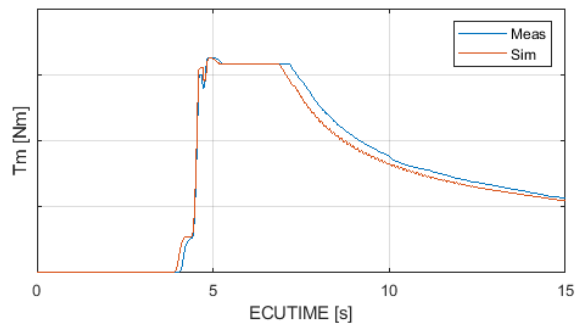
c) Engine speed  $N_e$  [rpm]



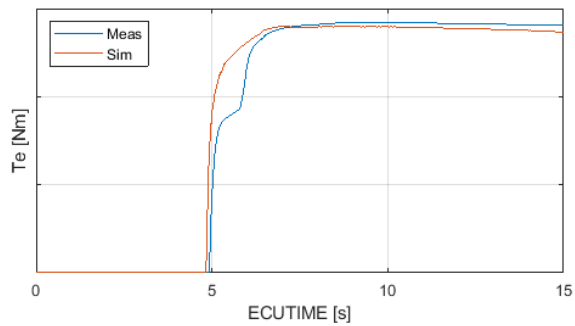
d) MG1 speed  $N_g$  [rpm]



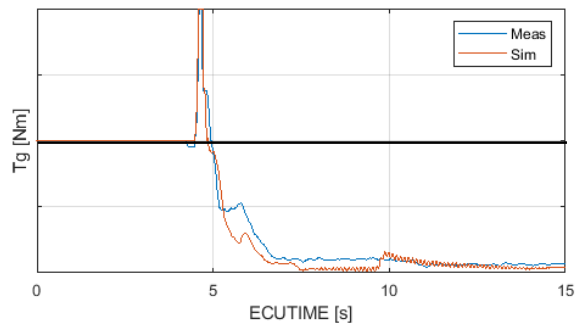
e) Propeller shaft torque  $T_p$  [Nm]



f) MG2 torque  $T_m$  [Nm]



g) Engine torque  $T_e$  [Nm]



h) MG1 torque  $T_g$  [Nm]

Figure 48 Initial results of the top-level validation of case 5

It can be seen in the plots, that results did not match well with the measurement data. The values differed from the data of experiment. The propeller shaft torque  $T_p$  in figure 48 a) prediction was too low, difference at  $t = 12\text{ s}$  was around 13 Nm. Difference of vehicle speed  $v$  in figure 48 b) was more than 4 km/h. Also in other scenarios the difference in propeller shaft torque and vehicle speed was too high to be acceptable.

The first idea how to fix this issue was to adjust the road load coefficients. As a result, one set of  $A$ ,  $B$  and  $C$  coefficients matching all the cases should be found. It meant to run many iterations. For this purpose, the intermediate version with the new vehicle model, without Amesim yet, was used. Its results were very close with the toolchain. The powertrain dynamics were not the subject yet. It helped to save time; the simulation time of the toolchain was roughly 30 times lower than SiL standalone model. It gave the idea of approximate values of road load coefficients for each case.  $B$  (linear) coefficient was also taken into consideration.

The analysis showed that  $A$  coefficients played the main role in lower speed and during acceleration, the  $C$  coefficient in higher speed and during coasting. The coefficients acted mostly against each other in terms of approaching the measurement data. It can be explained based on the following figure 49.

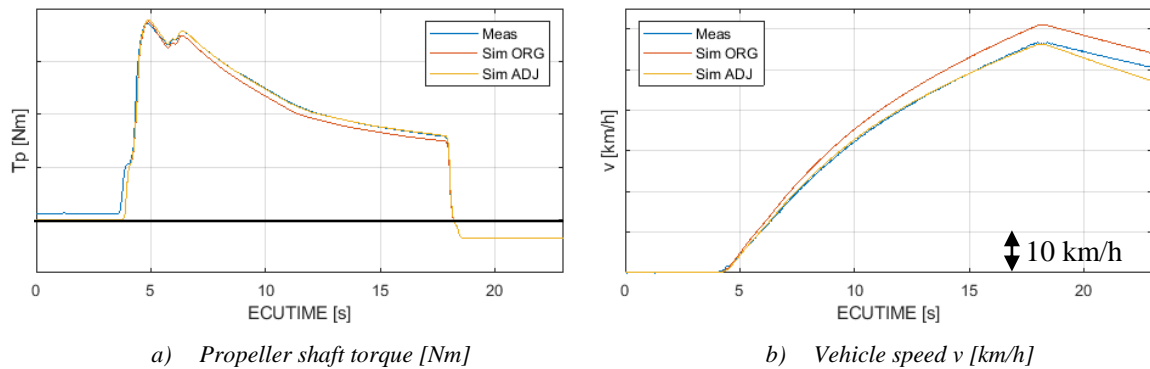


Figure 49 Equation of motion coefficients adjustment example for case 2

At first, there was a big gap between the propeller shaft torque (20 Nm) and vehicle speed (4 km/h) at  $t = 15\text{ s}$  (blue and red lines). A coefficient was adjusted (increased) to match the measurement data in the acceleration part.  $T_p$  matches considerably better in this part than before, vehicle speed is almost identical. But after the accelerator pedal tip-out during the coasting the slope of the speed curve is significantly different, and the vehicle slows down more quickly.  $T_p$  is kept at its maximum for recuperation by MG2. Further adjustment of  $C$  coefficient had almost no impact on the results.

In general, the sensitivity to the coefficients' variation was low. By adjusting the coefficients of the vehicle movement equation, the absolute values were matched well in some manoeuvres. Nevertheless, it was difficult to find the coefficients to keep the trends of vehicle speed and propeller shaft torque in steady speed driving and coasting. Following table 7 shows results of the best solution found for each case.

Table 7 Optimum values of vehicle equation of motion coefficients

Coefficient	Unit	ORG	Case 1	Case 2	Case 3	Case 4	Case 5
<i>A</i>	[N]	167	843	452	1072	653	1038
<i>B</i>	[N/(m/s)]	-	-	-	-15	-	-
<i>C</i>	[N/(m <sup>2</sup> /s <sup>2</sup> )]	0.6647	0.7534	0.4296	0.0997	0.1072	0.0997

It is obvious, that the values are distant from the originally determined road load coefficients. Also, the values for each case are different. No causality with any variable was found. Therefore, it is not able to take the results this study as a solution of the problem of the simulation. The cause had to be searched further.

Two sources of information were used for the road load calculation – the speed profiles and the tire diameter. Speed profiles were measured with a high accuracy, but the dynamic tire radius was estimated. The dynamic tire radius  $R_{t\ dyn}$  is a distance between a wheel hub and the contact point of the tire and the road surface during the vehicle movement. The value is usually calculated based on the free tire radius  $R_{t\ free}$ , when the tire is not loaded, assuming a constant tire deformation expressed by a coefficient  $a_{def}$  (20, 21). Another method is to indirectly determine the radius from measurement of vehicle longitudinal speed  $v$  and wheel rotational speed  $\omega_w$  in (22). [30]

$$R_{t\ dyn} = a_{def} \cdot R_{t\ free} \quad [m] \quad (20)$$

$$a_{def} = (0.95 \div 0.99) \quad [1] \quad (21)$$

$$R_{t\ dyn} = \frac{v}{\omega_w} \quad [m, m \cdot s^{-1}, rad \cdot s^{-1}] \quad (22)$$

The vehicle was equipped with tires 225/50 R18 with a theoretical value of free tire radius  $R_{t\ free} = 0.341\ m$ . The original dynamic tire radius used in the vehicle model in the toolchain and for road load determination was  $R_{t\ dyn} = 0.329\ m$ .

The dynamic tire radius is influenced by many factors, such as the vertical load, wheel speed and the inflation pressure. It means the radius may be dependent on the measurement conditions, therefore the used value did not need to fully correspond with the measurement conditions. Therefore, as a next step, a sensitivity analysis of this coefficient was performed. [30]

The study showed a high sensitivity to a small increase of the dynamic tire radius (in order of millimetres). It was significantly higher than the sensitivity of the road load coefficients. It was found out, that with an increasing tire radius, the toolchain results approach the measured values in all five cases. Also, the trends, especially of vehicle speed and propeller shaft torque, were followed considerably better than before.

The rolling radius was calibrated for the model, and the optimal value was found to be  $r_{t\ dyn} = 0.341\ m$  for all cases. With the new radius, the road load was recalculated again using the same tool with the

same speed profiles. The mean values were selected again. The results are relatively close to the values with the original radius as can be seen in figures 50 and 51 and table 8.

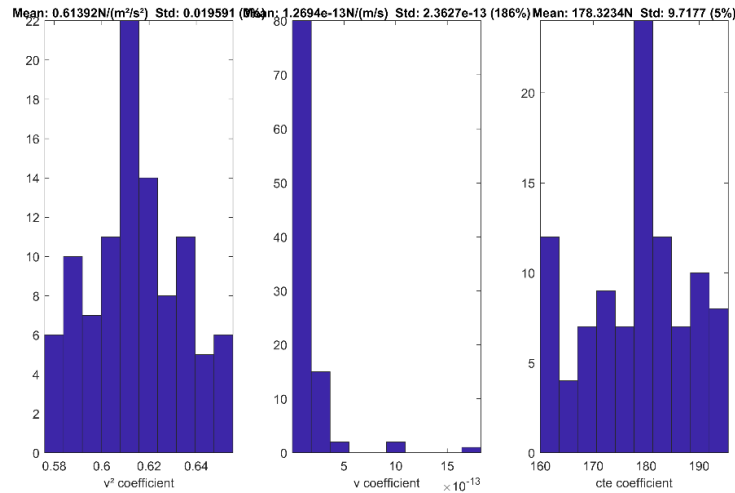


Figure 50 Vehicle equation of motion coefficients probability distribution of variant 1 with new tire radius

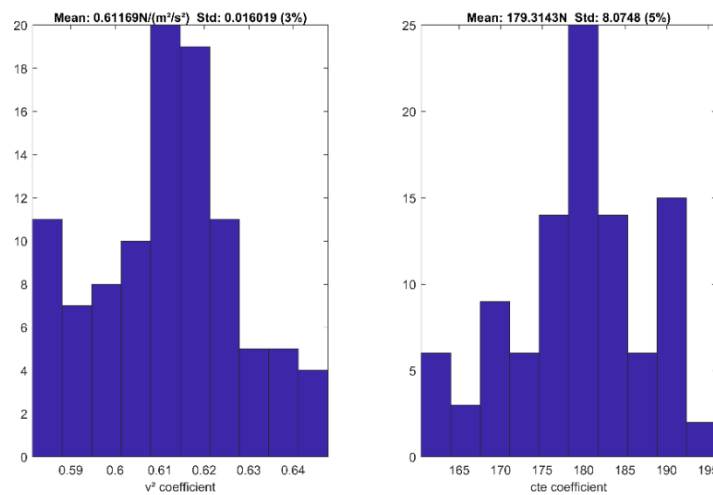


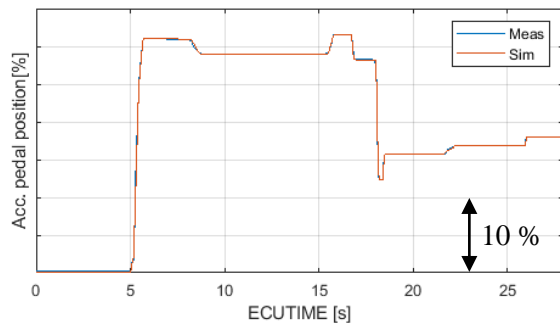
Figure 51 Vehicle equation of motion coefficients probability distribution of variant 2 with new tire radius

Table 8 Final vehicle equation of motion coefficients

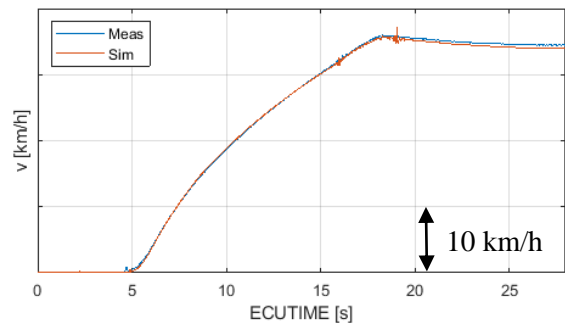
Coefficient	Unit	$R_{t\ dyn} = 0.329\ m$				$R_{t\ dyn} = 0.341\ m$			
		Variant 1	STD [%]	Variant 2	STD [%]	Variant 1	STD [%]	Variant 2	STD [%]
A	N	169.5	5	169.16	5	178.32	5	179.43	5
B	N/(m/s)	$1.478 \cdot 10^{-13}$	114	-	-	$1.269 \cdot 10^{-13}$	186	-	-
C	N/(m²/s²)	0.6625	4	0.6647	4	0.6139	3	0.6117	3

As soon as the new road load coefficients were determined, variant 2 omitting the linear *B* coefficient from the same reasons as before and all cases were recalculated with it. Three of them will be shown and discussed here, the results of the two remaining cases are in attachments.

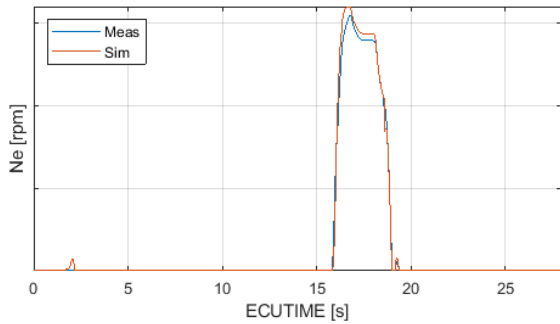
### Case 3



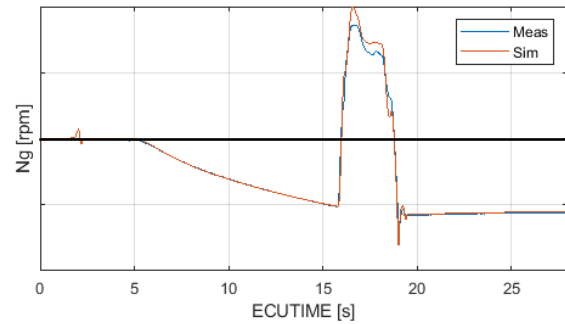
a) Accelerator pedal position [%]



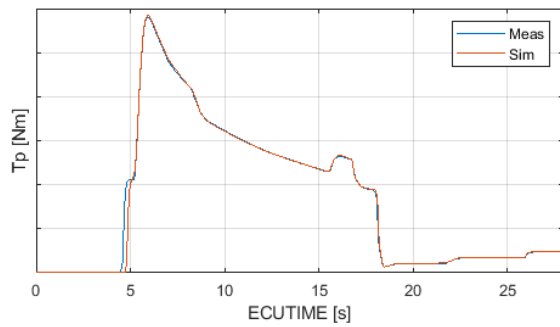
b) Vehicle speed  $v$  [km/h]



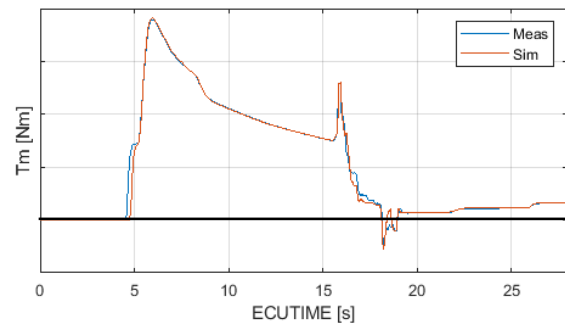
c) Engine speed  $N_e$  [rpm]



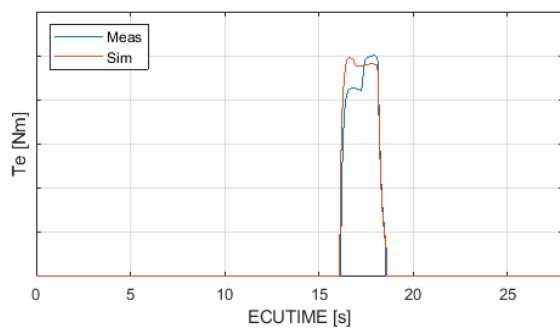
d) MG1 speed  $N_g$  [rpm]



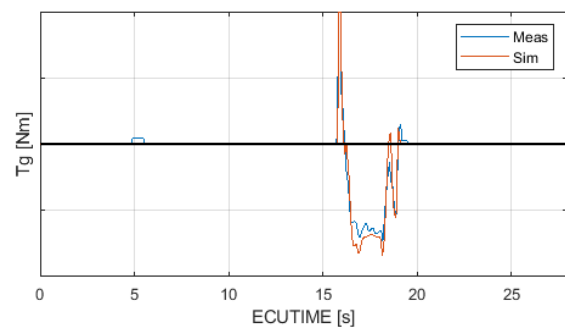
e) Propeller shaft torque  $T_p$  [Nm]



f) MG2 torque  $T_m$  [Nm]



g) Engine torque  $T_e$  [Nm]



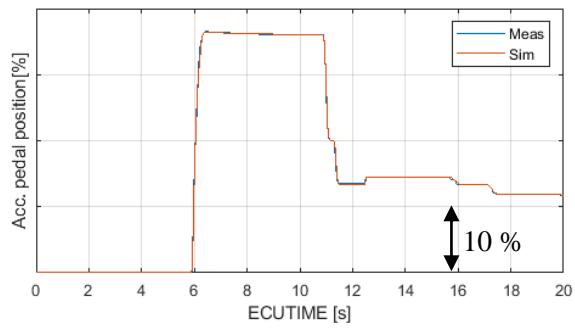
h) MG1 torque  $T_g$  [Nm]

Figure 52 Final results of the top-level validation of case 3

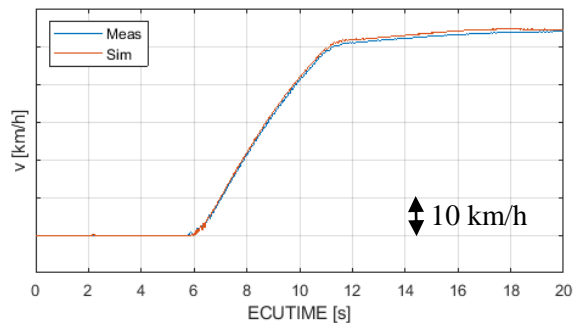
The case number 3 will be discussed now. Originally, it was planned in EV mode. Although there was a choice of a purely EV mode measurement attempt, this attempt in HEV mode was selected in order to show the sensitivity of the toolchain model. In figure 52 a) the accelerator pedal position curve can be seen as the only input to SiL. All other figures are a result of the toolchain. Vehicle speed  $v$  in figure 52 b) as a response to the applied torques is followed well, especially during the acceleration phase. Also, the calculation of the propeller shaft torque  $T_p$  in figure 52 c) is well predicted. The correct prediction is crucial as it is the signal, which is the base for all later calculations in HV-ECU because the logic distributes the load among components. The first rise in the measurement is probably due to the brake release and it seems to be difficult to be modelled in the simulation. Vehicle speed  $v$  in figure 52 b) is followed well, even after 10 s of the steady speed driving, the slope is equal to the measurement and the difference of absolute value is less than 0.5 km/h at  $t = 28$  s. Also, MG2 torque  $T_m$  is predicted with a high accuracy. The propeller shaft and MG2 speeds are not plotted due to the fact they are directly connected to the wheels and hence the vehicle speed.

The toolchain proved a good sensitivity to a small change of accelerator pedal position at  $t = 15.5$  s (in the critical area around 30 %), when due to the higher power requirement switched on the engine. After 2.5 s when the acc. pedal position dropped to 15 %, HV-ECU logic immediately switched off the engine. Some difference in the engine speed  $N_e$  in figure 52 c) and engine torque  $T_e$  in figure 52 g) can be seen in the peak after the start-up. This can be noticed in almost every case. MG1 torque  $T_g$  in figure 52 h) and speed  $N_g$  in figure 52 d) follow the engine behaviour then. The reason is most likely in the simplified EFI-ECU logic and a map-based engine plant model in simulation. There is some difference in values in transient. It is not a big concern until it is explainable, e.g. differences in limitations between the real vehicle and SiL ECUs.

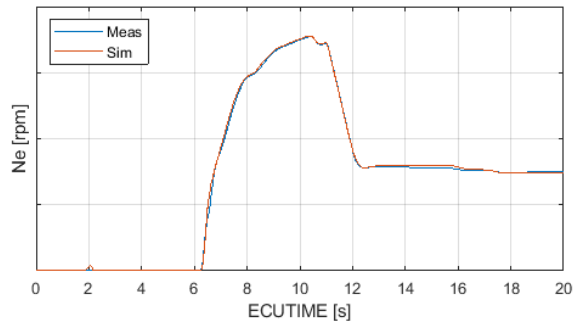
## Case 4



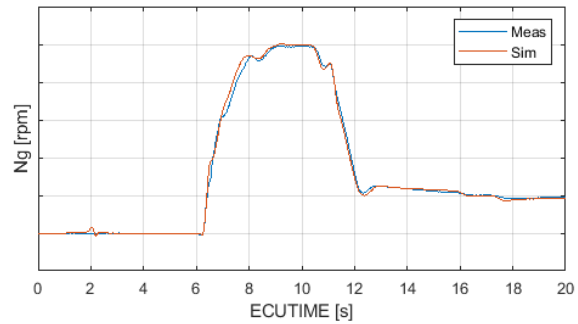
a) Accelerator pedal position



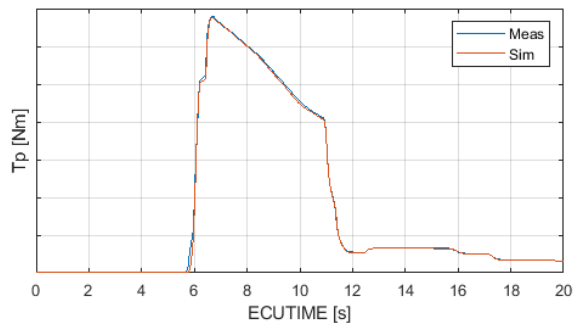
b) Vehicle speed  $v$



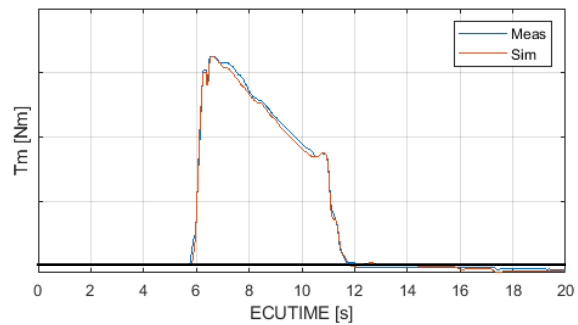
c) Engine speed  $N_e$



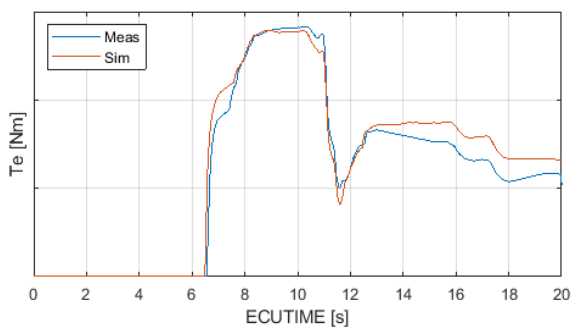
d) MG1 speed  $N_g$



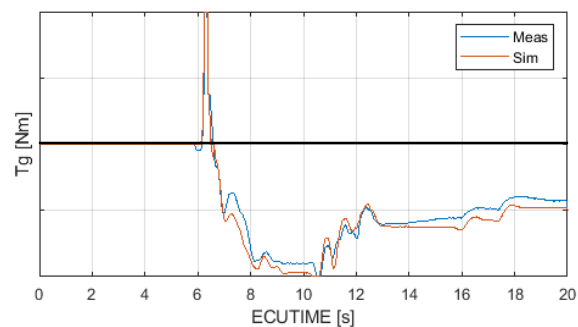
e) Propeller shaft torque  $T_p$  [Nm]



f) MG2 torque  $T_m$



g) Engine torque  $T_e$



h) MG1 torque  $T_g$

Figure 53 Final results of the top-level validation of case 4

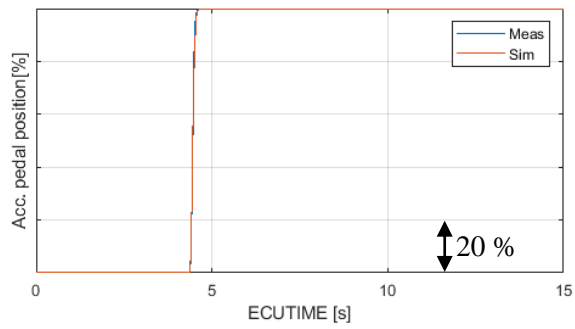
Case number 4 represents the steady speed driving conditions in the HEV mode. The results are shown in figure 53. The vehicle speed is followed well; the highest error is less than 1 km/h. Also, other variables ( $N_e$ ,  $N_g$ ,  $T_p$ ,  $T_m$ ) are followed with a satisfying accuracy. The difference in engine torque  $T_e$  after  $t = 6$  s was explained in the previous case. But a significant difference can be observed in the engine torque  $T_e$  (up to 13 Nm) and MG1 torque  $T_g$  (up to 3.5 Nm) after  $t = 12.5$  s. The vehicle reaches and keeps the steady speed  $v$  around 52 km/h. The  $T_e$  and  $T_g$  demand decrease but the slope is significantly steeper in the measurement. Simply speaking, the power demand for MG1 and hence engine is higher in simulation.

The root cause was searched and identified as a loss in the electric branch of the powertrain in SiL, more specifically in the plant model of the AC/DC inverter and boost converter. In the steady speed driving case, the HV-ECU decides to charge the battery. The power flows then from the engine via MG1 and AC/DC inverter and boost converter to the battery. For the same battery charging request, power request for MG1 (and hence engine) is higher due to higher loss in the path.

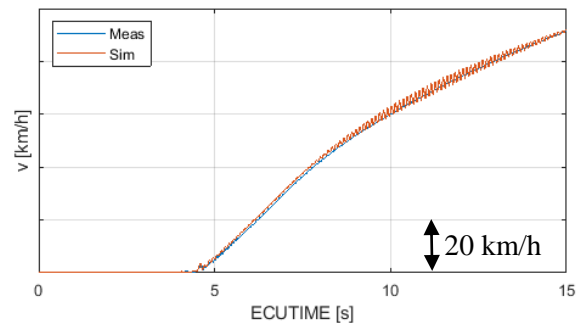
This could bring an issue later, since the high frequency validation is expected to be performed in the steady speed driving conditions. No countermeasures were applied because no data for AC/DC inverter loss map were available. Nor measurement of losses was possible, because no tools and devices were available in this project. Calibration of 2-D loss map would mean an excessive effort with an unclear result. Therefore, the measurement of losses should be considered and performed in the future.



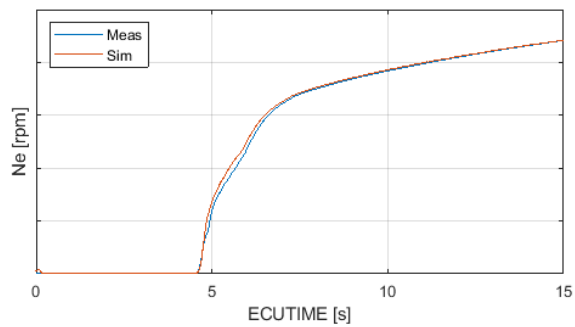
## Case 5



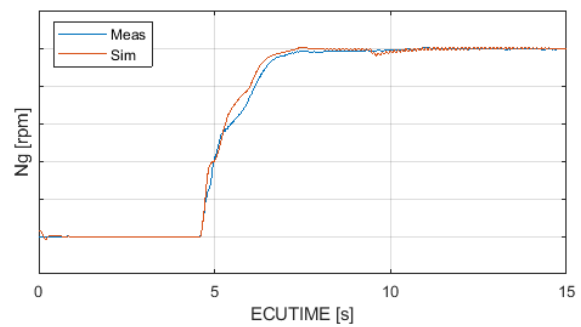
a) Accelerator pedal position [%]



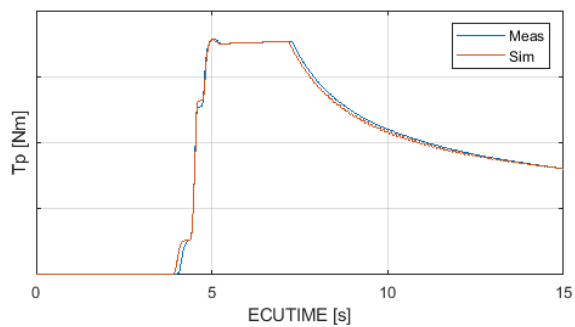
b) Vehicle speed  $v$  [km/h]



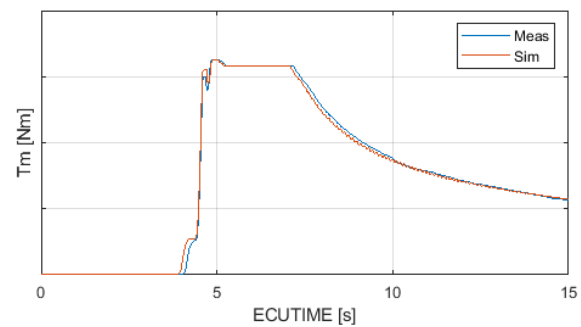
c) Engine speed  $N_e$  [rpm]



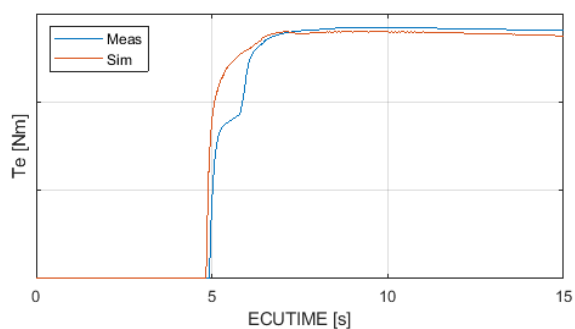
d) MG1 speed  $N_g$  [rpm]



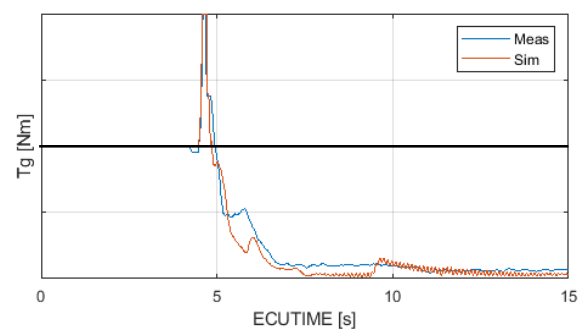
e) Propeller shaft torque  $T_p$  [Nm]



f) MG2 torque  $T_m$  [Nm]



g) Engine torque  $T_e$  [Nm]



h) MG1 torque  $T_g$  [Nm]

Figure 54 Final results of the top-level validation of case 5

The case number 5 was selected as the third case for the top-level validation discussion. It consists of a tip-in (full) acceleration as it can be seen in figure 54.

Propeller shaft torque  $T_p$  and MG1 torque  $T_g$  are followed with relatively low and acceptable error. Engine speed is also predicted well especially after reaching the top torque. The engine torque  $T_e$  has a different course during the first second of engine running. This has the same reason as it has been described for the previous scenario results. After the rev up,  $T_e$  seems to have a slightly different limits, but the difference is never more than 3 Nm (less than 2.1 %). The control logic in SiL seems to have different limits of the MG1 power, therefore it allows to drop MG1 torque to lower values.

After  $t = 8$  s, strong oscillations in the vehicle speed in figure 54 b) can be observed. This is the effect of the TeAC map, when the engine speed is over map's limit at 2000 rpm and the TeAC level crosses the zero line and grows linearly to negative values. The oscillations strongly influence the other variables, too. As they still grow, at  $t = 9.5$  s MG1 power hits the limit and the system reacts with a decrease of the MG1 torque  $T_g$  and MG1 speed  $N_g$ . The logic increases the torque and speed to the limit again but because the overall conditions had changed, this effect does not occur anymore.

#### **5.3.4. Summary**

Five driving scenarios were proposed, measured and replicated in the simulation. The tire radius was calibrated in order to match the results from the measurement. The final results of all cases proved acceptable overall behaviour of the toolchain. It can predict various manoeuvres with a high accuracy. Nevertheless, some limitations of the model are evident. Most of the limits are not a concern for the purpose of this model, which is booming noise prediction in steady state conditions. But the inaccuracy shown in case number 4 due to less accurate electrical loss model should be taken into consideration during the high frequency validation and potentially improved in the future.

## **5.4. Low frequency validation**

When the top-level validation was finished, the low frequency could proceed. In the top-level validation, the general course of signals was examined and evaluated, while for the low frequency validation, the phenomena with frequency higher than 1 Hz will be subjected. The upper limit is represented by the combustion frequency of an idling engine (I4 engine, 1000 rpm), i.e. 33 Hz. Many of the powertrain components are designed with the natural frequency in this spectrum. The main reason is to avoid strong excitation by combustion frequency and hence do not disrupt the passenger's comfort. In an extreme case, it could lead even to a failure of the component.

The low frequency validation should prove the ability of the toolchain model to predict the low frequency phenomena in the drivetrain.

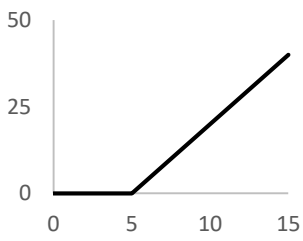
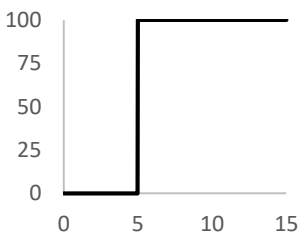
Like in the top-level validation, scenarios were proposed, an experiment with the test vehicle was performed, the data were post-processed, the same boundary conditions were imposed to the model and the results were evaluated.

### **5.4.1. Driving scenarios definition**

The low frequency dynamics phenomena of the powertrain occur in various driving conditions. However, their level can be suppressed, especially during the steady state driving. For a purpose of this validation process, a sufficiently high level of excitation of the drivetrain is needed. The most dynamic response of the system should be seen after a step force input when the natural frequencies of components are excited.

In the real conditions, the step torque input can be approached by a tip-in manoeuvre. In the Toyota Hybrid System, there are two sources of torque –the combustion engine and the MG2. In the hybrid mode they work together to provide the maximum system performance. The synchronous traction motor (MG2) is able to achieve the maximum torque from zero speed, right after the command from the accelerator pedal. This characteristic is favourable as it approximates the step input. Despite to the motor, the performance characteristic of the combustion engine is different and the maximum torque lays in higher engine speeds, therefore the peak value is not available immediately. Because the measurement must always start from the stand still with the engine switched off, the start-up of the engine takes time and prolongs the delay until the engine provides any torque to support the MG2. This behaviour does not contribute to the ideal step force (torque) input. It can even influence the smoothness of the MG2 torque rate. Therefore, the tip-in manoeuvre will be performed only in the EV mode. Thanks to that, any other influence of the engine dynamics to drivetrain can be avoided. This only scenario, performed in the EV mode shown in table 9, should sufficiently comply the requirements for the low frequency validation.

Table 9 Driving scenarios proposals for the low frequency validation

Case	Scenario	Speed profile [km/h]	Acc. pedal profile [%]	Mode
1	Tip-in acceleration from stand still in EV mode			EV mode

### 5.4.2. Measurement

With the scenario proposal, the measurement could be performed. The engine coolant temperature was above 80 °C, transaxle oil temperature above 50 °C and the battery temperature under the limit of overheating.

Table 10 Conditions of the measurement of the low frequency validation scenarios

	Unit	Value
Vehicle mass	kg	1731
Ambient temperature	°C	19
Ambient pressure	kPa	101.8

The purely electric mode was imposed on the vehicle through the open HV-ECU software, so the engine was prevented from a start-up. A calibration map, which controls the rate of rise of propeller shaft torque  $T_p$ , was set to the highest possible value so the torque command reaches the maximum in shorter time and helps to approach the ideal step input. The measurement was repeated several times in order to have a wider spectrum of trials for a possible reproduction by the toolchain model.

### 5.4.3. Evaluation

As well as for the top-level validation, the methodology had to be prepared for the low frequency validation first. The key signals as the propeller shaft torque  $T_p$  and vehicle speed  $v$  should be seen with a high accuracy. Due to the EV mode, the engine torque  $T_e$ , MG1 torque  $T_g$  and the engine speed  $N_e$  are expected to be zero and it is not necessary to evaluate them as well as the MG1 speed  $N_g$ , which is proportional to vehicle speed in the case of the stopped engine. MG2 torque  $T_m$ , as the only power source, should be followed well especially in the area right after the tip-in.

The driveshaft torque was selected as the main evaluation parameter for the low frequency drivetrain dynamics validation. The same frequency with the same amplitude should be visible in the signal from the measurement and from the simulation.

When the measurement and data post-processing were finished, the same boundary conditions (accelerator pedal position, brake pedal position, SOC) were imposed to the toolchain model. The EV mode was fixed by a modification in the HV-ECU code in the toolchain. The stiffness of driveshafts was updated from the measurement of driveshaft stiffness at a dedicated in-house driveshaft test-bench as described in chapter 5.1. and the equivalent stiffness determined from (7). The values are shown in table 11. Correct driveshaft stiffness is essential for the driveshaft natural frequency estimation.

Table 11 Driveshaft stiffness

	Driveshaft	Unit	Original value	Measured value	Equivalent value
$k_{DS LH}$	Left-hand	Nm/rad	6050	5725	11 375
$k_{DS RH}$	Right-hand	Nm/rad	5700	5650	

The results of the validation case are shown below in figure 55.

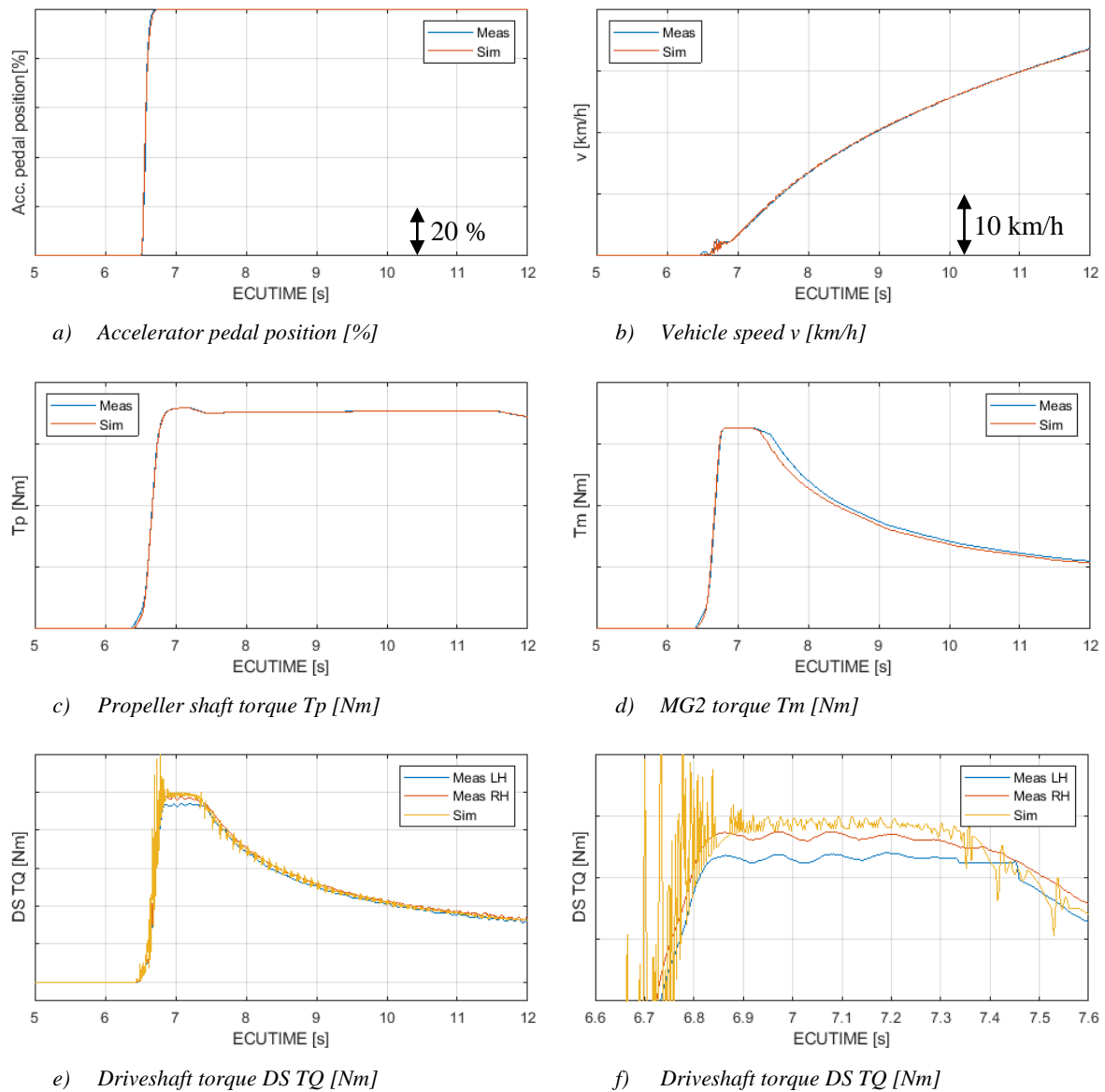


Figure 55 Initial results of the low frequency validation case

The vehicle speed and the propeller shaft torque of measurement are precisely replicated by the simulation. A little time delay (0.12 s) and hence a difference in the absolute values can be seen in the MG2 torque signal. It seems to have a similar cause as in top-level validation – AC/DC inverter and boost converter loss. MG2 approaches the power limit but because of the battery power limitation and a higher loss in the path, MG2 power  $P_m$  in figure 56 b) and hence the torque  $T_m$  is lower. On top of it, an offset in the battery power can be observed in figure 56 a). In total, the difference in plants power (loss) between the battery and MG2 is approximately 0.2 kW in the case of measurement and 1.5 kW in the simulation. This situation occurs at  $t = 7.3$  s, so it has no influence on low frequency phenomena which can be observed between  $t = 6.8$  s and 7.3 s in the driveshaft torque data in the measurement.

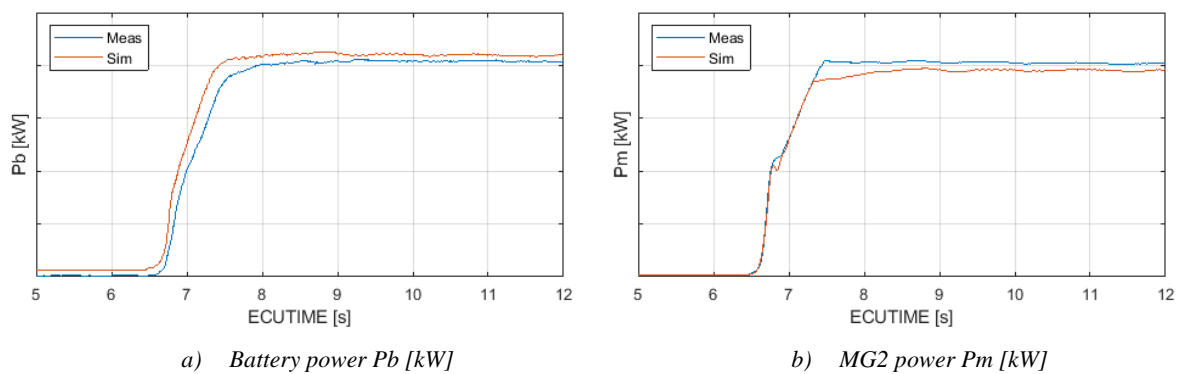


Figure 56 Battery and MG2 power of the low frequency validation case

The driveshaft torque signal can be seen in figure 55 e) with magnified critical area in 55 f). The oscillations in this region have a constant period  $T = 0.11$  s with the corresponding frequency 9 Hz in the measurement data. It was identified as the driveshaft natural frequency. The peak to peak values are almost the same throughout this region and the same for the left- and right-hand sensors, approximately 12 Nm.

In the measurement, the signal from the right-hand (RH – red) sensor is always greater than from the left-hand (LH – blue) sensor by 3 to 5 % throughout the validation case. This phenomenon appears also in the other measured cases. There are several possible reasons for this gap. Firstly, it could mean the measurement inaccuracy, but the driveshaft sensors were calibrated on the driveshaft test bench with a high precision. Secondly, it could be caused by a different stiffness of the left-hand and the right-hand driveshafts and hence a different torque distribution. But the difference between left-hand and right-hand driveshaft stiffness which came up from the measurement on the bench was much smaller (1.3 %). Tire pressure was checked and the same for all wheels. Another possibility is different load of wheels due to the lateral road slope (measurement was always performed on the same test track part) or different weight distribution of the vehicle. The weight records were checked, and the difference was quantified in table 12.

Table 12 Weight distribution of low frequency scenario measurement

Wheel	Unit	Weight	Wheel	Unit	Weight
Front left	kg	514	Front right	kg	495
Rear left	kg	371	Front left	kg	351
Left side	kg	885	Right side	kg	846

The load on front left wheel is higher by 19 kg (3.8 %) than on the front right wheel. The difference is approximately at the same level as the driveshaft torque, but the correlation is not evident. Nevertheless, this difference might be a combination of the phenomena mentioned above. It is not critical for the validation purpose as far as the low frequency dynamics have the same amplitude.

On the other hand, the result of drivetrain dynamics in the simulation can be marked as critical. No low frequency dynamics can be seen in figures, only very high frequency components can be observed. Since the real behaviour of the system is known from the measurement, the toolchain model output has no physical nature so it can be called a noise. Since the control model behaviour, which is mostly decided by SiL, was relatively accurate, the powertrain model was subjected to the investigation.

#### 5.4.4. Model improvements

##### Driveshaft and tire damping

The main consideration lay in the driveshaft and tire models in powertrain model. The root cause was found in the damping of the driveshaft and tire models used. The damping rate was dependent on combustion frequency as described in chapter 4.2.1. in equation (8). Therefore, in the EV mode, when the combustion frequency is zero, the damping rate was almost infinite, so it created additional noise instead of the low frequency dynamics. At first, lumped driveshafts and tires models were undamped separately (with zero damping rate) in order to see the effect of each.

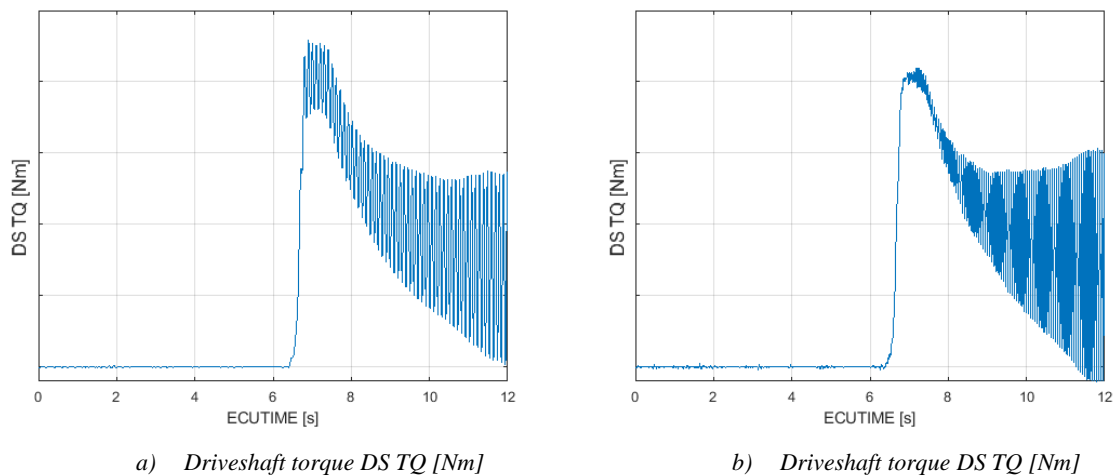


Figure 57 Driveshaft torque with separately undamped driveshaft a) and tire b)

In figure 57 a) with zero driveshaft damping, strong oscillations can be seen. Their frequency is 9 Hz which corresponds with the driveshaft natural frequency. In figure 57 b) with the zero tire damping rate, oscillations with a frequency 17 Hz can be seen. The other components with the same logic of the damping rate calculation (hybrid damper, planet carrier shaft and MG2 reduction shaft) were also investigated with the zero damping with no strong effect on the system dynamics.

A sensitivity study was performed on the standalone powertrain model in Amesim. The boundary conditions ( $T_e, T_g, T_m, N_w$ ) were imposed from the measurement. The advantage of using the standalone model lay in a lower computational time. The target was to learn the behaviour of the system and in the best case determine an approximate value of the driveshaft damping rate  $c_{DS\ eq}$  to match the experimental data. At first, it was verified that the results of standalone model were close to the co-simulation model. The tire damping rate model remained original. Three values of driveshaft torque were taken for evaluation: the highest peak value  $DS\ TQ\ max$ , peak to peak value  $A_{DS}$  of the fifth oscillation and frequency (time period  $T$ ). It can be seen graphically in the following figure 58.

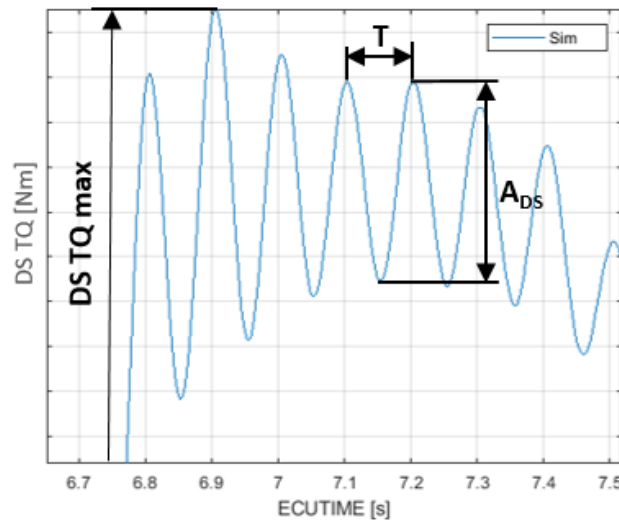


Figure 58 Evaluation parameters of the driveshaft damping sensitivity study



The results were plotted and can be seen in figure 59.

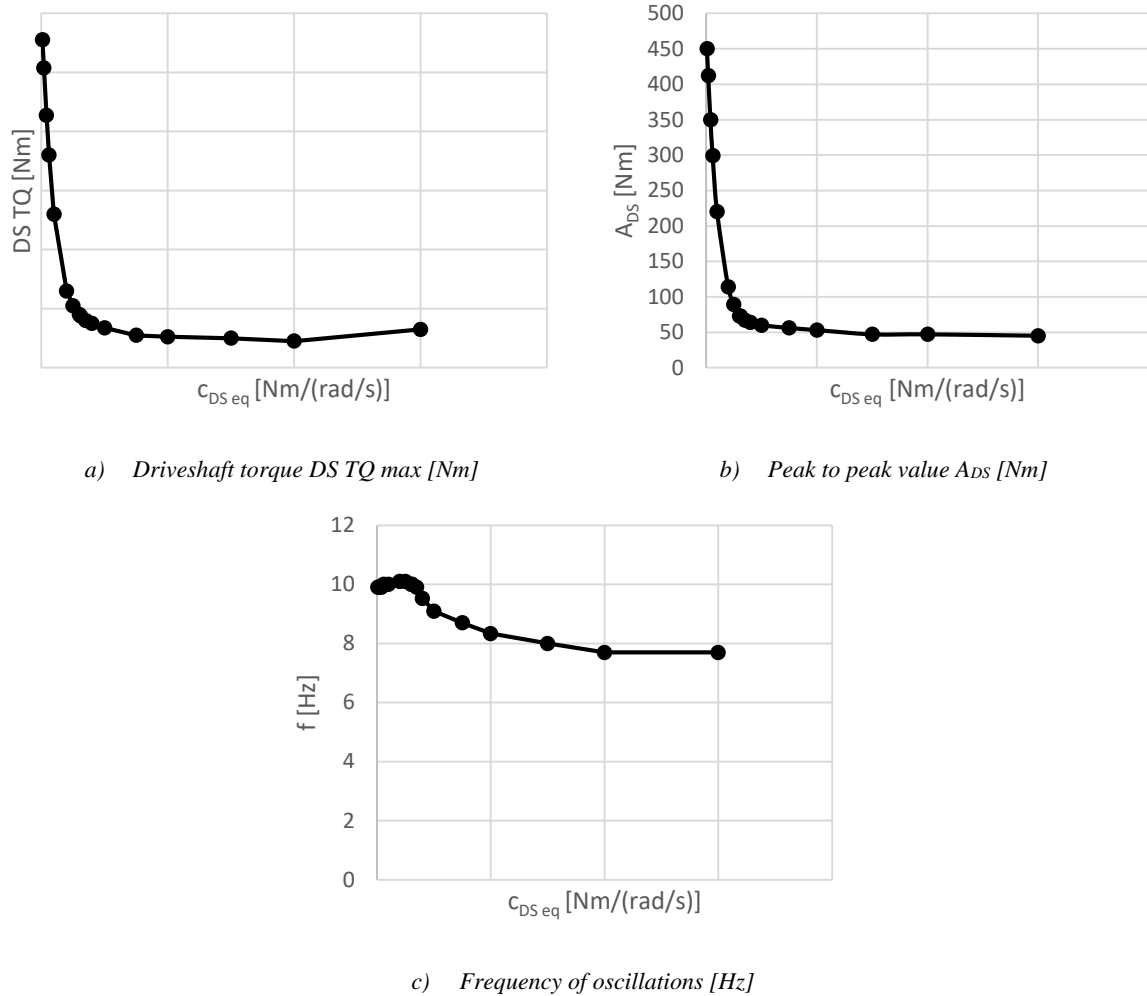


Figure 59 Results of the driveshaft damping sensitivity

The sensitivity study showed the response of the system to the varied damping rate value. As it was expected, the behaviour is strongly non-linear. When decreasing the damping rate, the peak values  $DS\ TQ\ max$  as well as the peak to peak values  $A_{DS}$  were sharply rising. When increasing, the values were relatively stable and practically did not change. The peak to peak values were never lower than 48 Nm, four times higher than the measurement. There is an expected decrease of the frequency, from 10 to 7.6 Hz. Theoretically, it should follow a similar relation of damped vibrations as for a simple example with a mass, spring and damper mechanism.

$$f_d = f_n \sqrt{1 - \zeta^2} \quad [Hz] \quad (23)$$

where  $f_d$  is natural frequency of damped vibrations,  $f_n$  is the natural frequency of undamped vibrations and  $\zeta$  is the damping ratio which can be determined as:

$$\zeta = \frac{c_d}{c_{crit}} = \frac{c_d}{2 \cdot \sqrt{k \cdot m}} \quad [Nm \cdot rad^{-1} \cdot s, Nm \cdot rad^{-1}, kg] \quad (24)$$

where  $c_d$  is damping coefficient,  $k$  is spring stiffness and  $m$  is mass.

The sensitivity study of the driveshaft damping rate did not bring out the optimal value, but it gave a valuable sense of the model behaviour. From this reason, it was decided to use an internal Toyota rule on equation (25) which is used when only the driveshafts stiffness is known. The value lay in the area of the breakpoint in  $A_{DS}$  sensitivity.

$$c_{DS\ eq} = \frac{k_{DS\ eq}}{1000} [Nm \cdot rad^{-1} \cdot s, Nm \cdot rad^{-1}] \quad (25)$$

However, a similar noise in torque signal could be seen in down-stream the tire model because of the original damping model. Therefore, the damping rate of the lumped tires model was set as a single value with the formula of this damping model for constant engine speed  $Ne = 1000\ rpm$ .

### Detailed drivetrain model

Another improvement was applied to the powertrain model. Originally, the end of the drivetrain was simplified and the left- and right-hand components were lumped together. The left and right driveshaft stiffness was not different from each other and the tires were assumed to be the same, but it is more precise to model each component separately (e.g. driveshafts have different stiffness as known from the test-bench measurement). The countershaft was not properly modelled either. Therefore, a new model of the end of the drivetrain was implemented. The model comes from an already existing model of a similar THS powertrain, but some changes had to be made though. The new configuration is shown in figure 60.

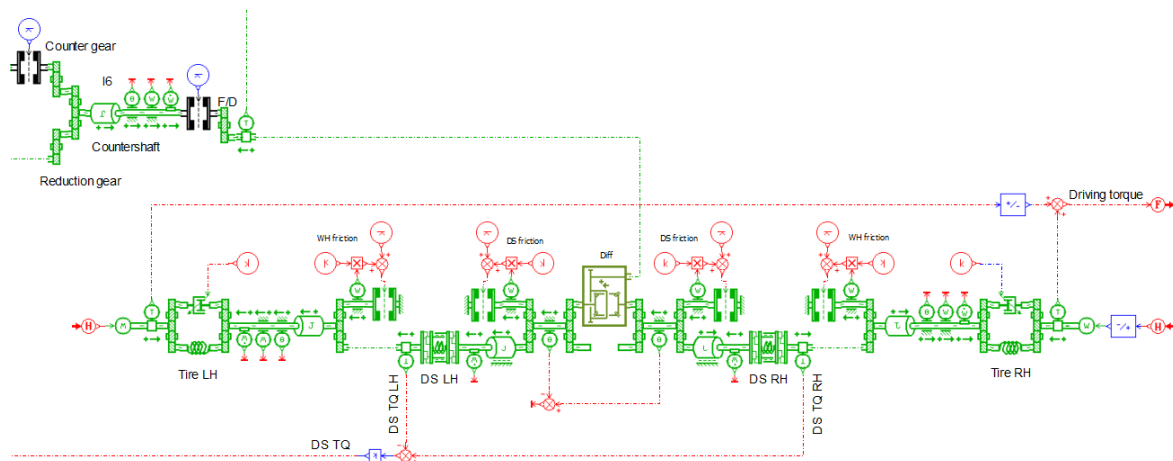


Figure 60 New detailed drivetrain model

This model allows to set the driveshaft and tire properties for left and right side separately. The original values of inertia were split in halves. It also includes the frictional elements, which gives a possibility to consider the frictional loss, but it would require a correction of the road load function in SiL. The friction can be static or linear so the model can express most of the losses in the powertrain. Alternatively, these elements can be used for static  $A$  and linear  $B$  constituents of the vehicle equation of motion (14). The countershaft inertia was moved to a separated block, but its stiffness and damping

properties were unknown, so it was modelled as a rigid shaft. Also the sensor of the driving torque was split in two and moved to a more appropriate position from the countershaft downstream the tire models. This drivetrain model also gives better opportunities for changes in the future.

The scenario was simulated with the toolchain model again. The top-level model behaviour results were almost identical with the results of the lumped drivetrain model as in figure 61. Driveshaft torque from the simulation results (Sim) is the average from left- and right-hand torque sensors in the powertrain model.

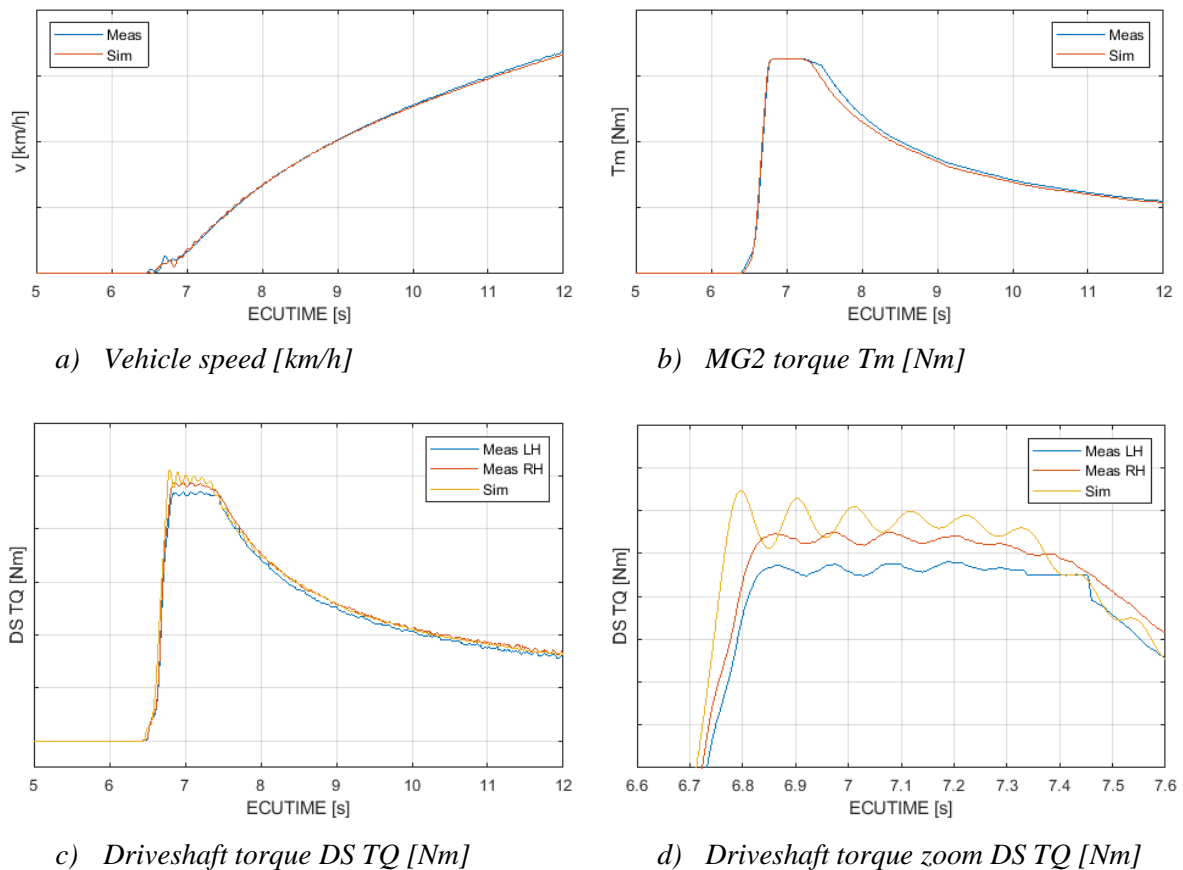


Figure 61 Results of the low frequency validation case

A significant difference can be observed in the driveshaft torque dynamics. While the amplitude remains constant in the critical area between  $t = 6.8$  s and 7.3 s in the measurement, the simulated torque overshoots the measured values and is continuously damped with a decrease of the amplitude. Also, the absolute mean value in this area is higher in the simulation, approximately by 5.8 %. In the measurement, we can see that the rise of driveshaft torque slows down after  $t = 6.7$  s and increases again after  $t = 6.75$  s until it reaches the first peak at  $t = 6.85$  s. In the simulation, driveshaft torque continuously grows until  $t = 6.8$  s without the slowdown.

The root cause was searched in the torque input into the system – MG2 torque  $T_m$ . In the following figure 62, it can be seen, that the blue and yellow line from the measurement and simulation are almost

identical. They represent the same signal of targeted MG2 torque ( $Tm\ tag$ ) from the HV-ECUs in the vehicle and in the SiL model. However, another signal of MG2 torque can be acquired in the measurement from the MG-ECU. This signal is called estimated MG2 torque ( $Tm\ est$ ). It is still not the real value of mechanical MG2 torque, but it is calculated from the MG2 speed, voltage and current which is supplied to MG2 in the real vehicle. These values correspond to the reality better than the targeted HV-ECU signal. When the blue  $Tm\ tag$  signal is compared with the red estimated  $Tm\ est$ , it is obvious that the real MG2 torque is delayed and the same slowdown of rise is present as in the driveshaft torque from measurement. It most likely suppresses the first peak in driveshaft torque in the measurement. This value cannot be retrieved in the simulation. The torque, which enters the powertrain model, is equal to the targeted value. The relatively fast change of the MG2 torque rate probably causes the strong first peak of the driveshaft oscillations.

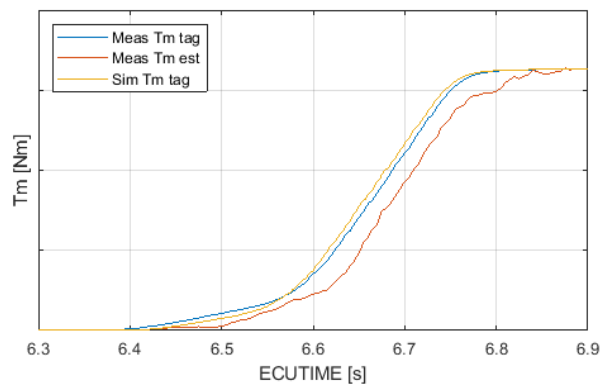


Figure 62 Targeted and estimated MG2 torque  $Tm$

It was also believed that a calibration of the tire dynamic properties could bring an improvement of the toolchain model. The sensitivity study of tire stiffness and damping rate was performed. The methodology and evaluation parameters were selected and shown in figure 63. One parameter was changed while all the others were constant. The high peaks of the first and fourth oscillations were taken into consideration, their peak to peak values (double value of the amplitude) and frequency, measured as time period over four peaks.

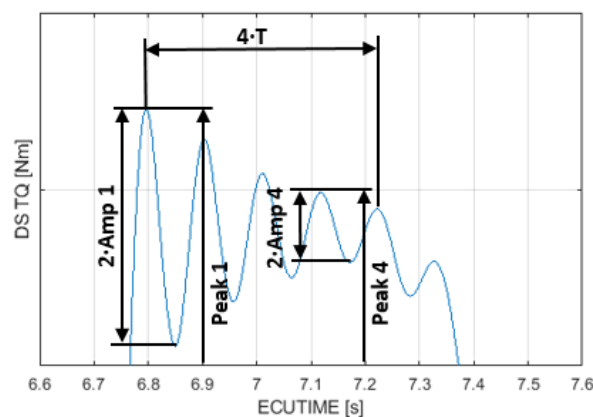


Figure 63 Evaluation parameters of tire stiffness and damping rate sensitivity study

The target was to find an optimal parameters so the first peak and amplitude are lowered and the ratio between  $Amp1$  and  $Amp4$  is ideally equal to one as in the measurement ( $r_{Amp} = \frac{2 \cdot Amp1}{2 \cdot Amp4}$ ). This ratio expresses a relative damping of the driveshaft torque in time. With the current model the first amplitude was three times higher than the fourth one.

Both, tire stiffness and damping rate had rather a minor impact on the results. Both amplitudes changed in order of units of Nm as well as the peak values. Only the amplitude ratio varied in case of tire stiffness but was never lower than 2.4 in the examined region (the base point is the middle one in figure 64).

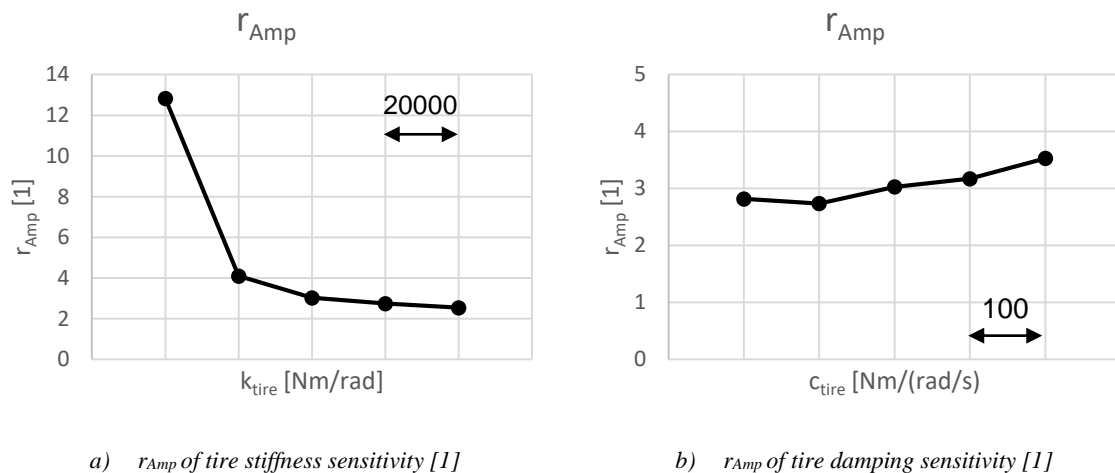


Figure 64  $r_{Amp}$  of tire stiffness and damping sensitivity study

The sensitivity study did not bring any fundamental scope for improvement of the model, therefore it was decided to finish the low frequency validation with the current model status with results shown in figure 61.

### 5.4.5. Summary

For the low frequency powertrain dynamics validation, the EV tip-in driving scenario was proposed and measured. This case was replicated by the toolchain model. Several improvements were applied to the model. Nevertheless, the absolute values and amplitudes of the final driveshaft torque are higher in simulation and their magnitude decreases with time in the final results, the frequency is predicted well and also the general trends are captured by the toolchain model. It can be evaluated as sufficient for the booming noise prediction model, since the low frequency phenomena are not critical.

## 5.5. Powertrain block movement validation

Besides the low frequency phenomena, the powertrain block movement validation is also covered in the validation process. It should prove capability of the toolchain model to predict correct powertrain movement, in other words validate the accuracy of the powertrain mount model. The powertrain mounts parameters were identified and together with the powertrain block, their models were developed as a part of the powertrain model in the work of my predecessor as mentioned in chapter 4.2.1. They have never been validated by a test vehicle. The same scenario as for low frequency validation (EV tip-in) was used for this purpose.

At first, it is necessary to define the coordinate systems because LMS Amesim uses several frames. The base frame is the absolute ground frame  $R_0$  with the x-axis towards the front of vehicle. The vehicle frame  $R_1$  axis is solid to the ground frame and its origin is in the centre of gravity of the vehicle. The engine uses the inertia frame which comes from the mass and inertia measurement of the block. Its origin is located in the powertrain block centre of gravity.  $R_4$  is the powertrain block frame, parallel with the vehicle frame, which allows all the dynamic expression and computation for the Newton – Euler’s law application. Its origin is located again in the powertrain block centre of gravity. The relation between the powertrain block frame and the inertia frame is via constant Euler angles  $\theta_1 = \theta_{yz}$ ,  $\theta_2 = \theta_{xz}$  and  $\theta_3 = \theta_{xy}$ . The frames are shown in figure 65.

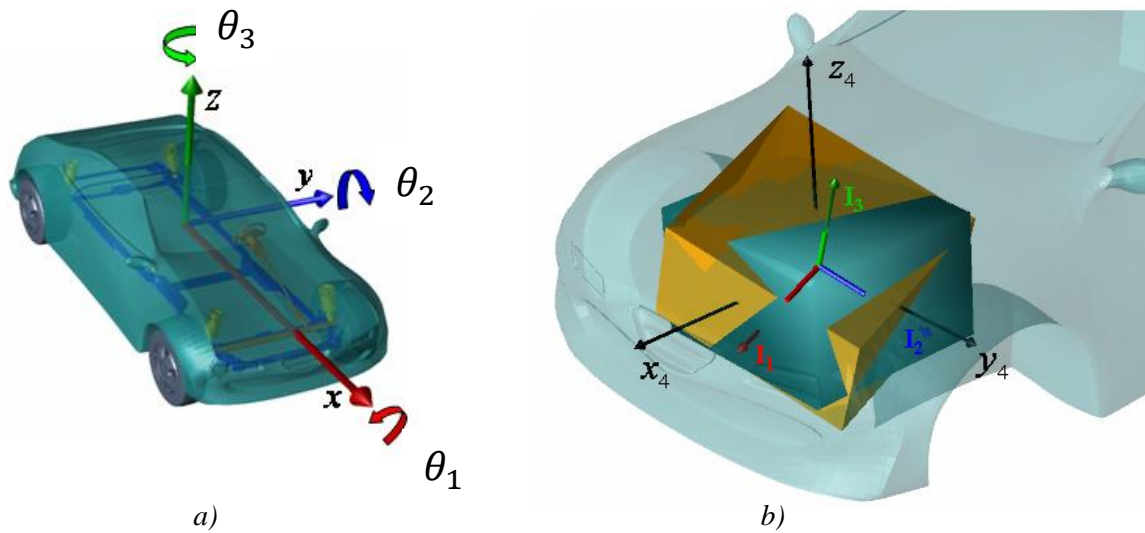


Figure 65 Vehicle  $R_1$  frame a), powertrain block  $R_4$  and inertia  $R_{inertia}$  frames b) [31]

The powertrain block movement is always a complex 3-D movement. The  $R_4$  frame will be used with direction notation  $x, y, z, \theta_1$  (roll),  $\theta_2$  (pitch) and  $\theta_3$  (yaw) with the right-hand rule for angular movement. LMS Amesim, as a part of the toolchain, calculates the complex powertrain block movement in the powertrain block element with respect to its centre of gravity as a result of the powertrain mounts response. In measurement, only three specific pieces of information were obtained from the stroke sensors described in chapter 5.1. Therefore, it was necessary to develop a methodology

for validation. Now, the results of relative powertrain movement in respect to its centre of gravity from the toolchain will be shown:

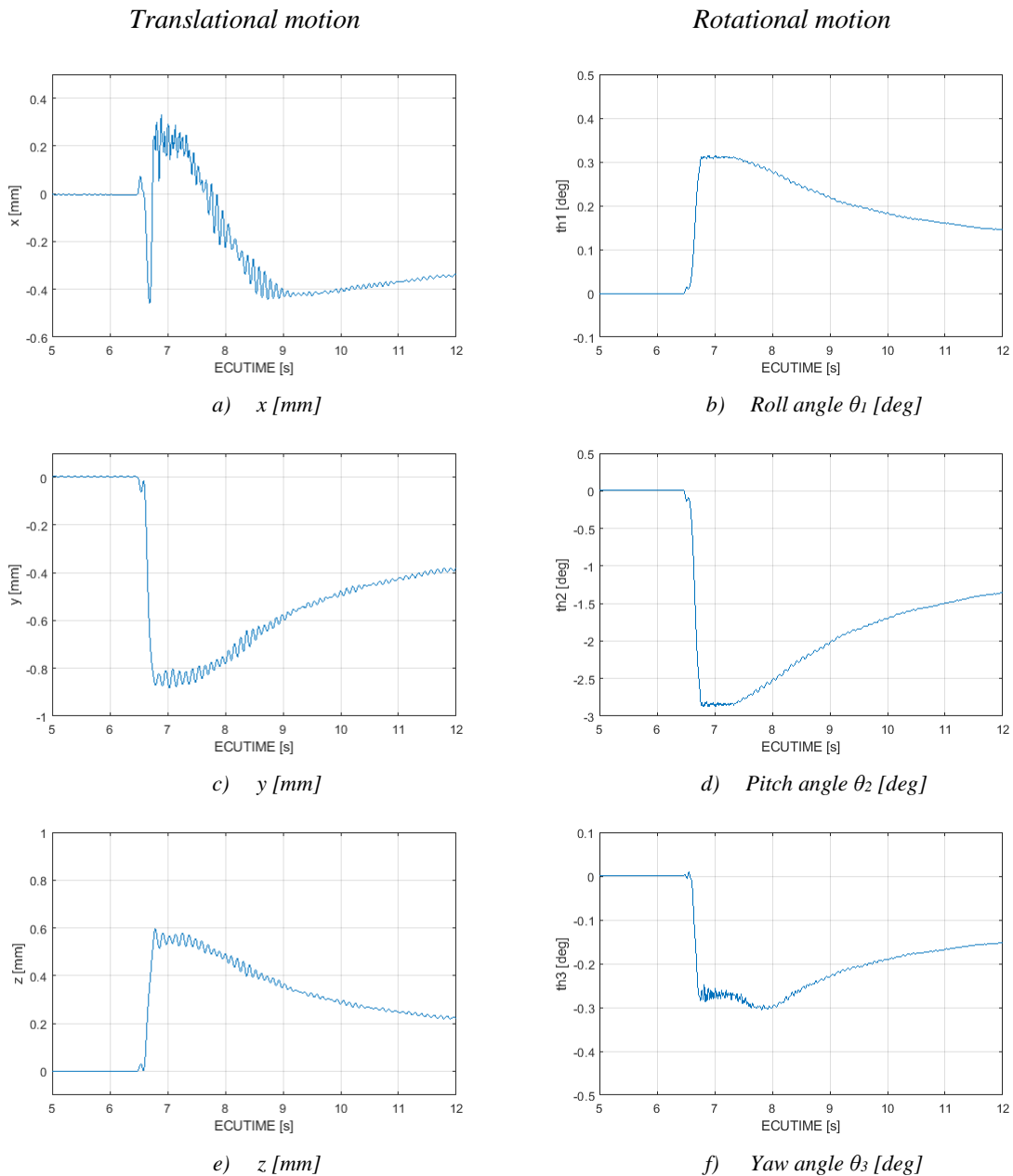


Figure 66 Powertrain block movement in respect to centre of gravity in simulation

As can be seen in figure 66 a), the centre of gravity of the powertrain makes an initial shake back and forth and later settles backward the original position. It moves a bit to left and up (figures 66 c) and 66 e)). The displacements are relatively low, never exceeding 0.85 mm in any direction. It corresponds with the tendency to design the geometry of mounts to not let the centre of gravity move in order not to influence the vehicle performance. In the rotational movement, pitch in 66 d) clearly prevails over roll and yaw (figures 66 b) and 66 f)). The value of pitch angle is approximately ten times higher than the other two (2.8 degrees to 0.3 degrees in peak values). The top of the powertrain block leans towards the vehicle cabin. This corresponds with the assumption of the torque roll axis. It is expected that the

powertrain block rotates around this torque roll axis. The powertrain mounts make the reaction to the torque applied to driveshafts and wheels. Therefore, the correct driveshaft torque prediction is fundamental and was proven above. The position of the torque roll axis is not fixed and varies under different load conditions. No effect of the suspension system is considered in this case.

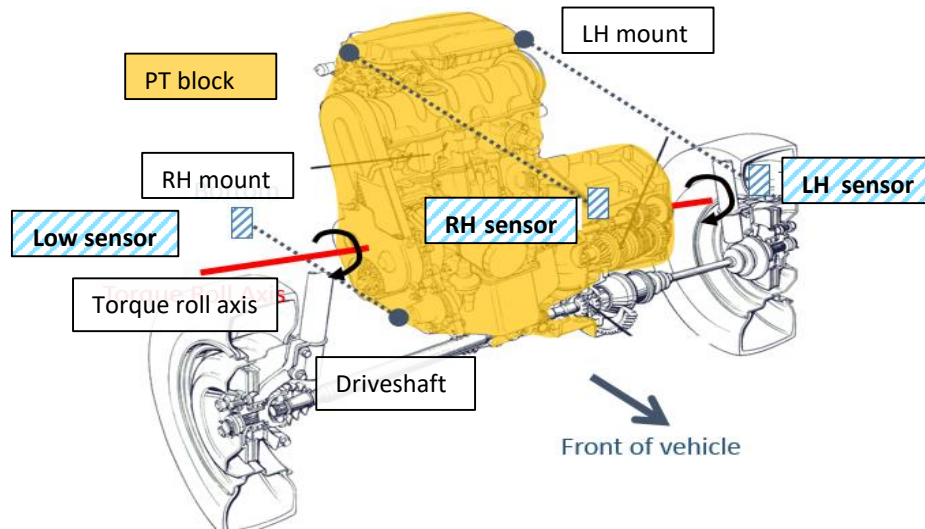


Figure 67 Powertrain with stroke sensors and the torque roll axis

Figure 67 shows the approximate locations of the displacement stroke sensors fixed on the body and attachment points on the powertrain block as installed in the test vehicle. There are two top sensors (LH sensor and RH sensor) and one sensor in the bottom (Low sensor) close to torque rod mount. Their geometrical location was measured in respect to the mounts. The connecting wires are nearly in horizontal and longitudinal position.

Since it is clear that the pitch movement is dominant in the powertrain block movement under driving conditions, the case can be simplified into 2-D. Displacements in the points of attachment points will be calculated based on the pitch angle  $\theta_2$  which was obtained from the toolchain model-based on the same input of accelerator pedal position from the measurement. The geometry comes from the measurement. These values are comparable to displacements measured in the real vehicle. The course of this process can be seen in figure 68.

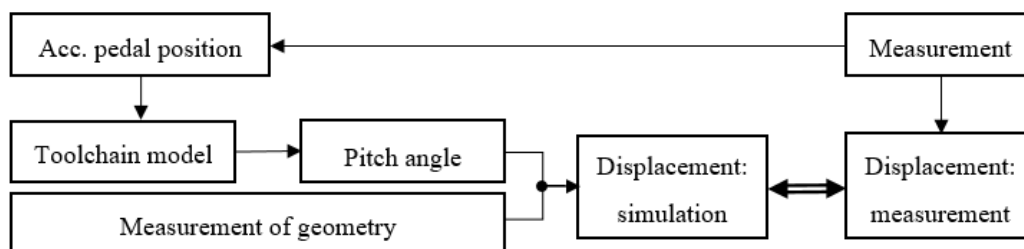


Figure 68 Course of powertrain block movement validation process



The methodology will be demonstrated for one top stroke sensor in the following figure 69. All the locations are known thanks to powertrain block model in LMS Amesim (centre of gravity – powertrain mounts) and measurement (powertrain mounts – stroke sensors). The vertical position (in z direction) of the left-hand and right-hand stroke sensors is nearly the same. The centre of gravity is represented by the orange point in the origin of the coordinate system. The red point is the position of the stroke sensor and the green cross (T) marks the original location of the attachment point on the block in unloaded state. Also, the low stroke sensor (blue point) and its attachment point (orange cross) are depicted.

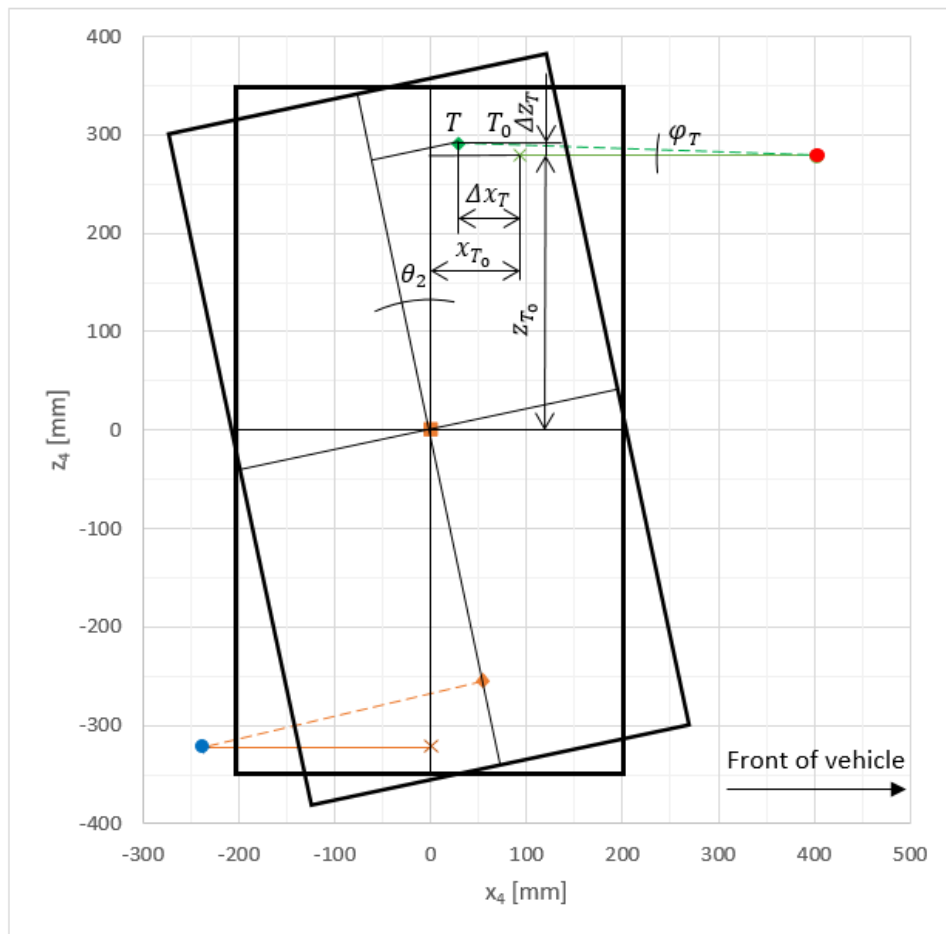


Figure 69 Powertrain block movement methodology

Another simplification comes when the system is loaded. The powertrain block is assumed to rotate around its centre of gravity because the location of the torque roll axis was unknown. The only assumed displacement is the pitch angle  $\theta_2$ . Then the attachment point changes its position from  $T_0$  to  $T$ . The movement can be decomposed into x and z directions. The displacement can be expressed as:

$$\Delta x_T^{\theta_2} = x_{T_0}(\cos(\theta_2) - 1) + z_{T_0} \cdot \sin(\theta_2) [m, deg] \quad (26)$$

$$\Delta z_T^{\theta_2} = z_{T_0}(\cos(\theta_2) - 1) + x_{T_0} \cdot \sin(\theta_2) [m, deg] \quad (27)$$

The total displacement would be under the conditions of pure pitch (axis of rotation is parallel with the  $y_4$  axis and position of stroke sensor wires is initially horizontal) as follows:

$$\Delta l_T^{\theta_2} = \sqrt{\Delta x_T^{\theta_2^2} + \Delta z_T^{\theta_2^2}} \Leftrightarrow \text{rot} \parallel y_4, \varphi_{T_0} = 0 \text{ deg [m]} \quad (28)$$

The question mark is in the reliability of this method from a reason of rotation axis which is mostly not identical with the centre of gravity and also shifts under load in reality. Therefore, a refinement of the method was applied.

The torque roll axis position can be determined from a mechanical principle, that the actual axis of rotation is a point or line with zero translational velocity. It can be found as a cross-section of a connecting line of top and low attachment points and connecting line of the velocity vectors in attachment points as shown in figure 70.

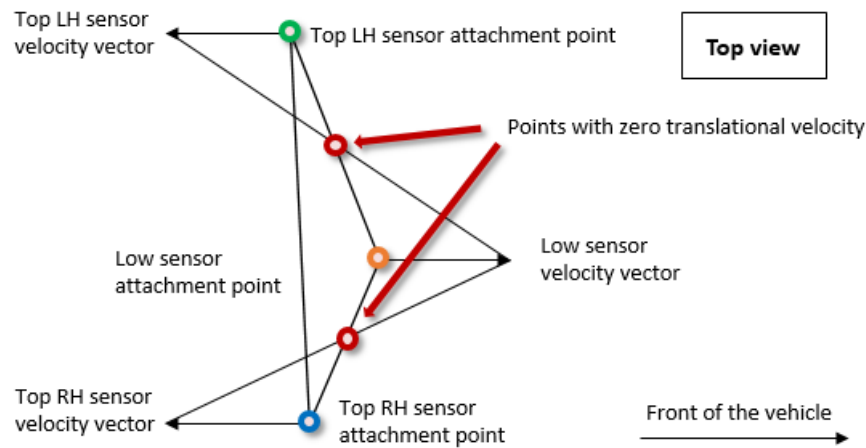


Figure 70 Points with zero velocity for the new axes of rotation

The position of these points with zero velocity was found based on known geometry of the system and the velocity vectors, which could be obtained as a differential of the stroke sensors displacement data from the measurement. The distance of these points to the centre of gravity was incorporated into  $x_{T_0}$  and  $z_{T_0}$  constituents in (26, 27) for each side. The new course of the validation process can be seen in figure 71.

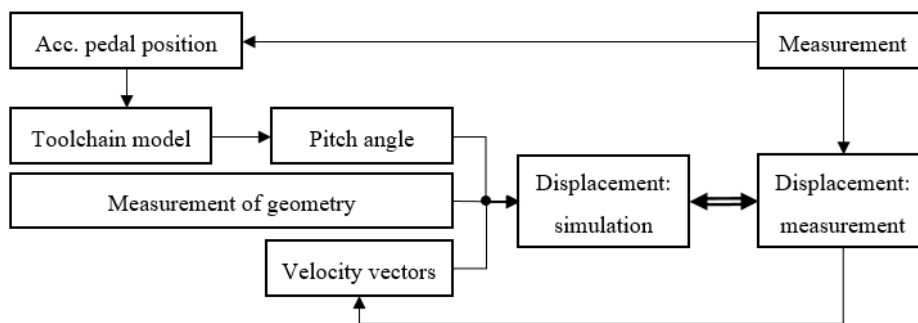


Figure 71 Course of the powertrain block movement validation process with a new torque roll axis

It was assumed that the torque roll axis is led in these points in lateral direction (parallel with  $y_4$ ), e.g. for the left and right side separately. For the displacement in the low attachment point the average of them was considered.

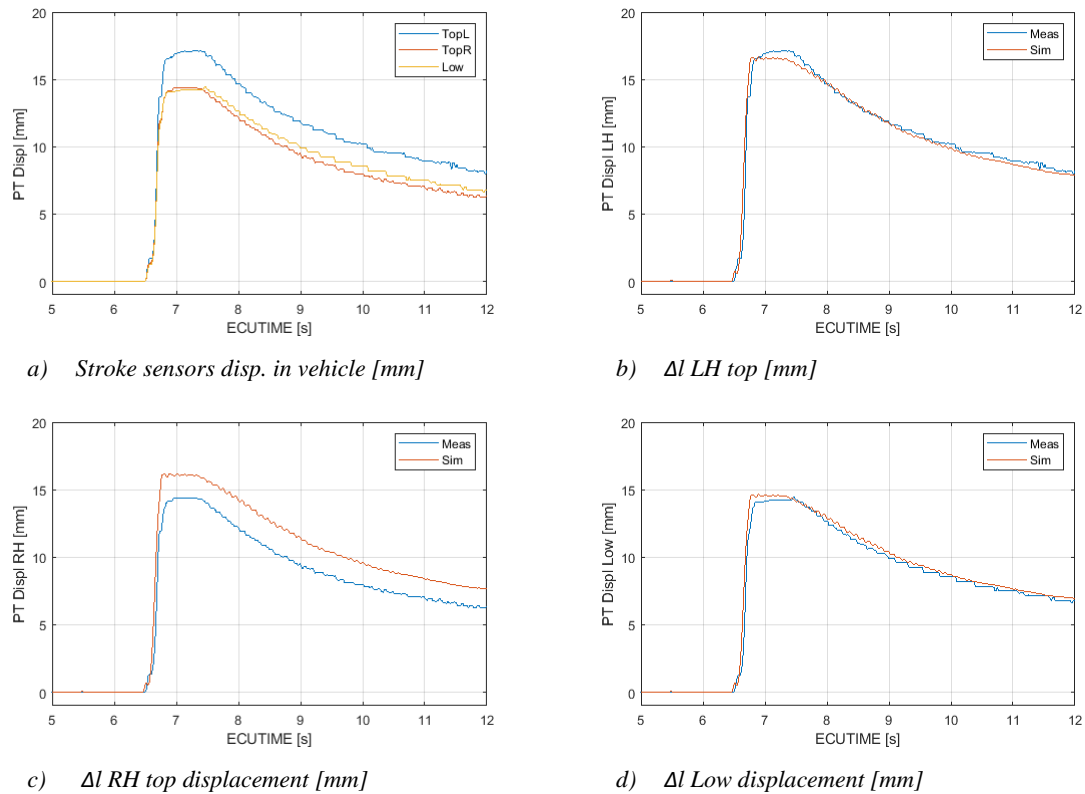


Figure 72 Final stroke sensors displacement results

In figure 72 a), the displacements from all three sensors in the vehicle can be seen. The displacement of the top left-hand (TopL) is approximately 2 mm higher than the right-hand one (TopR). This is most likely caused by the complex 3-D movement of the powertrain block, since the connecting line of top mounts is not aligned with the real torque roll axis. By coincidence, the displacement of the low sensor (Low) is almost identical with the top right-hand. The powertrain stroke sensors cannot capture any dynamics due to their construction type (even small steps in values are visible after  $t = 8$  s).

When being compared with the simulated data, it is obvious that the shape of curves that corresponds with the pitch angle as a result of applied MG2 torque. The results for the top left-hand and low attachment points displacement are almost identical with the measurement. The difference of top right-hand is around 1.5 mm at  $t = 7.2$  s.

The powertrain block movement in the quasi-static condition is predicted with the acceptable accuracy. Therefore, the powertrain mounts models under quasi-static condition are validated with a positive result. The remaining gap between the measurement and the model relates to the simplifications made in the validation process and experimental measurement principle. No dynamics could be compared since the stroke sensors were not able to capture them due to the measurement principle.

## 5.6. High frequency validation

The last validation step is the validation of the model in high frequency dynamics, which is the key for NV booming activity in this work. The subjected frequency range, in this case, is defined by the combustion frequency between 33.3 Hz ( $Ne = 1000 \text{ rpm}$ ) and 50 Hz ( $Ne = 1500 \text{ rpm}$ ). The high frequency validation should prove ability of the toolchain to predict the high frequency phenomena, more specifically the low speed booming noise in terms of frequency and amplitude caused by combustion. Phenomena outside this region of frequencies (e.g. driveshaft and powertrain mounts natural frequencies) will be considered, too, but with a lower priority. The booming noise will be evaluated on the powertrain side when it is propagated by the structure-borne mechanism.

The validation process will be carried out in the same manner as the top-level and low frequency validation. Driving scenarios were proposed first, the experiment was performed in the vehicle, data were post-processed, the same boundary conditions (will be explained in next sections) were imposed to the toolchain model and its results were evaluated or an improvement was proposed if needed.

### 5.6.1. Driving scenario definition

At first, driving scenarios were proposed. The measurement is done under PT load conditions which are relevant for NV booming phenomena. It means to subject the combustion engine to low engine speed and high load. This area is usually restricted by the control logic of booming noise avoidance as described in chapter 3.3.4.1. Similar approach of noise avoidance is also used for other noises in powertrain. Therefore, all NVH calibration maps must be disabled.

Since the engine is stable source of constant torque for booming noise, it is favourable to measure relatively long period of time under steady driving conditions for evaluation. Nevertheless, the HV-ECU can decide to shut down the engine immediately after reaching the steady state where the driving power demand is low. Thanks to the open ECUs in the test vehicle, the engine can be kept running at fixed rotational speed.

When the engine speed is fixed, the power demand for steady driving is relatively low, engine torque is mostly far below the maximum available torque. The load can be varied by vehicle speed (change in road load) but THS allows another option which is more controllable and precise. In order to increase the load and induce stronger torque fluctuations of the engine, charging request for battery can be modified externally through the open ECU.

Twelve driving scenarios were proposed in order to cover the critical area. The parameters varied are engine speed  $Ne$ , battery charging request  $Pb_{req}$  and vehicle speed. Three engine speeds were selected (1000, 1250 and 1500 rpm). For each engine speed the full load and part load case should be measured. For this reason, different battery charging requests were selected. For every combination, measurement was done at 20 and 40 km/h. All the proposed cases are shown in table 13.

Table 13 Driving scenarios proposals for high frequency validation

Case number	Engine speed $N_e$ [rpm]	Battery charging request $P_{breq}$ [kW]	Vehicle speed $v$ [km/h]
1	1000	5	20
2			40
3		8	20
4			40
5	1250	8	20
6			40
7		10	20
8			40
9	1500	10	20
10			40
11		13	20
12			40

As in previous validation processes, the measurement starts from standstill. The vehicle is brought to the desired speed which is held constant until the end of measurement by driver. Once the desired vehicle speed is reached, the accelerator pedal position is kept constant in order not to vary system torque command. Then, the charge request and engine speed are fixed. Measurement of the steady section under these conditions mentioned above should last at least 10 s for each case so that transient phenomena are avoided and a sufficient amount of data for evaluation is acquired.

### 5.6.2. Measurement

With scenario proposals, the measurement could be performed. The engine coolant temperature was above 80 °C, transaxle oil temperature above 50 °C and the battery temperature under the limit of overheating likewise the previous validation cases.

Table 14 Conditions of the measurement of the high frequency validation scenarios

	Unit	Value
Vehicle mass	kg	1728
Ambient temperature	°C	23
Ambient pressure	kPa	102.9

### 5.6.3. Evaluation

Driveshaft torque was selected as the main evaluation parameter. The frequencies and amplitudes from the simulation should match ideally with the measurement signal. The amplitude of combustion frequency is prioritized over others. Six cases from the measurement, two for each engine speed with a different load, were selected for validation (cases 1, 2, 6, 7, 10 and 12). The same approach was selected again. The same boundary conditions (accelerator pedal position, SOC) were imposed to the toolchain. The same modifications were done in the HV-ECU code (NVH maps disabled, battery charging request and engine speed fixed). Toolchain with the latest version of the powertrain model from the low frequency validation was run. The comparison of simulation and measurement results of

case 6 can be seen in figure 73. The green area highlights the area of interest. The results of other scenarios are in attachments.

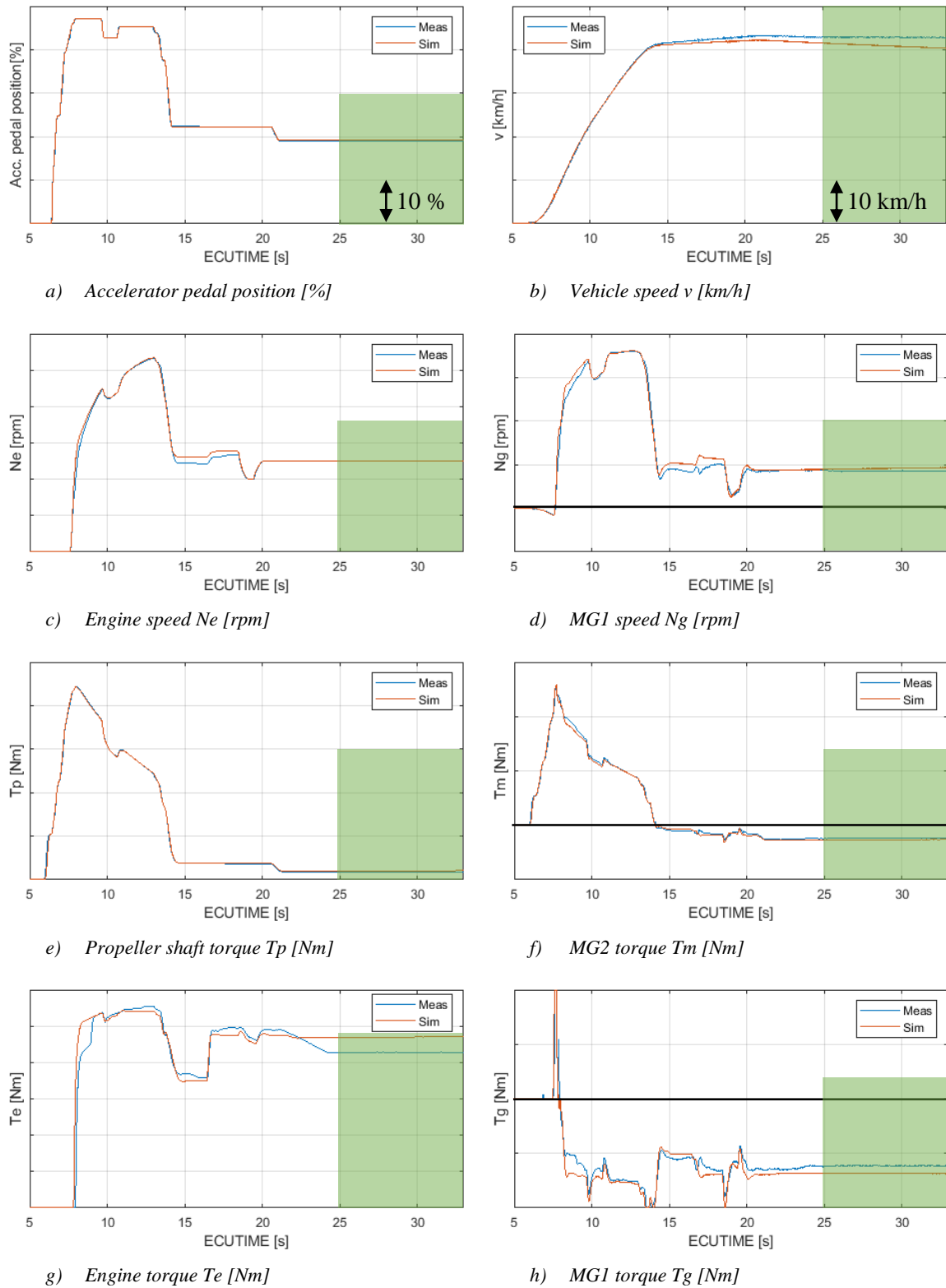


Figure 73 High frequency validation results of case 6

The accelerator pedal position as the input to the simulation is followed well. Vehicle speed  $v$  was followed with a relatively small error until the charging request was introduced at  $t = 16.4$  s. Then it

started to differ until the end of measurement at  $t = 33$  s, when the error was 2.5 km/h. Engine speed was followed well, especially after its fixing at  $t = 18.4$  s when  $N_e = 1250$  rpm. MG1 speed  $N_g$  is a consequence of the engine and vehicle speed, therefore a growing gap due to not precise prediction of the vehicle speed can be observed. The prediction of the propeller shaft torque  $T_p$  and MG2 torque  $T_m$  is relatively well followed. It can be seen that MG2 generates electricity due to fact, that MG1 generating power limit was reached. A significant difference can be spotted in the engine and MG1 torque signals  $T_e$  and  $T_g$ . After  $t = 21$  s engine torque in the vehicle decreases until it stabilizes at the constant level at  $t = 24$  s while it settles at higher value in the simulation. This gap is caused by the loss modelling in electrical part (boost converter and inverter) as described in chapter 5.3.3. Since there was not an effective countermeasure to remove this error, it must be always considered during the evaluation process. The evaluation of the driveshaft torque in the high frequency validation should be always performed in the area, where the variables are constant, in this case, after  $t = 25$  s.

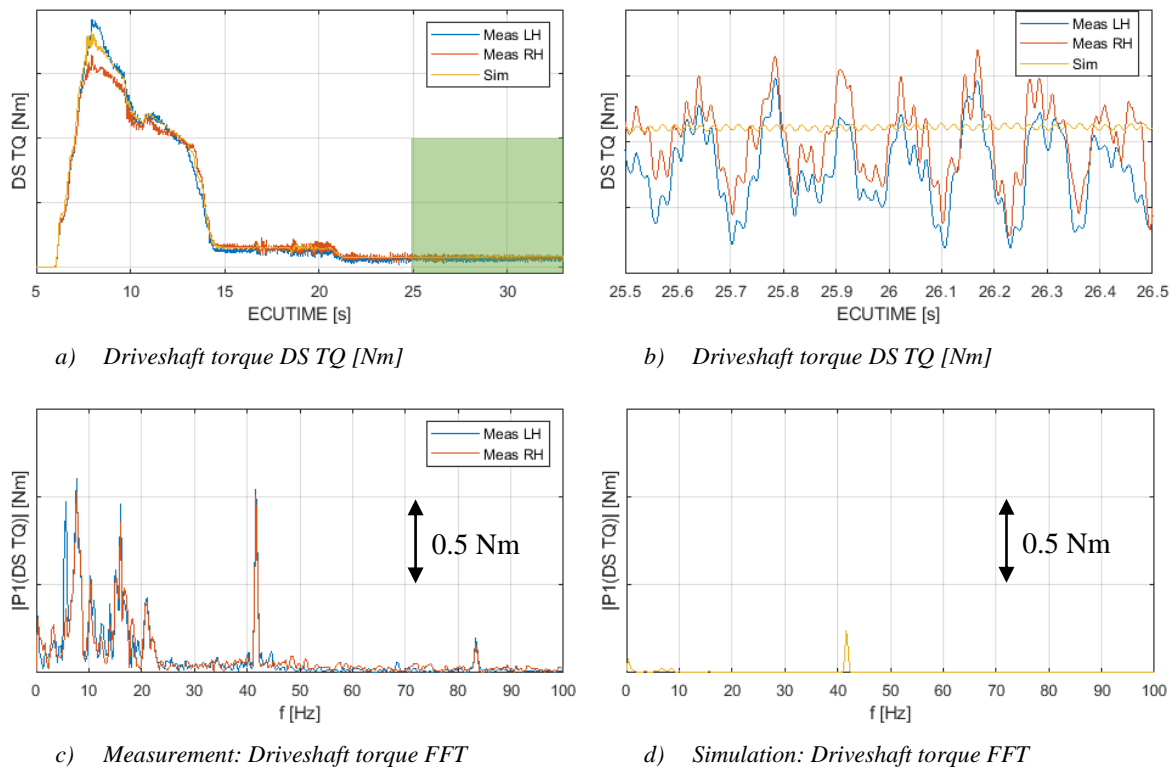


Figure 74 Driveshaft torque analysis of case 6

Driveshaft torque as the evaluation parameter is followed with a sufficient precision at the absolute level as can be seen in figure 74 a). When the signal is magnified in a time window of 1 s in the area of interest, the signals from measurement and simulation clearly differ in their dynamic pattern. In the measured signals, the values are slightly higher for the left- and right-hand driveshaft torque sensor. The possible reasons were explained in chapter 5.4.3. The shape of the oscillations is nearly the same containing many frequency components with similar amplitudes. The simulated driveshaft torque obviously contains only one dominant frequency, all others are suppressed or missing. The Fast Fourier

Transformation (FFT) was applied to the signals. The Hamming window was used in order to minimize the leakage. Due to the window definition, the shown amplitudes are half to real. The transformation was always applied to two sections of signal with a time period of 3 s in order to get the resolution of frequency 0.33 Hz to well cover the combustion frequency ( $N_e = 1250 \text{ rpm} \approx f_{comb} = 41.67 \text{ Hz}$ ). The values from these two sections were averaged. In the measurement, the frequency around 9 Hz was identified as the driveshaft natural frequency, frequency around 16 Hz was identified as the natural frequency of the powertrain mounts. Frequency around 21 Hz is the frequency of reciprocating mass of engine. The 1<sup>st</sup> order of combustion frequency is clearly dominant. The amplitude is almost identical for the left- and right-hand driveshaft torque signals ( $A_{DS\ LH}^{Hammm} = 1.04 \text{ Nm}$ ,  $A_{DS\ RH}^{Hammm} = 1.01 \text{ Nm}$ ). In the simulation data, the amplitude is much smaller ( $A_{DS\ sim}^{Hammm} = 0.24 \text{ Nm}$ ). The following plots show the driveshaft torque oscillation levels at the 1<sup>st</sup> order of combustion frequency for all six selected cases from the FFT analysis. Two cases for the same engine speed  $N_e$  are always plotted in one figure. The circles represent the part load cases (1, 6, 10) and the full dots the full load cases (2, 7, 12).

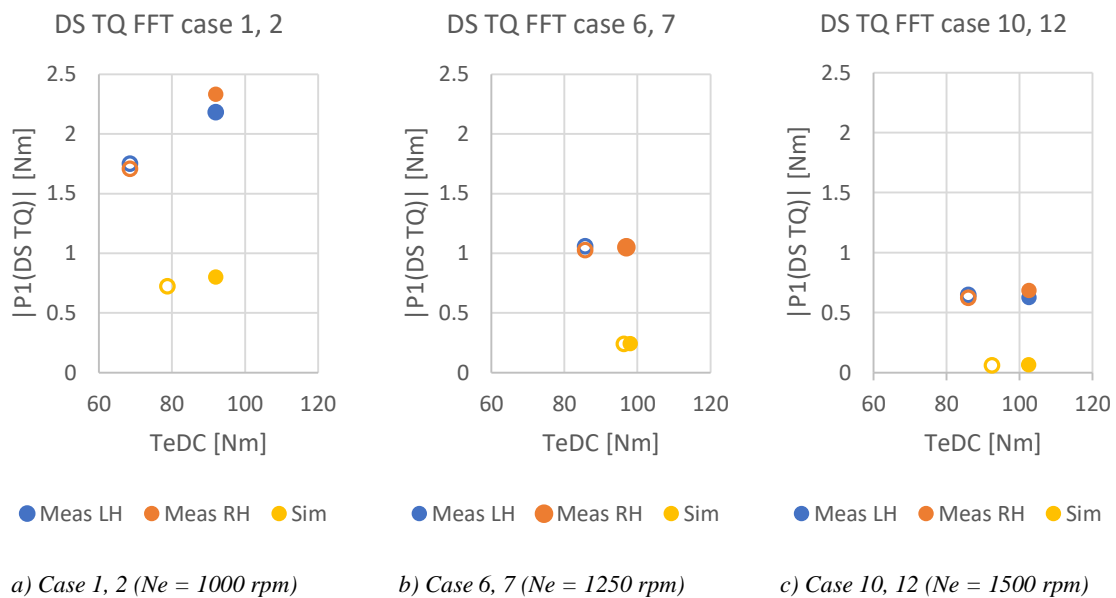


Figure 75 Driveshaft torque FFT results

At first, it can be seen in figure 75 that the prediction of engine torque  $TeDC$  is always higher in the part load cases. In case of the full engine load, the values of  $TeDC$  in the simulation and measurement equal each other. Especially in cases number 6 and 7 the difference between the part load and full load of  $TeDC$  is very small.

The levels of oscillations are obviously much lower in all the simulation results. With a higher engine speed the error in percent is higher (64.5 % for  $N_e = 1000 \text{ rpm}$  to 89.8 % for  $N_e = 1500 \text{ rpm}$  and full load case). This is a critical problem for the purpose of the toolchain model. Therefore, it was necessary to search for the root cause and possibly implement some improvements.



A more advanced tire model was one of the points which was assumed to improve the model in terms of powertrain dynamics level mainly from the reason that the origin of the dynamic properties of the tire model was unclear and could not be verified. The other concern was about TeAC logic, it was necessary to ensure the correct torque input into the system. The development and implementation of the improvements will be presented in the next chapter.

#### 5.6.4. Model improvements

##### Pacejka tire model [32]

Pneumatic tire plays an important role in the vehicle. It creates the contact between vehicle and road, damps its unevenness so it contributes to passenger's comfort. In vehicle dynamics modelling, appropriate tire model must be selected regarding the purpose. As an element with often the highest rotating inertia in drivetrain and strong damping properties, it significantly influences the performance of the model. Many tire models have been developed, however the Pacejka tire model is the most used in automotive engineering. The first version was developed and published by Prof. Pacejka in 1989 [33]. Since that time, the model was modified and improved several times.

At first, the fundamentals of tire modelling will be shown in figure 76. Due to acceleration and braking of the wheel, the driving and braking forces are applied to the tire patch. Longitudinal forces are developed in the tire-road contact zone due to the difference in circumferential  $V_r$  in point S and forward velocity of the wheel  $V_x$ . The difference between these velocities is called the slip velocity of the wheel  $V_{sx}$ . The slip  $\kappa$  of the wheel is defined as the ratio of the slip velocity and the longitudinal speed of the wheel center (29).

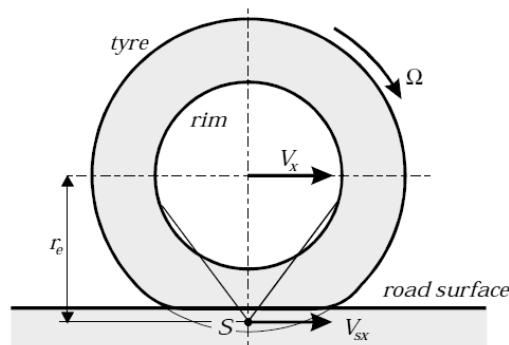


Figure 76 Kinematics of rolling [32]

$$\kappa = -\frac{V_{sx}}{V_x} = -\frac{V_x - V_r}{V_x} = -\frac{V_x - \Omega \cdot r_e}{V_x} \quad [m \cdot s^{-1}, rad \cdot s^{-1}] \quad (29)$$

The highest values of slip occur normally during harsh acceleration or braking. In a case of small value of slip, the longitudinal force  $F_x$  acting in point S can be represented as:

$$F_x = C_\kappa \cdot \kappa \quad [N] \quad (30)$$

where  $C_\kappa$  is linear coefficient known as slip stiffness.

Nevertheless, the linear part of tire stiffness is usually overcome, and the driving force usually decreases after reaching the peak value. Therefore, a more complex model must be determined. A stationary longitudinal slip characteristic can be seen in figure 77.

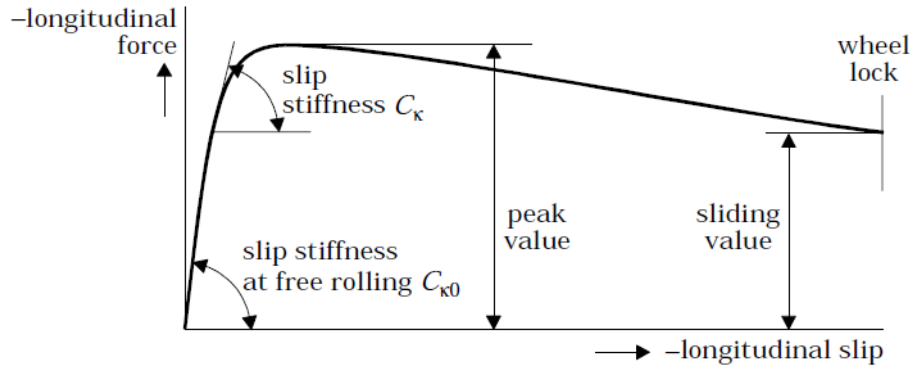


Figure 77 Typical stationary longitudinal slip characteristic. [32]

### Brush model

The brush model (figure 78) will be introduced first. It is a simple physical model, which allows analytical solution. It is an idealized representation of contact between tire and surface. The tire tread band is assumed to deform under vertical load. On the band, there are deformable cylinders attached – tread elements. When unloaded, they are assumed to be in radial direction of the belt. When coming to the contact, they start to deform due to the slip. The highest deformation comes when the blade travels along the contact patch in relative motion to wheel center. The length of the patch is called the contact length ( $l_c = 2 \cdot a$ ).

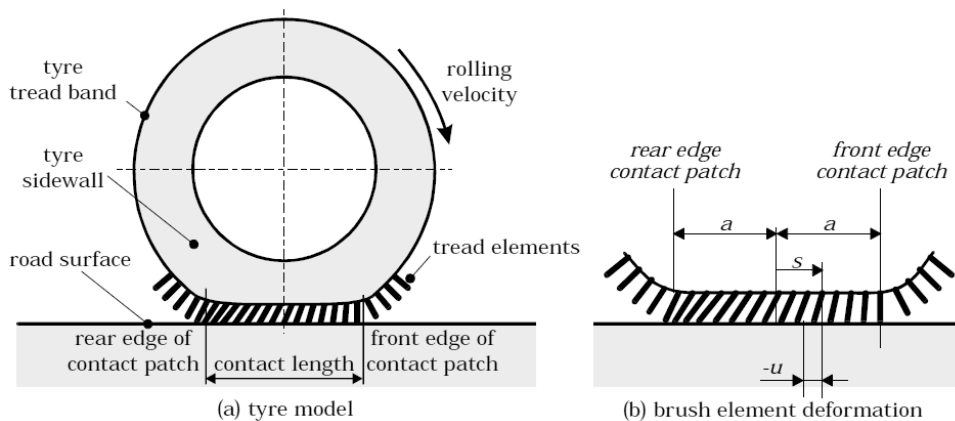


Figure 78 Tread elements attached to the tire tread band [32]

In the contact region the longitudinal deformation  $u$ , in distance  $s$  from point  $S$  in the contact patch, is directly related to the longitudinal slip. It can be expressed as:

$$u = (a - s) \cdot \frac{\kappa}{1 + \kappa} = -(a - s) \frac{V_{sx}}{V_r} [m, m \cdot s^{-1}] \quad (31)$$

After introducing the stiffness  $c_{cp}$  of tread elements per unit of length, the relation of driving force  $F_x$  can be expressed as:

$$F_x = c_{cp} \int_{-a}^a u(s) dx = 2 \cdot c_{cp} \cdot a^2 \cdot \kappa [N, N \cdot m^{-1}, m] \quad (32)$$

### Magic Formula model

The magic formula model is an empirical tire model. Its mathematical expression is based on measured tire data but also detailed finite element method model can be used for determination. The original formula of slip in Magic Formula was a combination of physical brush model and empirical data. The most recent version of Magic Formula slip relies only on measured data. [19]

$$F_x = D \sin\{C \operatorname{atan}[Bx + E(\operatorname{atan}((Bx) + Bx))]\} + S_V \quad (33)$$

where	$F_x$	-	Longitudinal force
	$x$	-	$x = \kappa + S_H$
	$B$	-	Stiffness factor
	$C$	-	Shape factor
	$D$	-	Peak factor
	$E$	-	Curvature factor
	$\kappa$	-	Longitudinal slip
	$S_H$	-	Horizontal shift
	$S_V$	-	Vertical shift

This model allows a precise description of the longitudinal force on the contact patch. Each factor is expressed by several more coefficients as can be found in [32]. According to a study case in [32], the Magic Formula model provides better results than the brush model, which includes a lot of simplifications.

The latest Pacejka tire model including the Magic Formula was implemented into the powertrain tire model as shown in figure 79. The parameters for corresponding tire were set from data sheet provided by tire supplier. However, Pacejka tire model allows the speed dependent calculation of tire radius, it was set as a constant. Rolling resistance, which is included in LMS Amesim tire model, was disabled since this loss is covered by road load function in SiL. A special element allowing to sense the tire longitudinal force  $F_x$ , which is sent to SiL instead of driving torque in LMS Amesim. This element was custom made by LMS Amesim supplier on request of this work. The vehicle mass (converted to vertical tire load acting on wheel) and wheel speed (converted to vehicle speed) were imposed from SiL.

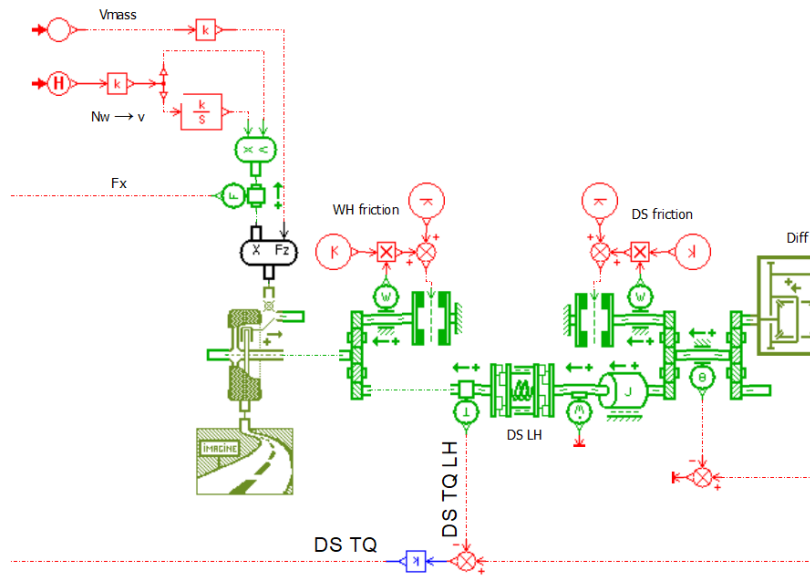


Figure 79 Implementation of Pacejka tire model

At the same time, another tire model was developed internally in Toyota (figure 80). This model is fairly simplified from the Pacejka model. It comprises of translational spring and damper as a representation of the contact patch situation. The stiffness and damping in longitudinal direction come from the same parametric sheet as for the full Pacejka model.

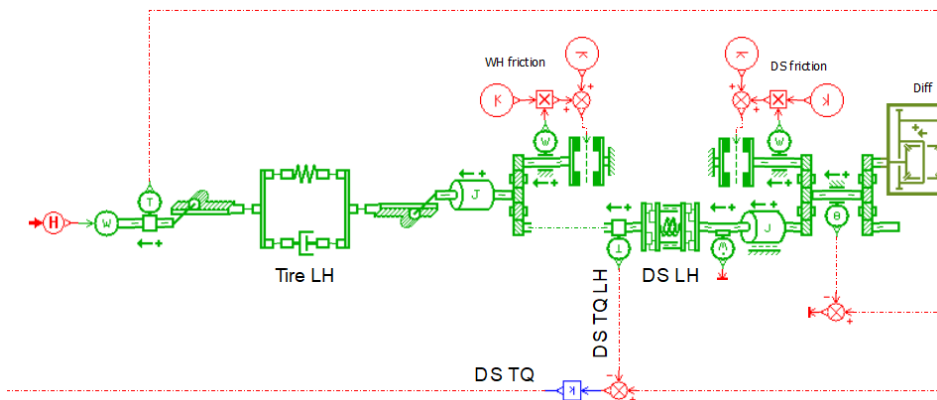


Figure 80 Implementation of simplified Pacejka tire model

Both models were tested, and they gave practically the same results. The simpler model was decided to be continued with. Firstly, it doesn't require a special LMS Amesim library, and it is easier to modify and calibrate it if needed. Unfortunately, neither of them brought any significant improvement to the model. Any other frequencies than the frequency of combustion was present. The targeted driveshaft torque oscillations of the combustion frequency were at approximately the same level as with the original tire model.

## TeAC logic

The powertrain model was subjected to a complex analysis. Torque and speed profiles of all parts were plotted. The first source of error was found in the engine block input torque.

The torque oscillations coming from the TeAC logic, as described in chapter 4.2.1., represent the torque of combustion forces acting on the crankshaft. Flywheel torque, which was measured by the flywheel torque sensor, as described in chapter 5.1., represents the torque on the input to the flywheel. The equivalent simulated flywheel torque for a direct comparison with the measured torque was determined using the calculation presented below in figure 81 and equation (34):

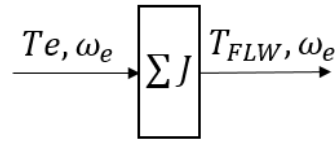


Figure 81 Flywheel torque calculation

$$T_{FLW} = Te - \Sigma J \cdot \alpha_{crksh} \quad [Nm, kg \cdot m^2, rad \cdot s^{-2}] \quad (34)$$

$$\Sigma J = J_{crksh} + J_{crod} + J_{pull} \quad [kg \cdot m^2] \quad (35)$$

$$\alpha_{crksh} = \frac{d\omega_{crksh}}{dt} = \frac{d\omega_e}{dt} \quad [rad \cdot s^{-2}, rad \cdot s^{-1}] \quad (36)$$

where  $T_{FLW}$  is calculated input torque to flywheel,  $J_{crksh}$  is moment of inertia of crankshaft,  $J_{crod}$  is moment of inertia of con rod,  $J_{pull}$  is moment of inertia of engine pulley,  $\alpha_{crksh}$  is rotational acceleration of crankshaft,  $\omega_{crksh}$  is speed of crankshaft and  $\omega_e$  is engine speed.

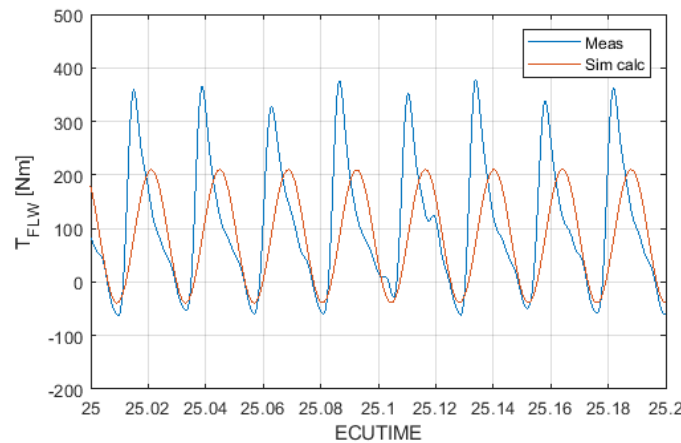


Figure 82 Flywheel torque  $T_{FLW}$  comparison

As can be seen in figure 82, the torque oscillations of flywheel torque are significantly lower in the simulation. The dynamic torque output of engine model in simulation is idealized into a pure sine wave pattern while the shape corresponds to the shape of combustion pressure in the measurement. The peak to peak values  $\Delta_{max-min}T_{FLW}$  (average over four oscillations – four cylinders firing) are compared in the following figure 83.

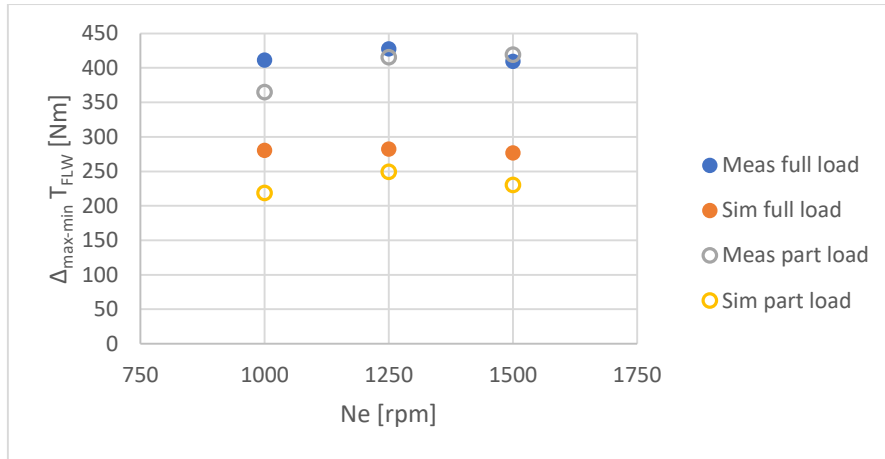


Figure 83 Flywheel torque oscillations, peak to peak values

The difference is always higher for the part load cases. The highest error is for the part load case at  $Ne = 1500 \text{ rpm}$  – peak to peak value is 54.9 % of the one measured. The lowest for the full load case at  $Ne = 1000 \text{ rpm}$  – 68.2 % of the one measured. Nevertheless, this improvement covered only a part of the difference between the simulation and measurement results.

As the first step of improvement, the peak to peak values of flywheel torque were brought to the level of measurement for each case by increasing the fluctuations of  $TeAC$ . The effect on the driveshaft torque oscillations amplitude was nearly proportional. When the  $TeAC$  level was increased by 50 % in relation to the original value, the driveshaft torque oscillations amplitude increased by 50 % in simulation, too.

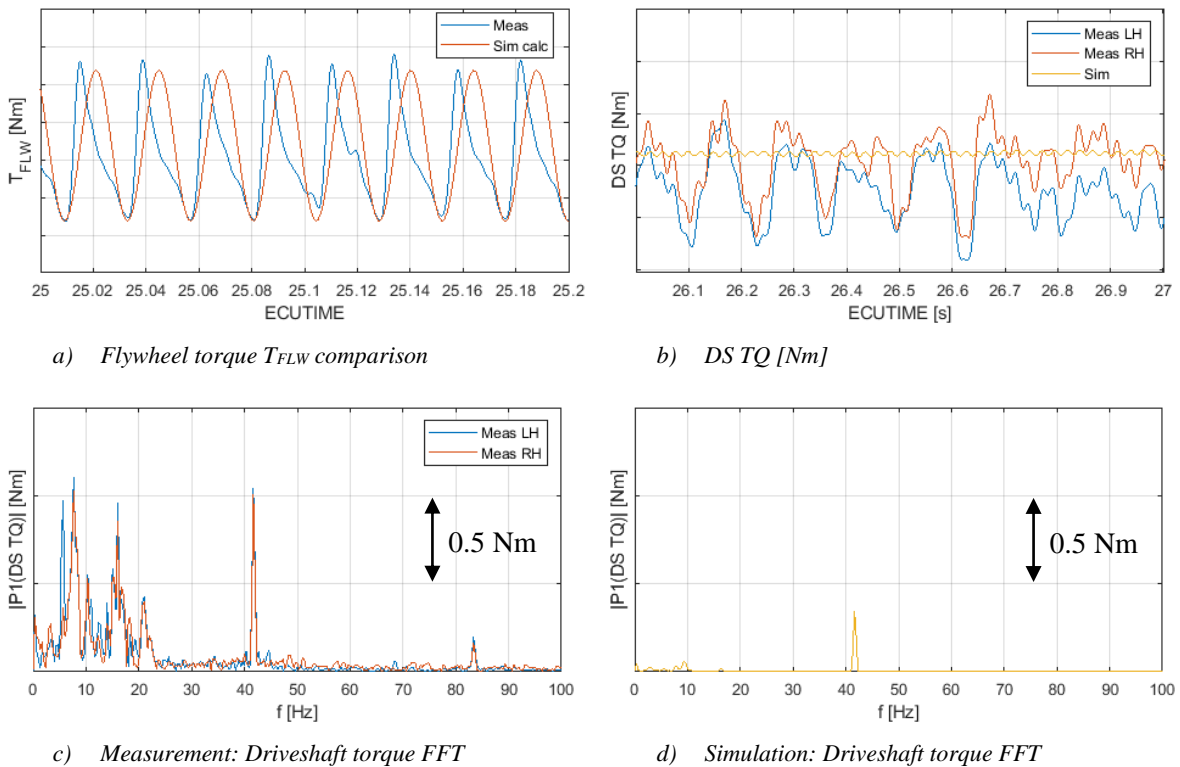


Figure 84 TeAC logic improvement results

This improvement, shown in figure 84, does not fully cover the gap in the driveshaft torque oscillations amplitude. Proposals for further improvements will be discussed in chapter 6.2.

### Drivetrain model investigation

Another issue was found in the drivetrain model. The low level of driveshaft torque oscillations seemed to have a cause in the counter driven gear model. In this summing junction, torque from the counter drive gear (engine and MG1) and reduction gear (MG2) sum up to the output counter driven gear torque, which is equal to countershaft torque since the gear is a part of countershaft. The countershaft torque oscillations in figure 85 b) correspond to driveshaft torque oscillations as there is no flexible element in the path until the driveshaft models. Junction distributes the speed coming from countershaft to the reduction and counter drive gears.

$$T_o = T_{p_{codrn}} + T_{m_{codrn}} = T_p \cdot i_{codr} + T_m \cdot i_{red} \quad (37)$$

$$N_o = N_{p_{codrn}} = N_{m_{codrn}} = \frac{N_p}{i_{codr}} = \frac{N_m}{i_{red}} \quad (38)$$

where  $T_o$  is countershaft torque,  $T_p$  is propeller shaft torque,  $i_{codr}$  is the counter gear ratio,  $T_m$  is MG2 torque,  $i_{red}$  is reduction gear ratio,  $N_o$  is countershaft rotational speed,  $N_p$  is propeller shaft rotational speed and  $N_m$  is MG2 rotational speed.

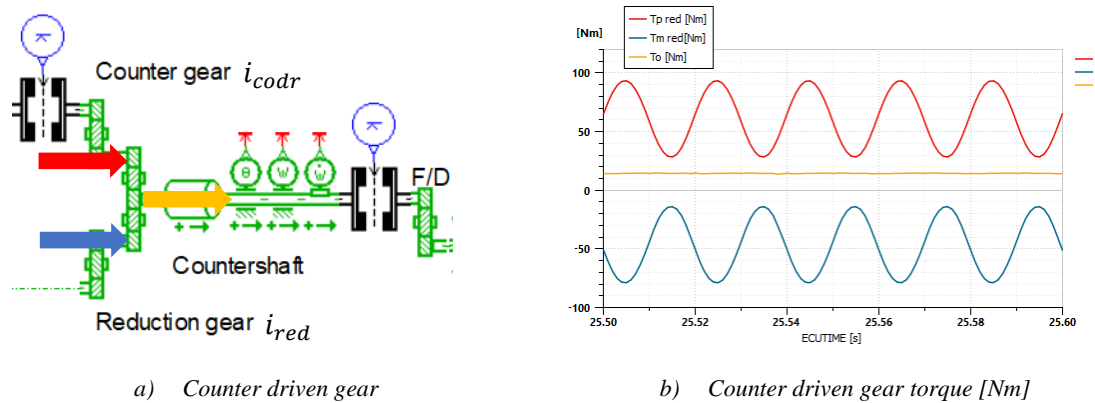
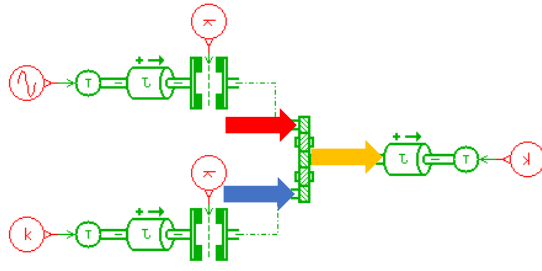


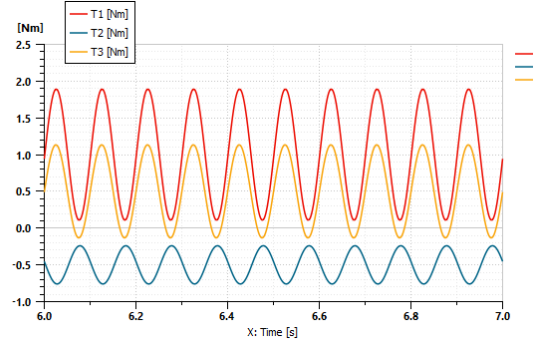
Figure 85 Counter driven gear model a) and the torque summation b)

When plotted, it is obvious that the dynamic torque from the propeller shaft (from engine and MG1 path, respectively – red line) is cancelled by MG2 torque oscillations (MG2 path – blue line) of almost the same, but opposite amplitude. As a result, the countershaft torque oscillations are very low. This behaviour of MG2 torque was a big concern because the synchronous electric motor (MG2) with a high number of poles usually provides a smooth torque output.

A simple standalone model (in figure 86 a)) expressing this situation was built in LMS Amesim. The values of moments of inertias and torques are random. The only fluctuating torque signal comes from the upper left element. The other two constant inputs (the right and bottom left) ensure the steady state.



a) Simple powertrain model



b) Summing junction torque [Nm]

Figure 86 Simple standalone model of the situation a) and its results b)

The same effect (in different ratios) can be seen in the results of the summing junction in figure 86 b). Based on these results, it can be assumed that this behaviour is physical. The idea behind is following the dynamic modelling strategy. The model works with the conservation laws. Therefore, torque and speed are always in phase shift of  $\pi/2$  (sinus and cosines) in order to satisfy the stability.

$$T(t) = T_0 \cdot \sin(t) \quad [Nm] \quad (39)$$

$$\alpha = \frac{T}{J} = \frac{T_0 \cdot \sin(t)}{J} \quad [rad \cdot s^{-2}, Nm, kg \cdot m^2] \quad (40)$$

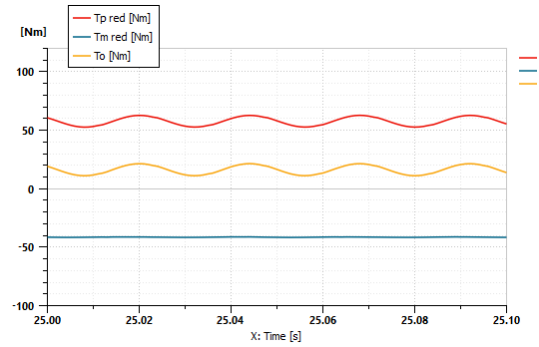
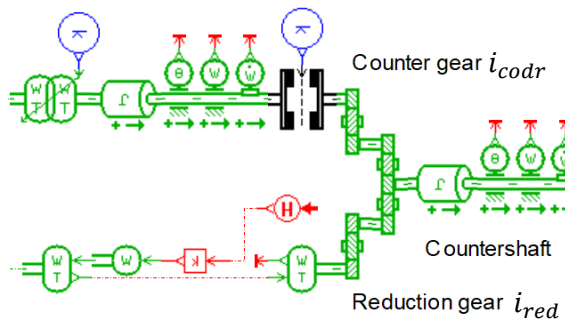
$$\omega = \int \alpha dt = \frac{1}{J} \int T_0 \cdot \sin(t) dt = -\frac{T_0}{J} \cos(t) [rad \cdot s^{-1}] \quad (41)$$

where  $T$  is torque,  $T_0$  amplitude of torque,  $t$  is time variable,  $\alpha$  is rotational acceleration,  $J$  is moment of inertia and  $\omega$  is the rotational speed.

The oscillating torque from the engine path (red) propagates through the drivetrain until the end (tire model), and the torque oscillations are compensated in inertia by speed oscillations (constant value is imposed on the other port), hence the first phase shift by  $\pi/2$ . The speed oscillations propagate back through the model to the summing junction where the signal is transferred to MG2 and engine paths via gear ratios (38). After entering the MG2 path the same principle of calculation of torque is applied. Hence another phase shift in MG2 path torque by  $\pi/2$ ,  $\pi$  in total to the engine path torque. When the torques sum up in the summing junction, the final amplitude of the output torque is lower.

This means, when the speed fluctuations entering MG2 inertia are lower, the torque fluctuations from the MG2 path are lower, too. Therefore, the final driveshaft torque oscillations are higher. This was proven when a non-oscillating MG2 speed was imposed to the MG2 path instead of the speed from the summing junction. Then the MG2 torque was also non-oscillating and the final torque at junction output or driveshafts was following the oscillations originated by engine. The situation is shown in figure 87. But the driveshaft torque oscillations in simulation were higher by order in this case. It means, that the speed oscillations in MG2 path need to be partly damped.





a) Imposed non-oscillating MG2 speed

b) Counter driven gear torque [Nm]

Figure 87 Counter driven gear model a) and the torque summation with non-oscillating Nm b)

Also, other possible improvements in terms of modelling were considered. For example, the countershaft could be modelled with dynamic properties, but the values of stiffness and damping were unknown. The next steps were focused on two spots in the model with the lowest stiffness – HV damper and driveshafts models. These two models were examined separately.

### HV damper model

The HV damper model is a relatively simple model with a spring, damper and a friction element representing the hysteresis. A more advanced HV damper model with backlash and stoppers models was considered to be implemented. But due to operational conditions of the booming noise (steady load not exceeding the limit displacement/torque point of the area of stiffness  $k_1$  in figure 88), it wouldn't bring any significant improvement. In the original model, spring stiffness and hysteresis were known from the drawing of the component. The value of the damping rate had no reference, it was given by the calculation as other components as described in chapter 4.2.1. The values of damping were relatively low in comparison to the damping rates of other elements. The value of the HV damper damping rate was subjected to the investigation.

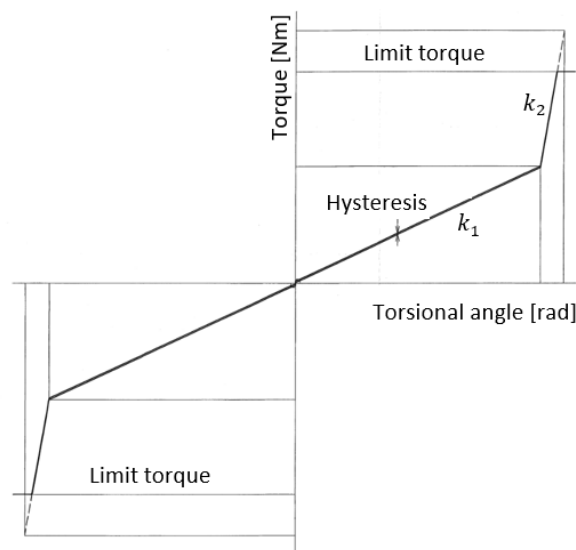


Figure 88 Typical HV damper characteristic

The investigation showed relatively high sensitivity, so that with increasing value of damping rate, the engine torque oscillations transfer through the HV damper model from engine increases, too, following the formula  $T = c_{HV} \cdot \omega$ , where  $T$  is torque,  $c_{HV}$  is damping rate of HV damper and  $\omega$  is rotational speed. Consequently, the torque oscillations from the MG2 path increase, too, as described in the chapter above. But due to dynamic properties of the drivetrain parts, this increase is lower. Therefore, the torque oscillations after the summing junction and hence on driveshafts are higher.

Calibration of the model was performed by varying the HV damper damping rate in a dedicated LMS Amesim standalone model derived from the latest version. This approach was chosen from the reason of incorrect prediction of the absolute level of engine torque  $TeDC$  in the toolchain model and shorter computational time. The boundary conditions ( $TeDC$ ,  $Tg$ ,  $Tm$ ,  $Nw$ ,  $Ne$ ) were imposed directly from the measurement. As a result, the optimal value of damping rate should be found in order to match the driveshaft torque oscillations amplitude with the results from the measurement. This study showed, that this parameter is strongly dependent on the combustion frequency, engine speed, respectively. Therefore, for every engine speed in the experiment, the value of damping rate for HV damper was tuned in the part load case first and this value was verified by the full load case. Then the final verification of all part load and full load cases was done using the toolchain model. No other frequencies than combustion frequency appeared in the driveshaft torque results as can be seen in the results from FFT analysis of case number 6 in figure 89.

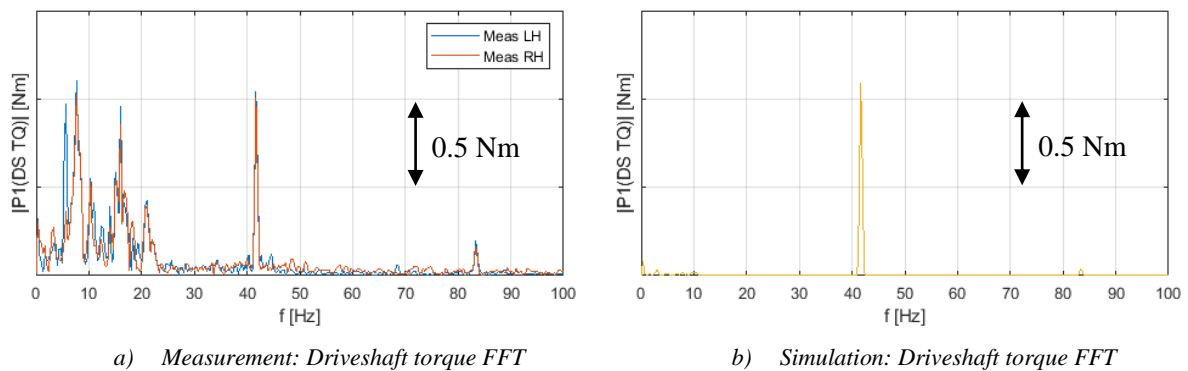
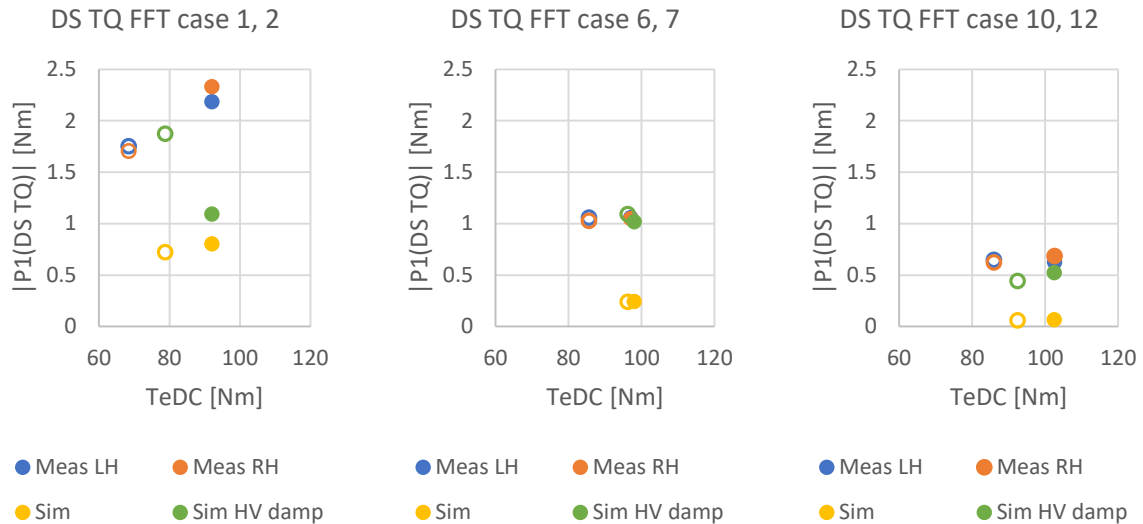


Figure 89 Driveshaft torque FFT after HV damper model calibration of case 6

The results from FFT of the 1<sup>st</sup> order of the combustion frequency amplitudes of all selected cases are shown in the following figure 90, which is based on figure 75. The blue and orange points represent the results from the measurement, yellow points the values from the initial high frequency validation model. The results from the HV damper model calibration are added as the green points. The circles represent the part load cases (1, 6, 10) and the full dots the full load cases (2, 7, 12).



a) Case 1, 2 ( $N_e = 1000 \text{ rpm}$ )      b) Case 6, 7 ( $N_e = 1250 \text{ rpm}$ )      c) Case 10, 12 ( $N_e = 1500 \text{ rpm}$ )

Figure 90 Results after HV damper model calibration

Firstly, it can be seen, that the absolute engine torque  $TeDC$  did not change, e.g. the powertrain model dynamics do not have an impact on the top-level data. The matching of values of driveshaft torque amplitude of the combustion frequency from the FFT analysis differs throughout the cases. The results of cases 1, 6, 7 and 12 match the targeted driveshaft torque oscillation with a high precision. The two remaining cases 2 and 10 have the levels of oscillations significantly lower. The reason was found again in the torque summing junction.

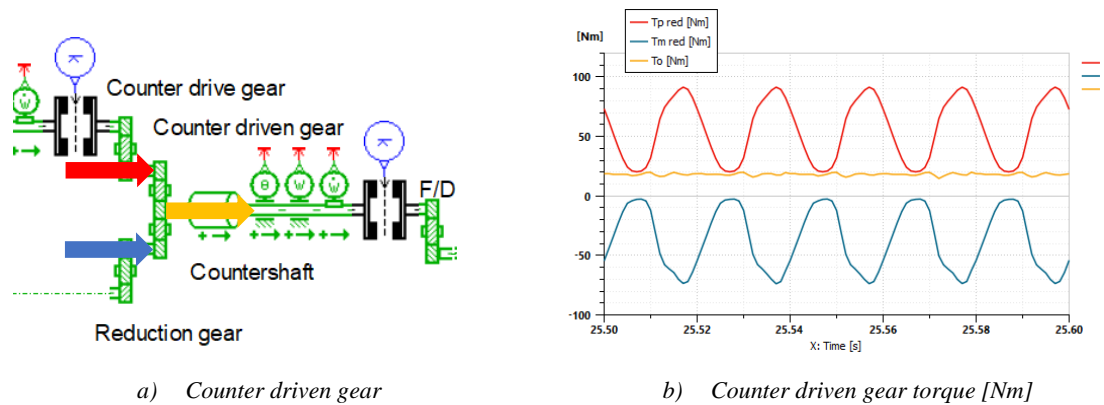


Figure 91 Counter driven gear model a) and the torque summation after model calibration b)

Because the torque coming from the MG2 path approaches zero values, the backlash models in MG2 path are activated and do not allow to cross the zero torque level from the reason of detaching the gear contact of the reduction gear. The final torque signal  $To$  is corrupted as shown in figure 91. In reality, this situation is usually followed by the rattle noise as described in chapter 3.3.3. HV control logic tries to avoid this situation as can be seen in figure 73 f) at  $t = 14 \text{ s}$  when the zero-torque level is quickly overcome. The rattle noise was not audible during measurement and is not expected to happen under the booming noise conditions. Therefore, this behaviour can be evaluated as non-realistic and strongly limits this method of the model improvement.

## Driveshaft model

The other subjected parameter was the driveshaft damping rate. The value was determined by a formula (25) based on driveshaft stiffness. This value was also sensitive to the changes, so it allowed the model to be further calibrated and the accuracy improved. The same approach and the same standalone model were used with the same boundary conditions as before. The part load case was used for calibration of the driveshaft damping rate in order to reach the same level of driveshaft torque oscillations. The full load case was used for validation. Due to the higher driveshaft damping rate, the speed oscillations propagating through drivetrain were suppressed and hence the MG2 path torque oscillations, too. Other frequencies in the driveshaft torque signal did not appear in this case in the simulation either, as it can be seen in the results of case 6 in figure 93.

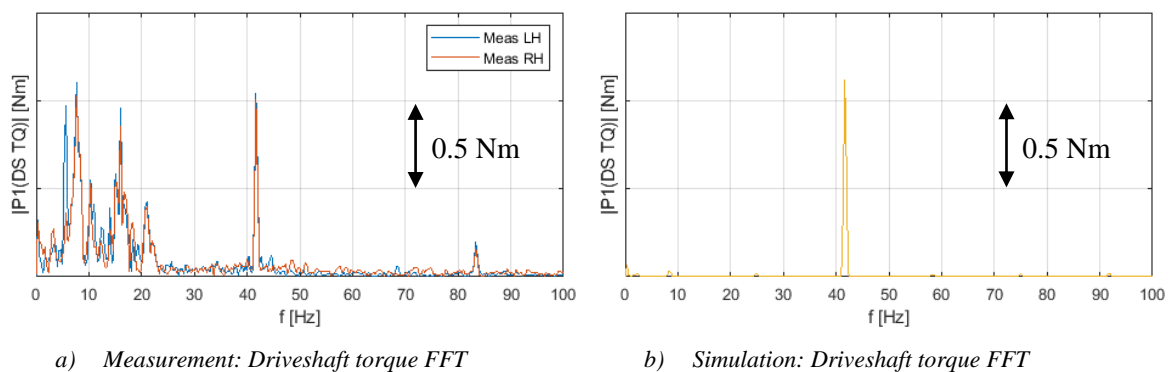


Figure 92 Driveshaft torque FFT after driveshaft model calibration of case 6

Nevertheless, the values of the optimal driveshaft damping values are relatively high, the amplitude of combustion frequency of the driveshaft torque from the simulation reaches the level as in the measurement. The optimal values were again found as dependent on the combustion frequency, engine speed, respectively. The results can be seen in the following figure 92 as the red points. The circles represent the part load cases (1, 6, 10) and the full dots the full load cases (2, 7, 12).

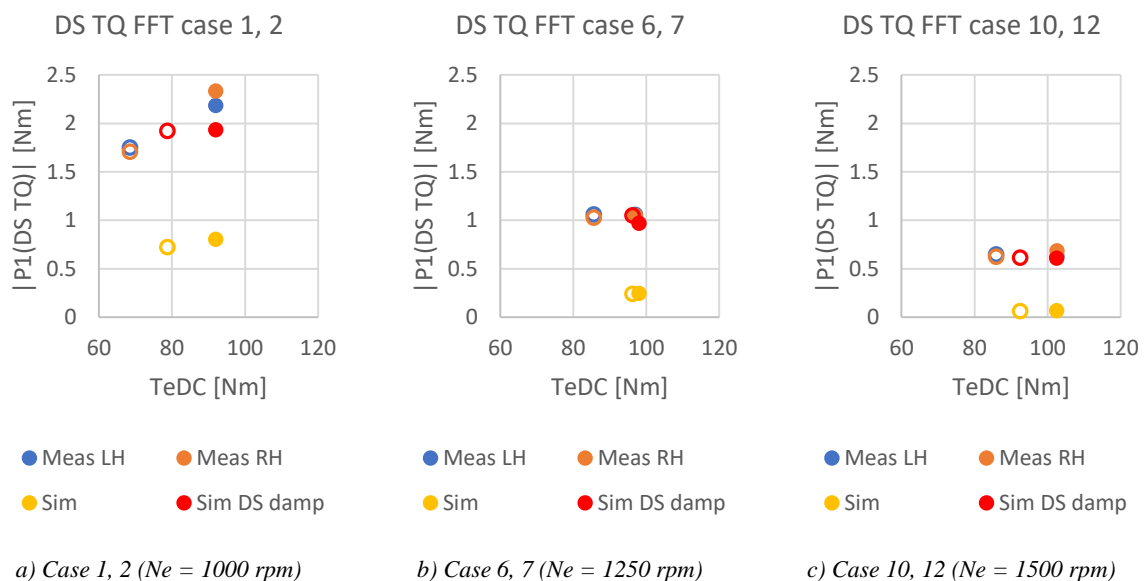


Figure 93 Results after driveshaft model calibration

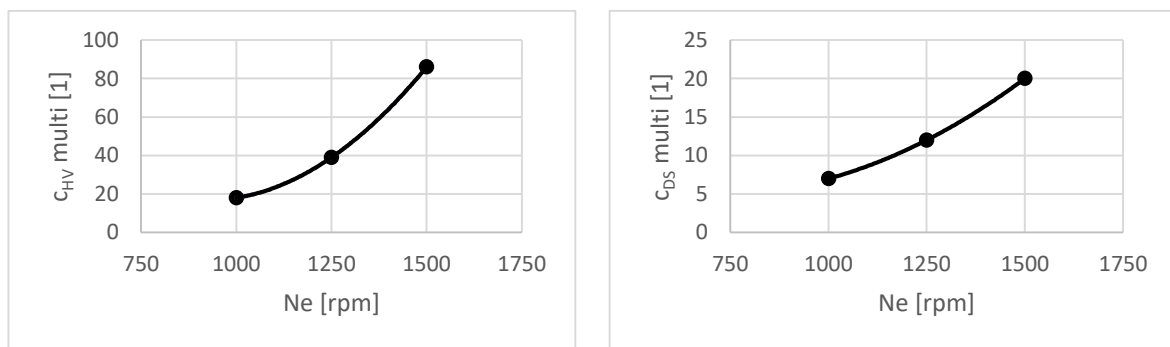
### 5.6.5. Summary

Also in this validation step, the driving scenarios were proposed first, measured with the test vehicle and replicated in the toolchain model. In the beginning, the level of simulated drivetrain dynamics was very low. It is obvious in table 15 where the relative error of the initial model when the FFT of the driveshaft torque signal was performed and the amplitude of the 1<sup>st</sup> order of the combustion frequency was compared with averaged measured values. The results for all cases of all improvements are shown in attachments.

Table 15 Relative error of the 1<sup>st</sup> order combustion frequency amplitude of driveshaft torque for initial and improved models

Model	Relative error [%]					
	$Ne = 1000 \text{ rpm}$		$Ne = 1250 \text{ rpm}$		$Ne = 1500 \text{ rpm}$	
	Case 1	Case 2	Case 6	Case 7	Case 10	Case 12
Initial model	58.3	64.5	76.9	76.7	90.6	89.8
TeAC logic	35.3	44.5	46.6	51.1	50.3	59.9
HV damper	8.3	51.6	4.9	3.3	30.5	20.1
Driveshafts	11.1	14.4	7.3	0.2	3.2	7.3

The relative error was decreased in relation to the model with initial model by several improvements. The improved TeAC logic calculation significantly decreased the error but the relative error remains still high. Further improvement was brought by calibration of HV damper and driveshafts models. These methods decreased the relative error to acceptable level in most of the cases. The method of changing the HV damper damping rate has a limitation as described above, effecting results of case 2, 10 and 12. It is necessary to mention, that the last two improvements are countermeasures in order to match the targeted signal properties. They do not follow any formula or rule, the values were calibrated for the model in order to match the results. The dependencies as the multipliers of the original values of the HV damper and driveshaft damping rates on engine speed are shown in figure 94.



a) HV damper damping rate multiplier

b) Driveshaft damping rate multiplier

Figure 94 Optimal values of multiplier of HV damper a) and driveshaft b) damping rates

Verification of each of them would require additional advanced instrumentation and measurement on a test vehicle or a dedicated test bench which was not available for this work. The effect of the modified damping rates was shown for each element separately but, it is highly possible, that the solution would be a combination of both and further model calibration would be needed.

## **6. Model accuracy improvements**

In this chapter the model accuracy improvements will be described. Some of them were already implemented to the toolchain model and will be summarized now. But there is still a lot of potential improvements which were identified and will be proposed hereafter. They can be divided to three groups – whether they are applied to the SiL, powertrain model or on the co-simulation level.

### **6.1.SiL model improvements**

Apart from the necessary modifications applied during the toolchain development, no other improvements were applied to the SiL model. Nevertheless, some improvements must be done in the future. It should be focused on the improvement of loss modelling in plant model of the electrical branch of the powertrain. The inaccuracy caused inexact prediction of engine and MG1 torque and power in case number 4 in top-level validation in figure 53 and all part load validation cases in high frequency validation in chapter 5.6.3. where this phenomenon is pronounced the most. The loss maps of MG1, MG2, battery, AC/DC inverter and boost converter should be verified and potentially corrected as it was partly proposed in chapter 5.3.3.

Another non-accuracy related improvement was made in the SiL model. The calibration map responsible for the booming noise avoidance was extracted from HV-ECU code to the canvas in Simulink so it can be easily modified. It is ready for a possible connection to an optimization tool for a calibration process in the future.

### **6.2.Powertrain model improvements**

In the powertrain model, several improvements were already performed. The end of powertrain (driveshafts and tires) was originally lumped to a single model, so it was split into left- and right-hand scheme as described in chapter 5.4.4. It gave the possibility to implement other more advanced models. The countershaft inertia model was moved to a more appropriate position.

As the next step, the torque signal response from powertrain model to SiL was modified. The new configuration downstream to tire better represents the driving force for a dynamic simulation as described in chapter 5.4.3.

Pacejka tire model is a common tire model in the vehicle dynamics modelling. It was implemented during the high frequency validation process. At the same time another tire model was derived from the full Pacejka tire model. The difference in results was minimal so the simpler model derivative was chosen for the powertrain model.

The HV damper and driveshaft damping rates were calibrated in order to match the dynamic performance of the model in chapter 5.6.4. These two approaches represent the possible ways of the

improvement of the toolchain model so that it can be used for the booming noise prediction and later for the model-based calibration process.

The dynamic engine torque calculation was improved at least in terms of the magnitude of the oscillations, however the idealised sinus shape of the engine torque signal does not correspond to the reality. This is most likely the reason why only the first order of combustion frequency can be seen in the results. In reality, it contains other orders for drivetrain excitation. One solution would be to update the TeAC map by measurement of cylinder pressure levels for different engine speed and load. In order to avoid complex and costly measurement, it can be more convenient to use 1-D CAE model of the engine to reproduce the cycling torque related to combustion. Also, the shape of engine torque fluctuations should be more realistic and improved by an advanced logic to include the other orders in the signal. Another solution would be to connect the engine 1-D CAE model to the toolchain and create a co-simulation of three models. The last solution would be to impose directly the measured flywheel torque the engine path. This solution would need a usage of a different engine block model in the powertrain model. It also loses a part of the prediction ability.

For a deep root cause analysis, the dynamic properties of all parts in powertrain should be revised based on measurement or results of 3-D CAD models. The missing dynamic properties of some parts (e.g. MG1 shaft, propeller shaft, countershaft) should be modelled. As the HV damper and driveshafts damping rates were calibrated, they should be subjected to deeper analysis.

Powertrain mount models can strongly influence the dynamic behaviour of the entire model. They have not been validated on highly dynamic base yet so the validation process should follow. Although their topology and parameters were identified, some inaccuracy may appear. It would give an indication for their calibration.

There are no mechanical losses covered in the powertrain model. They are mostly represented by  $A$  coefficient of the vehicle equation of motion (14) in SiL. This situation is not really suitable for the dynamic model as the damper and friction have the same function as a dissipater in the dynamic modelling [34]. As a further improvement, the main friction losses could be modelled in the powertrain model. From this reason, the friction elements for tire and damper were implemented in the model as in chapter 5.4.4.

### **6.3. Co-simulation level improvements**

One improvement was already proposed as a powertrain model improvement related to the co-simulation level – connecting engine 1-D CAE model for more precise dynamic engine torque prediction. In this case the biggest concern would be about increasing the computational time since the toolchain should be sufficiently fast for the purpose of the NV booming map calibration.

The other modification could consist in different signals transfer. In the current model, three torque signals are applied to the powertrain model ( $T_e, T_g, T_m$ ) and one speed signal ( $N_w$ ;  $N_e$  defines only the combustion frequency in the powertrain model). As an output three speed signals ( $N_e, N_g, N_m$ ) and one torque signal ( $T_w$ ) are sent to SiL. Directly imposed speed  $N_w$  can cause instability of the system under certain conditions as the speed source can be considered as an infinite torque source model so every difference in speed is covered by infinitely high torque and vice versa. From this reason, all powertrain model inputs should be remodelled to torque and outputs to speed as shown in the following figure. In this approach the powertrain model will output system speeds response as a result of applied torques to the system. The car model must be relocated to powertrain model in this case.

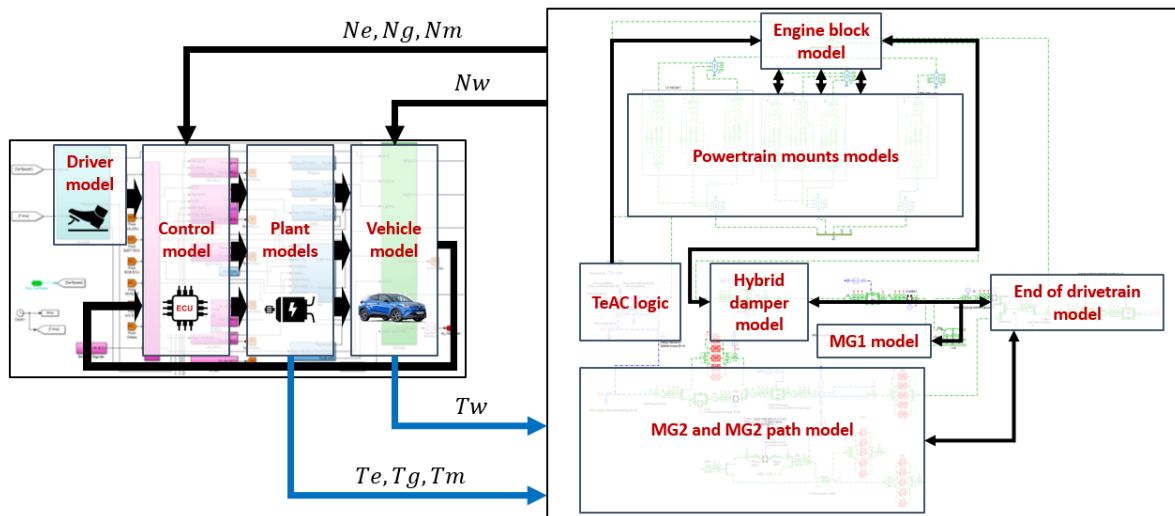


Figure 95 Proposed configuration of co-simulation



## 7. Conclusion

The scope of this work was to get familiar with the problems of NV in THS, develop a toolchain model for booming noise prediction, validate it based on data from measurement and identify the improvements to increase the toolchain accuracy. The suitable software environments were identified, and standalone models were built prior to this work.

Necessary changes were applied to the standalone models and they were successfully coupled into the toolchain. The SiL model in MATLAB Simulink has the master function and controls the detailed powertrain model in LMS Amesim which provides the speed response of plants to the applied torque signals from the control model. As the next step, the toolchain model was validated by test vehicle.

At first, the vehicle road load was measured as described in chapter 5.2., and the results were used as an input for the toolchain model. The top-level validation followed as described in chapter 5.3. Driving scenarios were proposed for the test vehicle, measured and replicated in simulation based on the same accelerator pedal input. Validation methodology was developed, and results compared. The tire radius was calibrated for the vehicle model so that the data match with measurement. Some limitations and inaccuracies were identified during the process and were described in this chapter. But in general, the toolchain model predicts the vehicle top-level behaviour with high accuracy.

In chapter 5.4. the low frequency validation was described. EV tip-in driving scenario was selected for this validation. Validation result proved the toolchain model did not contain the drivetrain low frequency phenomena, therefore the powertrain model had to be adjusted. Several improvements to the toolchain were implemented and some more proposed for future work. Finally, the targeted driveshaft torque oscillations were followed well in terms of frequency. The amplitude and absolute value were higher, but the accuracy was sufficient for this part of validation.

Powertrain block model was validated in quasi-static conditions under dynamic load in chapter 5.5. The model provided relatively accurate results using the selected methodology. Nevertheless, some more advanced measurement techniques and methodologies should be applied in future in order to capture the powertrain block dynamics, too.

The last validation step, high frequency validation, is described in chapter 5.6. The powertrain dynamics level in the model was low at first. A new tire model was derived from Pacejka tire model and implemented. Engine dynamic torque level was brought to the level as in measurement. Two ways of improvement by model calibration were shown so that the targeted combustion frequency oscillations match with the measurement data. No other frequencies appeared in the results yet, but several improvements were proposed. All the improvements applied to the model were summarized and several others proposed in chapter 6.

In general, the initial validation results have shown major issues of the toolchain model in terms of drivetrain dynamics prediction capability. Several toolchain improvements and modifications implemented within this work has greatly improved the toolchain accuracy. Some other improvement points and guidelines were suggested for future work.

## References

- [1] “Spain’s Booming Hybrid Electric Vehicle Market: A Summary of Supporting Policy Measures”. 2019. Online. The International Council on Clean Transportation. Available from: <https://theicct.org/>.
- [2] “Worldwide Sales of Toyota Hybrids Surpass 10 Million Units”. 2017. Online. Toyota Global Newsroom. Available from: <https://global.toyota/en>.
- [3] “Toyota Motor Europe Approaching Half a Million Sales of Self-Charging Hybrid Electric Vehicles in 2018”. 2019. Online. Toyota Europe Newsroom. Available from: <https://newsroom.toyota.eu/>.
- [4] “Toyota Hybrid Systems, THS-II: Next-generation hybrid technology”. 2011. Internal Toyota Motor Europe documentation.
- [5] McKay, Brian. 2016. “Benefits of A 48V P2 Mild Hybrid”. Online. Advanced Clean Cars Symposium: The Road Ahead. Available from: <https://ww2.arb.ca.gov>.
- [6] *Techdoc*, Internal Toyota Motor Europe documentation.
- [7] Heywood, John B. 1988. *Internal Combustion Engine Fundamentals*. New York: McGraw-Hill.
- [8] Chen, Kun-Ho, and Yei-Chin Chao. 2019. “Characterization of Performance of Short Stroke Engines with Valve Timing for Blended Bioethanol Internal Combustion”. *Energies* 12 (4). <https://doi.org/10.3390/en12040759>.
- [9] *Toyota Training Portal*, Internal Toyota Motor Europe documentation.
- [10] Miller, John M. 2004. *Propulsion Systems for Hybrid Vehicles*. Stevenage: Institution of Electrical Engineers.
- [11] “Introduction to Epicyclic Gear Train”. 2016. Online. Mechanical Engineering Project, Seminars, Basic Notes. Available from: <http://seminar1663.rssing.com>.
- [12] “Gen 3 PSD Question”. 2013. Online. Prius Chat. Available from: <https://priuschat.com>.
- [13] Toyota Hybrid System II. Internal Toyota Motor Europe documentation.
- [14] Genuit, Klaus. 2004. “The Sound Quality of Vehicle Interior Noise: A Challenge for The NVH-Engineers”. *International Journal of Vehicle Noise and Vibration* 1 (1/2). <https://doi.org/10.1504/IJVNV.2004.004079>.
- [15] Nobou Dassi, Martial, Arnaud Gaudin, Zouhir Abbadi, Laurent Gagliardini, Charles Pezerat, and François Gautier. 2015. “Analysis of the performances of automotive car bodies with different structural contrasts”. *11th International Conference on Engineering Vibration*. Ljubljana.
- [16] “In-Vehicle Powertrain Noise Evaluation”. 2017. Online. Bruel & Kjaer. Available from: [www.bksv.com](http://www.bksv.com).

- [17] Cinkraut, Jakub. 2015. "Transfer Path Analysis of a Passenger Car". Diploma thesis, Stockholm: KTH.
- [18] Gartmeier, Otto. 2014. *Vehicle Acoustics and Vibration - course compendium*. Stockholm: KTH.
- [19] Rahnejat, Homer. 2010. *Tribology and Dynamics of Engine and Powertrain: Fundamentals, Applications and Future Trends*. Woodhead Publishing in Mechanical Engineering. Philadelphia: Woodhead Pub.
- [20] Wellmann, Thomas, Kiran Govindswamy, Eugen Braun, and Klaus Wolff. 2007. "Aspects of Driveline Integration for Optimized Vehicle NVH Characteristics". *SAE 2007 Transactions Journal of Passenger Cars: Mechanical Systems-V116-6*. <https://doi.org/10.4271/2007-01-2246>.
- [21] Farshidianfar, Anooshiravan, Masoumeh Ebrahimi, and Homer Rahnejat. 2002. "High Frequency Torsional Vibration of Vehicular Driveline Systems in Clonk". *International Journal of Heavy Vehicle Systems* 9 (2). <https://doi.org/10.1504/IJHVS.2002.001173>.
- [22] Shangguan, Wen-Bin, Xue-Lai Liu, Yuming Yin, and Subhash Rakheja. 2018. "Modeling of Automotive Driveline System for Reducing Gear Rattles". *Journal of Sound and Vibration* 416: 136-153. <https://doi.org/10.1016/j.jsv.2017.07.052>.
- [23] Britto, John Vijay Antony, Sudipto Karmakar, Madhan Muthuveeraswamy, and Balasubramanian Natarajasundaram. 2016. "High Speed Booming Noise Reduction in Passenger Car by Application of Cost Optimized NVH Solution". *SAE Technical Paper Series*. <https://doi.org/10.4271/2016-28-0039>.
- [24] Lee, Youn-Hee, and Adel Nasiri. 2007. "Real Time Active Noise Control of Engine Booming in Passenger Vehicles". *SAE Technical Paper Series*. <https://doi.org/10.4271/2007-01-0411>.
- [25] Kang, Hyungsouk, TaeYoung Chung, Hyeongcheol Lee, and Hyungbin Ihm. 2016. "Active Booming Noise Control for Hybrid Vehicles". *SAE International Journal of Passenger Cars - Mechanical Systems* 9 (1): 167-173. <https://doi.org/10.4271/2016-01-1122>.
- [26] "What Is an S-Function?". Online. MathWorks Documentation. Available from: <https://nl.mathworks.com>.
- [27] Zaffiri, Francesco. 2018. "Development of an Engine Mounting System Model for NVH Phenomena Investigation". Diploma thesis, Modena: UNIMORE.
- [28] Berg, Mats. 2005. "A Model for Rubber Springs in The Dynamic Analysis of Rail Vehicles". *Proceedings of The Institution of Mechanical Engineers, Part F: Journal of Rail and Rapid Transit* 211 (2): 95-108. <https://doi.org/10.1243/0954409971530941>.
- [29] Preda, Ion, Dinu Covaciu, and Gheorghe Ciolan. 2011. "Coast Down Test – Theoretical and Experimental Approach". in *The Automobile and The Environment: International Congress of*

*Automotive and Transport Engineering Conat 2010*, 155. Newcastle upon Tyne: Cambridge Scholars Pub.

- [30] Anghelache, Gabriel, and Robert Moisescu. 2017. "The Measurement of Dynamic Radii for Passenger Car Tyre". *Iop Conference Series: Materials Science and Engineering 252* (October). <https://doi.org/10.1088/1757-899X/252/1/012014>.
- [31] LMS Amehelp, LMS Amesim help section
- [32] Zegelaar, Peter W.A. 1998. *The Dynamic Response of Tyres to Brake Torque Variations and Road Unevennesses*. Delft: Delft University of Technology.
- [33] Bakker, Egbert, Hans B. Pacejka, and Lars Lidner. 1989. "A New Tire Model with an Application in Vehicle Dynamics Studies". *SAE Technical Paper Series*. <https://doi.org/10.4271/890087>.
- [34] Wellstead, P. E. 1979. *Introduction to Physical System Modelling*. New York: Academic Press.

## List of abbreviations

A/C	Air-conditioning
A/C-ECU	Air-conditioning Electronic Control Unit
AC	Alternating Current
BAS	Belt Alternator Starter
BAT-ECU	Battery Electronic Control Unit
BDC	Bottom Dead Centre
BEV	Battery Electric Vehicle
CAD	Computer Aided Design
CAE	Computer Aided Engi--neering
CVT	Continuously Variable Transmission
DC	Direct Current
DS	Driveshaft
ECB-ECU	Brake Electronic Control Unit
ECU	Electronic Control Unit
e-CVT	Electronic Continuously Variable Transmission
EFI-ECU	Engine Electronic Control Unit
EGR	Exhaust Gas Recirculation
EU	European Union
EV	Electric Vehicle
FFT	Fast Fourier Transformation
FWD	Front Wheel Drive
GUI	Graphical User Interface
HEV	Hybrid Electric Vehicle
HSG	Hybrid Starter Generator
HV	Hybrid Vehicle
HV-ECU	Hybrid Vehicle Electronic Control Unit
MBC	Model-based Calibration
MBD	Model-based Design
MG-ECU	Motor Electronic Control Unit
MG1	Motor/Generator 1
MG2	Motor/Generator 2
NiMH	Nickel-Metal Hydrid
NV	Noise and Vibration

NVH	Noise, Vibration and Harshness
PC	Personal Computer
PCU	Power Control Unit
RWD	Rear Wheel Drive
SiL	Software in Loop
SOC	State of Charge
STD	Standard deviation
TeAC	Dynamic Engine Torque
TeDC	Non-oscillating Engine Torque
THS	Toyota Hybrid System
TMED	Transmission Mounted Electric Device
TopL	Top Left-hand
TopR	Top Right-hand
VVT	Variable Valve Timing

## List of figures

Figure 1 Market share of new HEV's in selected EU countries [1].....	9
Figure 2 Toyota hybrid vehicle global sales [2].....	10
Figure 3 Series hybrid layout [4] .....	13
Figure 4 Parallel hybrid layout [4].....	14
Figure 5 Location of electric motor in mild hybrid powertrain [5].....	15
Figure 6 Power-split hybrid layout [4].....	16
Figure 7 Scheme of THS Gen4 [6] .....	16
Figure 8 Otto and Atkinson cycles p-V (a) and T-s (b) diagrams [8].....	17
Figure 9 p-V diagram of Atkinson cycle in the conventional reciprocating engine [9].....	18
Figure 10 High voltage layout [9].....	19
Figure 11 HV damper [9].....	20
Figure 12 Planetary gear set [11] .....	21
Figure 13 Nomographic chart of vehicle taking off [12] .....	22
Figure 14 Nomographic chart of engine starting up [12].....	22
Figure 15 Nomographic chart of electricity generation during driving [12].....	23
Figure 16 Nomographic chart of electricity generation when vehicle stopped [13] .....	23
Figure 17 Comparison between THS and non-hybrid powertrain behaviour in a simple driving cycle [9] .....	24
Figure 18 Noise sources and transfer paths [16].....	25
Figure 19 Transition region between structure-borne and air-borne noise [18] .....	26
Figure 20 Structure-borne transfer path [18] .....	27
Figure 21 Typical frequency range of different powertrain NVH [20].....	28
Figure 22 Gear rattle origin [22] .....	29
Figure 23 Source-Path-Receiver scheme of booming noise [23].....	30
Figure 24 Acoustic and structural meshed models of the cabin [24] .....	32
Figure 25 Principle of in-cabin active noise control [24] .....	32
Figure 26 TMED parallel hybrid configuration [25] .....	33
Figure 27 Main principle of anti-phase torque reduction in drivetrain [25] .....	33
Figure 28 Engine operational point modification .....	34
Figure 29 Simplified SiL model scheme.....	36
Figure 30 Simplified powertrain model scheme .....	38
Figure 31 TeAC logic scheme .....	39
Figure 32 Engine torque signal composition in powertrain model .....	39
Figure 33 Right-hand powertrain mount model scheme.....	40
Figure 34 HV damper model scheme .....	40

Figure 35 MG1 model scheme.....	41
Figure 36 MG2 and MG2 path model scheme.....	41
Figure 37 End of drivetrain model scheme.....	42
Figure 38 Co-simulation modes SL2AME and SL2AMECosim.....	43
Figure 39 Co-simulation modes AME2SL and AME2SLCosim.....	43
Figure 40 Vehicle resistance calculation block in SiL model.....	45
Figure 41 Scheme of co-simulation.....	46
Figure 42 Driveshaft torque sensors calibration process.....	48
Figure 43 Flywheel torque measurement location.....	48
Figure 44 Powertrain top displacement sensors.....	49
Figure 45 Powertrain low displacement sensor.....	49
Figure 46 Vehicle equation of motion coefficients probability distribution of variant 1.....	52
Figure 47 Vehicle equation of motion coefficients probability distribution of variant 2.....	52
Figure 48 Initial results of the top-level validation of case 5.....	56
Figure 49 Equation of motion coefficients adjustment example for case 2.....	57
Figure 50 Vehicle equation of motion coefficients probability distribution of variant 1 with new tire radius.....	59
Figure 51 Vehicle equation of motion coefficients probability distribution of variant 2 with new tire radius.....	59
Figure 52 Final results of the top-level validation of case 3.....	60
Figure 53 Final results of the top-level validation of case 4.....	62
Figure 54 Final results of the top-level validation of case 5.....	64
Figure 55 Initial results of the low frequency validation case.....	68
Figure 56 Battery and MG2 power of the low frequency validation case.....	69
Figure 57 Driveshaft torque with separately undamped driveshaft a) and tire b).....	70
Figure 58 Evaluation parameters of the driveshaft damping sensitivity study.....	71
Figure 59 Results of the driveshaft damping sensitivity.....	72
Figure 60 New detailed drivetrain model.....	73
Figure 61 Results of the low frequency validation case.....	74
Figure 62 Targeted and estimated MG2 torque $T_m$ .....	75
Figure 63 Evaluation parameters of tire stiffness and damping rate sensitivity study.....	75
Figure 64 $r_{Amp}$ of tire stiffness and damping sensitivity study.....	76
Figure 65 Vehicle $R_1$ frame a), powertrain block $R_4$ and inertia $R_{inertia}$ frames b) [31].....	77
Figure 66 Powertrain block movement in respect to centre of gravity in simulation.....	78
Figure 67 Powertrain with stroke sensors and the torque roll axis.....	79
Figure 68 Course of powertrain block movement validation process.....	79
Figure 69 Powertrain block movement methodology.....	80



Figure 70 Points with zero velocity for the new axes of rotation .....	81
Figure 71 Course of the powertrain block movement validation process with a new torque roll axis .	81
Figure 72 Final stroke sensors displacement results .....	82
Figure 73 High frequency validation results of case 6.....	85
Figure 74 Driveshaft torque analysis of case 6 .....	86
Figure 75 Driveshaft torque FFT results.....	87
Figure 76 Kinematics of rolling [32] .....	88
Figure 77 Typical stationary longitudinal slip characteristic. [32] .....	89
Figure 78 Tread elements attached to the tire tread band [32].....	89
Figure 79 Implementation of Pacejka tire model .....	91
Figure 80 Implementation of simplified Pacejka tire model.....	91
Figure 81 Flywheel torque calculation.....	92
Figure 82 Flywheel torque $T_{FLW}$ comparison.....	92
Figure 83 Flywheel torque oscillations, peak to peak values.....	93
Figure 84 TeAC logic improvement results.....	93
Figure 85 Counter driven gear model a) and the torque summation b) .....	94
Figure 86 Simple standalone model of the situation a) and its results b).....	95
Figure 87 Counter driven gear model a) and the torque summation with non-oscillating Nm b) .....	96
Figure 88 Typical HV damper characteristic .....	96
Figure 89 Driveshaft torque FFT after HV damper model calibration of case 6 .....	97
Figure 90 Results after HV damper model calibration .....	98
Figure 91 Counter driven gear model a) and the torque summation after model calibration b) .....	98
Figure 92 Driveshaft torque FFT after driveshaft model calibration of case 6.....	99
Figure 93 Results after driveshaft model calibration .....	99
Figure 94 Optimal values of multiplier of HV damper a) and driveshaft b) damping rates .....	100
Figure 95 Proposed configuration of co-simulation.....	103

## List of tables

Table 1 Toyota CH-R Hybrid 1.8L engine characteristics [6].....	18
Table 2 MG1 and MG2 characteristics [6] .....	19
Table 3 Conditions of measurement of road load .....	51
Table 4 Vehicle equation of motion coefficients .....	52
Table 5 Driving scenarios proposals for the top-level validation .....	54
Table 6 Conditions of the measurement of the top-level validation scenarios .....	55
Table 7 Optimum values of vehicle equation of motion coefficients .....	58
Table 8 Final vehicle equation of motion coefficients.....	59
Table 9 Driving scenarios proposals for the low frequency validation.....	67
Table 10 Conditions of the measurement of the low frequency validation scenarios.....	67
Table 11 Driveshaft stiffness .....	68
Table 12 Weight distribution of low frequency scenario measurement.....	70
Table 13 Driving scenarios proposals for high frequency validation .....	84
Table 14 Conditions of the measurement of the high frequency validation scenarios .....	84
Table 15 Relative error of the 1 <sup>st</sup> order combustion frequency amplitude of driveshaft torque for initial and improved models .....	100

## Attachments

- 1 Top level validation results
- 2 High frequency validation results